Jagiellonian University
Faculty of Physics, Astronomy and Applied
Computer Science

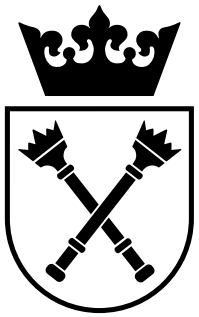

Volume reduction in large-N lattice gauge theories

Mateusz Koreń

Ph.D. thesis under supervision of prof. Jacek Wosiek

Kraków, 2013

Contents

Introduction

Abstract

This work covers volume reduction in quantum field theories on a lattice at large N (number of colors), as first described by Eguchi and Kawai in Ref. [1]. The volume reduction (or volume independence) means that the theory defined on an arbitrarily small lattice is equivalent in the large-N limit to the theory on an infinite lattice with the same bare parameters.

We analyze the volume reduction by means of Monte Carlo simulations using the lattice model on a single site (or a small fixed number of sites) with Wilson fermions in the adjoint representation, using N up to 60. Most of the results focus on two flavours of Dirac fermions and the single fermionic flavour is also discussed where there is a significant difference of behaviour.

We find that the $(\mathbb{Z}_N)^4$ center symmetry, necessary for the realization of volume reduction, is unbroken in the reduced model for a large range of parameters and, in particular, that the maximum admissible value of the adjoint fermion mass is non-zero in the large-N limit.

We calculate physical quantities, such as the plaquette, the static quark potential and the eigenvalues of the Dirac operator. We analyze the finite-N corrections and consider the practicality of volume-reduced models in supplementing the large-volume calculations.

Thesis organization

This work is organized as follows. In Chapter 1 we introduce the basic notations and show the derivation of Eguchi-Kawai reduction as well as the reason of its failure, together with some historical attempts to cure the problems of the original construction. In Chapter 2 we give a pedagogical review of the modern way of understanding volume reduction in the language of large-N orbifold equivalences. Chapter 3 contains a definition of the lattice model we analyze, and a review of perturbative predictions for the volume-reduced models.

Chapters 4, 5 and 6 contain the main part of this work which is the numerical investigation of the large-N volume-reduced lattice model with adjoint fermions. Chapter 4 describes the numerical setup for the Monte Carlo simulations used to generate our results, presented in the subsequent chapters. Chapter 5 describes the phase diagram of the analyzed model and focuses on finding the range of parameters where volume reduction holds. In Chapter 6 we analyze several physical quantities in the volume-reduced model.

Finally, we conclude with Chapter 7 where we summarize the obtained results and give an outline of future directions to extend the analysis performed in this work.

Publications

A substantial part of the results presented in this thesis has already been published by the author and collaborators in Refs. [2, 3].

Acknowledgments

I would like to thank to my supervisor prof. Jacek Wosiek for sharing his experience and providing guidance and support. I am also greatly indebted to prof. Stephen Sharpe who was a mentor for me during my internship at the University of Washington in Seattle where large part of this work was created. I have also greatly benefited from discussions with Barak Bringoltz, as well as with Masanori Hanada, Piotr Korcyl and Mithat Ünsal.

This work was supported by Foundation for Polish Science MPD Programme co-financed by the European Regional Development Fund, agreement no. MPD/2009/6.

I am grateful to the University of Washington for hospitality. Large part of the numerical simulations was done using `Shiva` computing cluster and `Deszno` supercomputer at the Faculty of Physics, Astronomy and Applied Computer Science of Jagiellonian University.

Last but not least, I would like to thank to my parents and to my wife Donata for their continuous love and support during my Ph.D. studies and the writing of this thesis.

Chapter 1

Eguchi-Kawai reduction

1.1 Large-N lattice gauge theory primer

Lattice gauge theory [4] is based on the euclidean path integral formulation of quantum field theories [5, 6]. The spacetime is discretized as a 4-dimensional cubic lattice with spacing a. The lattice coordinates are labeled by

$$x = an = a(n_1, n_2, n_3, n_4), \quad n_i \in \mathbb{Z}. \tag{1.1}$$

To introduce gauge fields we assign a group element $U_\mu(x) \in \mathcal{G}$ (in this work $\mathcal{G}$ will typically be $SU(N)$, unless otherwise stated) to lattice links connecting neighboring sites $(x, x+\mu)$ – matrix notation is imposed in gauge ("color") indices[1]. Fermion fields are introduced by assigning a Dirac spinor $\psi_\alpha(x)$ to each lattice site. The anticommuting nature of fermion fields is taken into account by using Grassmann variables.

Gauge transformation of the fermion field under group $\mathcal{G}$ is given by

$$\psi_\alpha(x) \to \omega(x)\psi_\alpha(x), \tag{1.2}$$

where $\omega(x) \in \mathcal{R}(\mathcal{G})$ is a matrix in some given representation of the group $\mathcal{G}$. The gauge fields transform according to

$$U_\mu(x) \to \omega(x)U_\mu(x)\omega^{-1}(x+\mu). \tag{1.3}$$

[1] In this work we always understand the notation $x + \mu$ as lattice vector x plus unit lattice vector in direction μ.

In continuum, parallel transporter along a curve Γ is given by

$$U_\Gamma = \mathcal{P} \exp\{ig \int_\Gamma \hat{A}_\mu(x) dx_\mu\}, \tag{1.4}$$

where $\mathcal{P}$ is the Dyson's path ordering, g is the bare coupling constant and $\hat{A}_\mu(x) = A_\mu(x)^a \tau^a$ is the vector potential of the gauge field (τ^a are the generators of the proper gauge algebra).

The same quantity on the lattice is given by a product of link matrices along the contour Γ. Thus we identify the lattice variables with their continuum counterparts via

$$U_\mu(x) = \exp\big\{iga\hat{A}_\mu(x + \tfrac{1}{2}\mu)\big\}, \tag{1.5}$$

Moreover, it is easy to see that, in accordance with Eq. 1.3, any parallel transporter along closed contour Γ transforms covariantly and its trace, called the Wilson loop[2]

$$W_\Gamma \equiv \operatorname{Tr} U_\Gamma \tag{1.6}$$

is gauge invariant.

Let us also mention about a special type of Wilson loop that will be of great importance in this work. Consider a finite lattice of sizes $\{L_\mu\}$, with periodic boundary conditions. We can construct a closed contour by taking a straight line of length L_μ in the proper direction – a Wilson loop along such line is called the Polyakov loop (or Wilson line) P_μ and is the simplest example of a non-contractible loop (i.e. loop whose winding number is different from zero).

We can now introduce the action for the theory. It must be gauge invariant and it must give the continuum action ($\sim \operatorname{Tr} \hat{F}^2$) in the limit $a \to 0$. The simplest choice for the gauge action, introduced by Wilson [4], is based on the simplest non-trivial Wilson loop, the so-called plaquette:

$$\operatorname{Tr} U^{\square}_{\mu\nu}(x) = \operatorname{Tr} U_\mu(x) U_\nu(x+\mu) U^{-1}_\mu(x+\nu) U^{-1}_\nu(x), \tag{1.7}$$

[2]It is quite common in the literature to use the term Wilson loop also for the untraced operator along a closed contour. We also use this convention in this work, using the term "Wilson loop matrix" for the untraced operator whenever the meaning cannot be easily deduced from the context.

which can be shown (see e.g. Ref. [7]) to correspond to $\mathrm{Tr}\exp\{iga^2\hat{F}_{\mu\nu}(x)\}$. Therefore we define the action for the gauge group $SU(N)$ as

$$S_{\text{gauge}} = \beta \sum_{x,\,\mu<\nu} \big\{1 - \frac{1}{N}\mathrm{ReTr}U^{\square}_{\mu\nu}(x)\big\}, \tag{1.8}$$

the sum goes over all plaquettes on the lattice and β is the normalization factor which for conformity with the continuum theory must be set to

$$\beta = \frac{2N}{g^2}\,. \tag{1.9}$$

The action for the fermion field

$$S_{\text{ferm}} = \bar{\psi}\, D_{\text{lat}}\, \psi \tag{1.10}$$

requires more attention as the naive discretization of the Dirac operator leads to the famous doubling problem [7]. In this work we choose the simplest solution to this problem, namely the Wilson fermions which remove the unwanted doublers at the cost of explicit breaking of the chiral symmetry which is only restored as $a \to 0$ [7, 8]. The Wilson Dirac operator (with the Wilson parameter $r = 1$ and after customary rescaling) is equal to

$$D^W_{\text{lat}}(x,y) = \delta_{xy} - \kappa \sum_{\mu=1}^{4} \Big[(1-\gamma_\mu)U^{\mathcal{R}}_\mu(x)\delta_{y,x+\mu} + (1+\gamma_\mu)U^{-1\,\mathcal{R}}_\mu(y)\delta_{y,x-\mu}\Big], \tag{1.11}$$

where $U^{\mathcal{R}}$ is the gauge link in the chosen group representation[3], γ_μ are the euclidean Dirac matrices and κ is the (dimensionless) hopping parameter related to the bare fermion mass by

$$\kappa = \frac{1}{2am_0 + 8}. \tag{1.12}$$

Action defined in this way may now be quantized within the path integral formalism, using the generating functional

$$\mathcal{Z} = \int [dU][d\psi][d\bar{\psi}\,] e^{-S_{\text{gauge}}[U] - S_{\text{ferm}}[\psi,\bar{\psi},U]}. \tag{1.13}$$

[3]In this work we will be particularly interested in the adjoint representation. The gauge theory with adjoint fermions will be labeled as QCD(Adj) to distinguish it from the physical QCD with fundamental fermions. Another theory used in this work is QCD(AS), which contains fermions in the two-index antisymmetric representation.

To avoid Grassmann variables we use the bilinearity of the fermionic action and integrate out ψ, $\bar{\psi}$ to get

$$\mathcal{Z} = \int [dU] e^{-S_{\text{gauge}}[U] - \ln \det D^W_{\text{lat}}[U]}. \tag{1.14}$$

Note that, thanks to the lattice regulator, there is no need to introduce gauge fixing via Fadeev-Popov procedure. That is particularly clear in the case of finite lattices (which are used in computer simulations) where the path integral is nothing but a finite-dimensional Haar integral over the group space.

The theory given in Eq. 1.14 contains no dimensionful parameters. However, the renormalization group connects the dimensionless bare coupling constant g with the dimensionful lattice spacing a (which plays the role of the UV cutoff), in a process called dimensional transmutation – see Ref. [7] for a comprehensive discussion. For our purposes, it is sufficient to note that for asymptotically free theories, which are the topic of this work, the continuum limit $a \to 0$ is approached by taking $g \to 0$ (or equivalently $\beta \to \infty$).

We now analyze the large-N limit of the theory i.e. use gauge group $SU(N)$ with infinite (or, in computer practice, finite but large) number of colors. That requires [9] keeping the product

$$b = \frac{1}{g^2 N} \tag{1.15}$$

fixed[4]. As first shown in Ref. [9], the large-N limit results in a vast simplification of the perturbative expansion of the theory – it allows only graphs with topology of a sphere (the so-called planar graphs).

There are several possibilities of what can happen with the fermion fields. If we start from the QCD with $N = 3$ colors and N_f fundamental fermions there are at least 3 interesting possibilities:

1. 't Hooft limit [9] – keep N_f fixed,

[4] b is the inverse of the 't Hooft coupling, $b^{-1} = \lambda = g^2 N$, and is the quantity typically used in the large-N lattice literature. Note that $b = \frac{\beta}{2N^2}$.

2. Veneziano limit [10] – keep the ratio N_f/N fixed,

3. Corrigan-Ramond limit [11] – keep N_f fixed but use fermions in the antisymmetric representation (which coincides with the fundamental representation when $N = 3$).

The first possibility quenches fermions in the large-N limit making the dynamics dependent only on the gluon sector. The two others allow dynamical fermions making the large-N dynamics more reminiscent of the original QCD.

Another major simplification of the theory in the large-N limit is the factorization of products

$$\langle \hat{A}\hat{B} \rangle = \langle \hat{A} \rangle \langle \hat{B} \rangle + \mathcal{O}(1/N), \tag{1.16}$$

where $\hat{A}$ and $\hat{B}$ are quantum operators properly normalized to possess a finite limit as $N \to \infty$ [12, 13]. Therefore, in the large-N theories variances of operators vanish.

The large-N lattice gauge theory is a very active field of work – see Ref. [14] for a recent review of research in this field.

1.2 Derivation of the Eguchi-Kawai reduction

The first notion of volume reduction in large-N lattice gauge theory was introduced by Eguchi and Kawai [1]. Let us consider two theories:

1. $U(N)$ (or equivalently $SU(N)$) pure gauge theory on infinite lattice (called the "full model" in the following), with generating functional

$$\mathcal{Z} = \int [dU]\, e^{-S[U]} = \int (\prod_{x,\mu} dU_{x,x+\mu}) e^{-\beta \sum_{x,\mu<\nu} \left(1 - \frac{1}{N} \mathrm{ReTr} U^{\square}_{\mu\nu}(x)\right)}, \tag{1.17}$$

2. The same theory reduced to a single lattice site with periodic boundary conditions – the so-called Eguchi-Kawai model – with generating

functional

$$\mathcal{Z}_{EK} = \int (\prod_{\mu} dU_\mu) e^{-\beta \sum_{\mu<\nu} \left(1 - \frac{1}{N} \mathrm{ReTr} U^{\square}_{\mu\nu}\right)}, \tag{1.18}$$

where the reduced plaquette is $U^{\square}_{\mu\nu} = U_\mu U_\nu U^\dagger_\mu U^\dagger_\nu$.

Eguchi and Kawai showed that in the large-N limit these two theories satisfy the same Dyson-Schwinger equations and are thus equivalent in the large-N limit (for observables that are invariant under translational symmetry), provided that some conditions are satisfied.

To see what these conditions are let us quickly sketch the proof here. We start with the derivation of the Dyson-Schwinger equations for the expectation values of Wilson loops (also called loop equations) in the full model [1, 12, 15, 16, 17].

First we choose a closed contour Γ such that the link $U_\mu(y)$ is only encountered once in the contour. For ease of notation we label Γ' as the contour Γ without the link $(y, y+\mu)$ i.e.

$$W_\Gamma \equiv \mathrm{Tr}\, U_\Gamma = \mathrm{Tr}\, U_{\Gamma'} U_\mu(y). \tag{1.19}$$

The quantity $\langle \mathrm{Tr}\, U_{\Gamma'} \tau^a U_\mu(y) \rangle$, due to the invariance of the measure in the path integral, must be invariant under the transformation

$$U_\mu(y) \to (1 + i\varepsilon\tau^a) U_\mu(y). \tag{1.20}$$

Collecting the terms linear in ε one obtains

$$\begin{aligned}
\langle \mathrm{Tr}\, U_{\Gamma'} \tau^a \tau^a U_\mu(y) \rangle = \frac{\beta}{2N} \big\langle & \mathrm{Tr}\,(U_{\Gamma'} \tau^a U_\mu(y)) \times \\
& \sum_{\rho \neq \mu} \big(\mathrm{Tr}\, U_\rho(y) U_\mu(y+\rho) U_\rho(y+\mu) U^\dagger_\mu(y) \tau^a - \\
& \quad \mathrm{Tr}\, \tau^a U_\mu(y) U_\rho(y+\mu) U^\dagger_\mu(y+\rho) U^\dagger_\rho(y) + \\
& \quad \mathrm{Tr}\, U^\dagger_\rho(y-\rho) U_\mu(y-\rho) U_\rho(y+\mu-\rho) U^\dagger_\mu(y) \tau^a - \\
& \quad \mathrm{Tr}\, \tau^a U_\mu(y) U^\dagger_\rho(y+\mu-\rho) U^\dagger_\mu(y-\rho) U_\nu(y-\rho) \big) \big\rangle,
\end{aligned} \tag{1.21}$$

where the traces in the sum consist of all the oriented plaquettes in the action that contain $U_\mu(y)$ or its hermitian conjugate. One can now use the

property of the generators τ^a:

$$\sum_{a=1}^{N^2} \tau^a_{ij}\tau^a_{kl} = \tfrac{1}{2}\delta_{il}\delta_{jk} \tag{1.22}$$

and perform the sum over a to get the loop equation:

$$\langle W_\Gamma \rangle = \frac{1}{g^2 N} \sum_{\rho\neq\mu} \Big(\langle W_{\Gamma'_{+\rho}(y,\mu)} \rangle - \langle W_{\Gamma''_{+\rho}(y,\mu)} \rangle + \langle W_{\Gamma'_{-\rho}(y,\mu)} \rangle - \langle W_{\Gamma''_{-\rho}(y,\mu)} \rangle \Big) , \tag{1.23}$$

where the contours are:

$\Gamma = (x, \ldots, y, y+\mu, \ldots, x)$ $\sim$

$\Gamma'_{+\rho}(y,\mu) = (x, \ldots, y, y+\rho, y+\rho+\mu, y+\mu, \ldots, x)$ $\sim$

$\Gamma''_{+\rho}(y,\mu) = (x, \ldots, y, y+\mu, y+\rho+\mu, y+\rho, y, y+\mu, \ldots, x)$ $\sim$

$\Gamma'_{-\rho}(y,\mu) = (x, \ldots, y, y-\rho, y-\rho+\mu, y+\mu, \ldots, x)$ $\sim$

$\Gamma''_{-\rho}(y,\mu) = (x, \ldots, y, y+\mu, y-\rho+\mu, y-\rho, y, y+\mu, \ldots, x)$ $\sim$

When the link $U_\mu(y)$ is encountered more than once in the contour we get additional terms in Eq. 1.23. For example, when

$$\Gamma = (x, \ldots, y, y+\mu, \ldots, z, \ldots, y, y+\mu, \ldots, x)$$

(the contour passes through $U_\mu(y)$ twice in the same direction), on the r.h.s. of Eq. 1.23 we get an additional term proportional to $\langle W_{\Gamma_1} W_{\Gamma_2} \rangle$, where $\Gamma_1 = (y, y+\mu, \ldots, z, \ldots, y)$ and $\Gamma_2 = (y, y+\mu, \ldots, x, \ldots, y)$ sum up to the contour Γ. One can systematically add terms from different link repetitions of $U_\mu(y)$ in a similar manner [16].

Let us now consider the same equations in the reduced (EK) model. For every contour $\Gamma = (x, x+\alpha, x+\alpha+\beta, \ldots, x+\alpha+\beta+\ldots+\omega)$ in the full model one can uniquely assign its counterpart $\tilde{\Gamma} = (\alpha, \beta, \ldots, \omega)$ in the reduced model.

The only difference in the obtained Dyson-Schwinger equations is the presence of additional terms coming from the fact that the reduced counterpart of contour $\Gamma = (x, \ldots, y, y+\mu, \ldots, z, z+\mu, \ldots, x)$ has the same link U_μ repeated even when $y \neq z$. Therefore in this case we get an additional term proportional to $\langle W_{\tilde{\Gamma}_1} W_{\tilde{\Gamma}_2} \rangle$, where $\tilde{\Gamma}_{1,2}$ correspond to the following (open) contours in the full model: $\Gamma_1 = (y, y+\mu, \ldots, z)$, $\Gamma_2 = (z, z+\mu, \ldots, y)$.

Thus, the volume-reduced theory is in general different from the unreduced one. However, in the limit $N \to \infty$ we can factorize the additional terms:

$$\langle W_{\tilde{\Gamma}_1} W_{\tilde{\Gamma}_2} \rangle = \langle W_{\tilde{\Gamma}_1} \rangle \langle W_{\tilde{\Gamma}_2} \rangle + \mathcal{O}(1/N). \tag{1.24}$$

Since $\tilde{\Gamma}_1$ and $\tilde{\Gamma}_2$ correspond to open paths, in both of them at least one term U_μ will not have a corresponding $U_\mu^\dagger$. We now use the fact that the reduced action possesses a symmetry (independently for each lattice direction):

$$U_\mu \to e^{i\phi} U_\mu, \quad \text{where} \quad \phi \in \left\{ 0, \tfrac{2\pi}{N}, \ldots, \tfrac{2(N-1)\pi}{N} \right\}, \tag{1.25}$$

called the center symmetry – it is $\mathbb{Z}_N$ for finite N and becomes $U(1)$ in the large-N limit[5]. Using it we obtain

$$\langle W_{\tilde{\Gamma}_1} \rangle = \langle W_{\tilde{\Gamma}_2} \rangle = 0 \tag{1.26}$$

and all the unwanted terms disappear. We thus see that Eguchi-Kawai reduction holds iff the center symmetry is not spontaneously broken.

* * *

However, the center symmetry in the Eguchi-Kawai model is in fact spontaneously broken at high β for $d > 2$, as can be seen both in the Monte Carlo simulations [18, 19, 20] and in perturbation theory [18, 21] (see Sec. 3.2). This invalidates the Eguchi-Kawai reduction.

Over the years there were several proposals to cure the center-symmetry breaking and obtain a working large-N volume reduction. Let us quickly describe the most interesting approaches:

[5]The full symmetry in d spacetime dimensions is $(\mathbb{Z}_N)^d$ and throughout this work we also use the shortened notation $\mathbb{Z}_N^d$.

1. Force the eigenvalues to satisfy the center symmetry by explicitly fixing them as different elements of the $\mathbb{Z}_N$ group (the so-called Quenched Eguchi-Kawai or QEK model) [18, 22]. This approach is the historically first attempt to heal the Eguchi-Kawai reduction and it gained some popularity. However, several years ago it was shown to fail [23] due to non-trivial correlations between different lattice directions.

2. Use twisted boundary conditions (Twisted Eguchi-Kawai, or TEK model) [24, 25]. The original choice of the twist was shown not to work [26, 27, 28] however a different choice that appears to overcome the problems was proposed recently [29, 30].

3. The center symmetry is intact for physical lattice size larger than some aL_{crit} [20] – as long as one keeps the lattice size $L > L_{\text{crit}}$ the volume reduction allows one to perform the calculations as though it was infinite. This idea is known as partial reduction or continuum reduction and was studied both in four [20] and three dimensions [31] (it was also the topic of the master's thesis of the author of this work, see Ref. [32] for a review of the results). Note that $L_{\text{crit}} \to \infty$ in the continuum limit.

4. Use adjoint fermions to stabilize the center symmetry (Adjoint Eguchi-Kawai, or AEK model) [33]. This idea is inspired by the large-N orbifold equivalences described in Chapter 2 and is the basis of this work[6].

[6]There is also a related idea of trace-deformed (or center-stabilized) reduction [34, 35], that however becomes rather complex when reducing more than one lattice direction.

Chapter 2

Volume reduction as large-N equivalence

2.1 Large-N equivalences

The large-N factorization, Eq. 1.16, not only greatly simplifies the dynamics of the theory but also resembles the classical limit of quantum mechanics where quantum fluctuations are suppressed as $\hbar \to 0$. In fact this analogy can be made formal, as was shown in Ref. [13]. The idea of this construction is to find a basis of coherent states – in this basis the expectation values of quantum operators become classical observables when $N \to \infty$, in the full analogy to the $\hbar \to 0$ limit. Let us briefly discuss the main ingredients of this construction (our treatment follows closely that of Ref. [36]).

We introduce a Lie group $\mathbf{G}$ (called the coherence group) acting on the Hilbert space of the theory $\mathcal{H}$ via a set of unitary operators $\{\hat{\mathbf{G}}(u)\}$, $u \in \mathbf{G}$. We choose a base state[1] $|0\rangle \in \mathcal{H}$ and generate the coherent states by

$$|u\rangle = \hat{\mathbf{G}}(u)|0\rangle. \tag{2.1}$$

E.g. in the case of quantum mechanics of a point particle $\mathbf{G}$ is the Heisenberg group, consisting of space and momentum translations, while

[1] The precise form of the base state is not important for our purposes, see Refs. [13, 36] for a more comprehensive discussion.

for $U(N)$ hamiltonian lattice gauge theory $\mathbf{G}$ is generated by a Lie algebra consisting of all hermitian linear combinations of spatial Wilson loops with up to one conjugate momentum or matter field insertion [13, 36].

The set of coherent states forms an overcomplete basis of the Hilbert space. As $N \to \infty$ the overlaps between different states $\langle u|u'\rangle$ tend exponentially to 0 and the basis becomes orthogonal.

Operators with finite $N \to \infty$ limit of $\frac{\langle u|\hat{A}|u'\rangle}{\langle u|u'\rangle}$ are called classical operators. We introduce the classical phase space defined as the coadjoint orbit of the coherence group[2]. For every classical operator we define the classical observable as

$$a(\zeta) \equiv \lim_{N\to\infty} \langle u|\hat{A}|u\rangle, \tag{2.2}$$

where ζ denotes a point in the classical phase, uniquely determined by u [13]. The following relations hold for the matrix elements of classical operators:

$$\lim_{N\to\infty} \langle u|\hat{A}\hat{B}|u\rangle = a(\zeta)b(\zeta), \tag{2.3}$$

$$\lim_{N\to\infty} \langle u|\big[\hat{A},\hat{B}\big]|u\rangle = \{a(\zeta), b(\zeta)\}_{\mathrm{PB}}, \tag{2.4}$$

where $\{\cdot,\cdot\}_{\mathrm{PB}}$ is the Poisson bracket (the construction of the classical phase space always allows the introduction of the Poisson bracket [13]). The classical dynamics is governed by the classical Hamiltonian, given by the expectation value of the quantum one:

$$h_{cl}(\zeta) \equiv \lim_{N\to\infty} \tfrac{1}{N^2}\langle u|\hat{H}|u\rangle, \tag{2.5}$$

$$\frac{da(\zeta)}{dt} = \{h_{cl}(\zeta), a(\zeta)\}_{\mathrm{PB}}. \tag{2.6}$$

By minimizing the classical Hamiltonian one obtains the ground state of the large-N theory. It is then possible to systematically add $1/N$ corrections to find the excited states [13].

[2]See Section 3 of Ref. [13] for a thorough discussion. For example, in the case of the point particle the coadjoint orbit of the Heisenberg group is simply the two-dimensional plane parametrized by the position and momentum of the particle.

Unfortunately, finding the minimum $\zeta_{\min}$ of h_{cl} has not been attained in the case of gauge theories except for some simple toy models. One can however use the coherent state method to compare different quantum theories – if the classical phase spaces and Hamiltonians of the two theories are identical then the theories are equivalent in the large-N limit. This method has the advantage over the Dyson-Schwinger approach used in Refs. [1, 17] in being completely general – while the Dyson-Schwinger equations can have multiple solutions and identical equations are only guaranteed to give coinciding dynamics in the phase continuously connected to strong-coupling large-mass region [17].

In the following parts of this section we present two particularly interesting examples of large-N equivalences: the orbifold and orientifold equivalences. Both these terms originate from string theory but can be described purely in the QFT language and will be analyzed in this work without mentioning their stringy interpretation.

2.1.1 Orbifold equivalence

Large-N orbifold equivalences were conjectured in Ref. [37] as a way of relating non-perturbative aspects of supersymmetric and non-supersymmetric theories related by orbifold projection. Then they were put in a rigorous framework for gauge theories with and without matter fields in Refs. [17, 36]. In this section we limit ourselves to a general discussion of orbifold equivalences, postponing the detailed discussion until Sec. 2.2.

The orbifold projection is based on a discrete symmetry (the so-called projection group $\mathbf{P}$) of a "parent" field theory. We project out all degrees of freedom in the parent that are not invariant under this symmetry, yielding a "daughter" field theory. Both theories possess the same large-N limit for a class of observables commuting with $\mathbf{P}$ (called the "neutral sector"), provided that $\mathbf{P}$ is not spontaneously broken[3].

[3]Technically, the equivalence is independent of the realization of $\mathbf{P}$. However, if $\mathbf{P}$ is spontaneously broken the minimum of the classical Hamiltonian lies outside the neutral sector, thus preventing the extraction of information about quantum theories of interest

The projection groups typically used for orbifold equivalences, such as volume reduction, are cyclic groups or products thereof. To be specific let us choose just one cyclic group $\mathbf{P} = \mathbb{Z}_m$ embedded in a pure-gauge $U(N)$ lattice gauge theory[4], where $N = mN'$ with integer N'.

The embedding is chosen so that the gauge fields $U_\mu(x)$ transform under $\mathbf{P}$ as [36, 38]:

$$U_\mu(x) \to \gamma U_\mu(x)\gamma^\dagger, \tag{2.7}$$

where $\gamma = \Omega^{(m)} \times \mathbb{I}_{N'}$, with $\Omega^{(m)}$ defined as the clock matrix:

$$\Omega^{(m)} \equiv \mathrm{diag}[1, \omega, \ldots, \omega^{m-1}], \quad \text{with} \quad \omega = e^{2\pi i/m}. \tag{2.8}$$

The orbifold projection removes the degrees of freedom that are not invariant under the transformation given in Eq. 2.7[5]. As a result, the $N \times N$ matrices of the gauge fields are left with non-zero entries only in m blocks, each of size $N' \times N'$ (an example is given in Fig. 2.1). All of these blocks are unitary by construction, thus the daughter theory will have a $[U(N')]^m$ symmetry group that can be interpreted as $U(N')$ gauge theory with additional internal space (called "theory space" $\mathbf{T}$ by the authors of Ref. [36]) consisting of m independent factors on a discretized circle (or a torus in the general case of many cyclic groups).

There is a bijective mapping of the neutral observables between the daughter and parent theories. For example, for the Wilson loops:

$$\frac{1}{N}\mathrm{Tr}\, U_\Gamma = \frac{1}{m}\sum_{i\in\mathbf{T}} \frac{1}{N'}\mathrm{Tr}\, U_\Gamma^{(i)}, \tag{2.9}$$

where the discrete index i is used for averaging over the theory space.

In Ref. [36] the authors have proven that the subgroups of the coherence groups that define the neutral sectors are isomorphic in the two theories,

and making the problem rather academic [36].

[4]The procedure can be extended to include adjoint matter fields in a completely analogous way [36], see also Sec. 2.2.

[5]The more general form of the constraint is of the form $U_\mu(x) = \gamma U_\mu(x)\gamma^\dagger e^{2\pi i r/m}$, where $r \in \mathbb{Z}$ is called the charge of the field. Non-zero charge will be used for the gauge fields in Sec. 2.2, cf. Eq. 2.14.

$$U^{(\text{daughter})} = \begin{pmatrix} U_{11} & U_{12} & 0 & 0 & 0 & 0 \\ U_{21} & U_{22} & 0 & 0 & 0 & 0 \\ 0 & 0 & U_{33} & U_{34} & 0 & 0 \\ 0 & 0 & U_{43} & U_{44} & 0 & 0 \\ 0 & 0 & 0 & 0 & U_{55} & U_{56} \\ 0 & 0 & 0 & 0 & U_{65} & U_{66} \end{pmatrix}$$

Figure 2.1: An example result of orbifold projection, with $\mathbf{P} = \mathbb{Z}_3$ acting on a $U(6)$ gauge theory. The fields invariant under $\mathbf{P}$ are given by the condition $U = \gamma U \gamma^\dagger$, where γ (in a convenient basis) is given by $\gamma = \Omega^{(3)} \times \mathbb{I}_2 = \text{diag}[1, 1, e^{2\pi i/3}, e^{2\pi i/3}, e^{-2\pi i/3}, e^{-2\pi i/3}]$. The remaining symmetry of the daughter theory is $[U(2)]^3$.

thus giving the same classical phase spaces and Hamiltonians – and making the theories equivalent in the large-N limit, as discussed in the earlier part of this section. One particularly interesting example of the orbifold equivalence will be the volume reduction, discussed in Sec. 2.2, where the theory space is identified with the physical spacetime.

2.1.2 Orientifold equivalence

Another example of large-N equivalence that attracted a lot of attention is the orientifold equivalence which relates large-N limits of QCD(Adj) with n_f adjoint Majorana fermions and QCD(AS) with N_f Dirac fermions, at $n_f = N_f$ [39, 40].

This equivalence was initially investigated in the case of $n_f = 1$ where it relates a supersymmetric theory ($\mathcal{N} = 1$ SYM) with a non-supersymmetric one ($N_f = 1$ QCD(AS)). Another particularly interesting possibility, which will be used in the following part of this work, is $n_f = 2$. QCD(AS) at large number of colors is a very natural large-N limit of the physical $N = 3$ QCD [41] (called the Corrigan-Ramond limit, see Sec. 1.1), especially at $N_f = 2$

which describes the 2 lightest physical quarks.

In this section we follow the terminology of Ref. [42]. In this treatment the orientifold equivalence is an example of "daughter-daughter" equivalence in the sense that both theories can be constructed from a common parent by applying different orientifold projections.

The orientifold projections are based on $\mathbb{Z}_2$ projection groups related with charge conjugation ($\mathcal{C}$) symmetry. The parent theory for both theories under investigation is $SO(2N)$ gauge theory with n_f adjoint Majorana fermions. The two theories result from different $\mathbb{Z}_2$ projections of the parent theory [42]. The QCD(Adj) with n_f Majorana fermions is a result of imposing the constraint

$$U = JUJ^T,\ \psi = J\psi J^T, \tag{2.10}$$

where $J = i\sigma_2 \times \mathbb{I}_N \in SO(2N)$, U symbolically denotes the bosonic degrees of freedom and ψ the fermionic degrees of freedom. On the other hand, QCD(AS) with $N_f(= n_f)$ Dirac fermions is obtained from the parent theory by the projection with the constraint

$$U = JUJ^T,\ \psi = -J\psi J^T. \tag{2.11}$$

The projection in Eq. 2.11 involves additional factor $(-1)^F$, which multiplies the fermionic fields by -1.

One can show that the neutral sectors in both theories consist of $\mathcal{C}$-even operators (see Ref. [42] for details). Thus, for the equivalence to be meaningful it is necessary that the charge conjugation symmetry is not spontaneously broken in either of the theories [42, 43]. For the Wilson loops this requirement can be written simply as

$$\langle \mathrm{Tr}\, U_\Gamma \rangle = \langle \mathrm{Tr}\, U_\Gamma^\dagger \rangle. \tag{2.12}$$

While the $\mathcal{C}$ symmetry is expected to be preserved on $\mathbb{R}^4$ [43] it was shown to be broken in QCD(AS) on $\mathbb{R}^3 \times S^1$, with periodic boundary conditions for fermions, for small enough radius of the circle [42].

2.2 Volume reduction as large-N orbifold equivalence

Volume reduction/expansion in the language of orbifold projections was introduced in Refs. [33, 44]. For definiteness and ease of notation we consider the following two d-dimensional lattice gauge theories:

- Theory 1: $U(N')$ gauge theory on a periodic lattice of volume $\Lambda = L^d$, with or without adjoint matter fields,
- Theory 2: $U(N)$ single-site model with the same matter content as theory 1.

The generalization to arbitrary volume of theory 2 and anisotropic lattices is also possible (the only difference is a somewhat more complicated notation, see the Appendix of Ref. [33] for details).

2.2.1 Theory 1 $\rightarrow$ Theory 2 (volume reduction)

The volume reduction from theory 1 to 2 is implemented by discarding all fields carrying non-zero momentum [33]. This can be described in the language of orbifold projections with theories 1 and 2 being the parent and daughter theories respectively, with $N' = N$.

Due to the periodic boundary conditions theory 1 has a $\mathbb{Z}_L^d$ translational invariance. We choose the projection group $\mathbf{P} = \mathbb{Z}_L^d$ and eliminate all the fields that are not invariant under the translations. The invariant fields are manifestly visible in the momentum space – consider a lattice Fourier transform for some generic field Φ:

$$\Phi_{\text{Th.1}}(x) = \sum_{n \in \mathbb{Z}_L^d} \tilde{\Phi}_n e^{2\pi i n \cdot x/L} \xrightarrow{n=0} \Phi_{\text{Th.2}} = \tilde{\Phi}_0. \tag{2.13}$$

As a result of the projection all the components except the (constant in space) zero-momentum mode are discarded.

The projection defines a one-to-one mapping between the Wilson loops in the parent theory, averaged over spacetime, and the Wilson loops in the

daughter theory[6]. For example, the Wilson action of pure gauge theory is cast to the Eguchi-Kawai action times L^d (the factor of volume accounts for the ratio of discarded degrees of freedom of the parent theory). This result also applies to the Wilson loops with arbitrary number of adjoint matter field insertions along the loop (called "single-trace observables" by the authors of Ref. [33]).

2.2.2 Theory 2 → Theory 1 (volume expansion)

We start with pure gauge theory and choose $N = L^d N'$. The single-site model is now the parent theory whereas the "big" lattice of theory 1 is the daughter. We choose $\mathbf{P} = \mathbb{Z}_L^d$ which is a subgroup of the $\mathbb{Z}_N^4$ center symmetry of theory 2.

As usual, the orbifold projection eliminates all degrees of freedom not invariant under $\mathbf{P}$ – the proper embedding of the projection group in the full symmetry of the theory will allow us to identify the subblocks of gauge matrices in the parent with different points in the spacetime of the daughter theory.

The projection is equivalent to imposing a following set of constraints on the gauge fields [33]:

$$U_\mu = \begin{cases} \gamma_\nu U_\mu \gamma_\nu^\dagger \, e^{2\pi i/L}, & \mu = \nu \\ \gamma_\nu U_\mu \gamma_\nu^\dagger \,, & \mu \neq \nu \end{cases} \tag{2.14}$$

Here γ_ν are defined as

$$\gamma_\nu = \underbrace{\mathbb{I}_L \times \ldots}_{\nu-1} \times \Omega^{(L)} \times \underbrace{\mathbb{I}_L \times \ldots}_{d-\nu} \times \mathbb{I}_{N'}, \tag{2.15}$$

with $\Omega^{(L)}$ being the clock matrix, cf. Eq. 2.8.

As a result of the projection, in every U_μ there are only L^d non-zero blocks of size $N' \times N'$ left. Each of the $N' \times N'$ blocks is a unitary matrix by itself, and can be naturally associated with a single link in the "big"

[6]With winding numbers being integer multiples of L (this includes all the "ordinary" contractible Wilson loops with zero winding number).

lattice by inspection of how it couples to other blocks in the projected Eguchi-Kawai action[7].

Under the same mapping the Wilson loops of the parent theory are associated one-to-one with Wilson loops in the daughter theory averaged over spacetime volume. Likewise the action becomes the standard big lattice action up to a constant factor that ensures the equality of 't Hooft couplings in the two theories.

Addition of adjoint matter fields (both scalars and fermions) is straightforward as these fields transform in the same way as the gauge fields, they also preserve center symmetry. Thus the effect of the projection is simply

$$\Phi = \gamma_\nu \Phi \gamma_\nu \tag{2.16}$$

where Φ is the matter field matrix. There is a one-to-one mapping between the single-trace observables, just as in the pure-gauge case.

2.2.3 Large-N equivalence

As discussed earlier, the large-N dynamics of parent and daughter theories related by orbifold projections coincide in the neutral sectors. However, for the ground states (and thus the physical properties) of the theories to coincide, the symmetries defining the projections must not be spontaneously broken. Of these symmetries, the one that is the most non-trivial to satisfy is the center symmetry of the small-volume model – it is broken in the pure-gauge case, thus invalidating Eguchi-Kawai reduction. In the subsequent chapter we will analyze the introduction of adjoint fermions in order to keep the center symmetry intact.

2.2.4 Effective system size at finite N

The orbifold equivalence is demonstrated by taking $N \to \infty$. However, since in computer simulations we are always dealing with finite N it is useful to

[7]The phase factor $e^{2\pi i/L}$ in Eq. 2.14 is chosen so that the correct coupling of blocks to the nearest neighbors is obtained – see the Appendix of Ref. [33] for a comprehensive discussion.

consider, at least qualitatively, the effective size L_{eff} of the volume-reduced lattice (or, equivalently, the effective volume $V_{\text{eff}} = L_{\text{eff}}^4$) and its finite-$N$ dependence.

If the large-N equivalence holds, we expect that the theory on a single site with N colors gives the same physical results as the theory on a volume V_{eff} with N_{eff} colors – up to corrections suppressed by powers of $1/N_{\text{eff}}$. There is a trade-off between increasing L_{eff} and N_{eff} and the value of N_{eff} must be large enough so that the finite-N_{eff} corrections to the quantities of interest are not too large. We choose N_{eff} fixed and ask what is the dependence $L_{\text{eff}}(N)$.

The orbifold projection of presented in Sec. 2.2.2 gives an explicit prescription of packaging the matrices in different spacetime points into a larger gauge matrix. The $N \times N$ link matrices are partitioned into blocks of size $N_{\text{eff}} \times N_{\text{eff}}$, with $N_{\text{eff}} = N/L_{\text{eff}}^4$. If we fix N_{eff} to some constant value (e.g. 3) we obtain the effective-size scaling

$$L_{\text{eff}}(N) \propto N^{1/4}. \tag{2.17}$$

Chapter 3

Volume reduction with adjoint fermions

3.1 Definition of the Adjoint Eguchi-Kawai model

Addition of adjoint fermions was proposed by the authors of Ref. [33] as a way to stabilize center symmetry. They have shown that the massless adjoint fermions with periodic boundary conditions give a repulsive contribution to the one-loop potential of Polyakov loop eigenvalues that allows the center symmetry to be preserved. There are also reasons to believe that the center symmetry may be preserved even with heavy adjoint fermions (see Sec. 3.2).

In this section we define the model that will be the main topic of this work, the Adjoint Eguchi-Kawai (AEK) model, i.e. a single-site lattice theory with $SU(N)$ gauge group and N_f adjoint Dirac fermions. The generating functional of the theory is

$$Z_{\mathrm{AEK}} = \int \prod_{\mu} [dU] \, \exp\left(-S_{\mathrm{gauge}}[U] + \ln(\det D_W[U])^{N_f}\right), \tag{3.1}$$

where the gauge part is the Eguchi-Kawai action (cf. Eq. 1.18):

$$S_{\text{gauge}} = -2Nb \sum_{\mu<\nu} \text{ReTr}\, U_\mu U_\nu U_\mu^\dagger U_\nu^\dagger + \text{constant}. \tag{3.2}$$

The constant is independent of the gauge configuration and we neglect it in the numerical simulations. We use Wilson fermions with periodic boundary conditions in all directions:

$$D_W = 1 - \kappa \left[\sum_{\mu=1}^{4} (1-\gamma_\mu)\, U_\mu^{\text{adj}} + (1+\gamma_\mu)\, U_\mu^{\dagger\text{adj}} \right]. \tag{3.3}$$

The Wilson discretization is chosen due to its simplicity (especially when working with fermions that are not very light), following Refs. [2, 45] (see also Ref. [46] for a related calculation on a 2^4 lattice). Overlap discretization was also used in the literature [47, 48].

The bare quark mass is zero at $\kappa = 1/8$. However, since Wilson fermions do not preserve chiral symmetry at finite a, the physical quark masses are additively renormalized. We thus define $\kappa_c(b)$ as the value of κ at which the physical quark mass becomes 0. The value of κ_c goes to $1/8$ as $a \to 0$ but it is in general different (larger) than that at finite lattice spacing, and the physical quark mass becomes:

$$m_{\text{phys}} = \frac{1}{a}\left(\frac{1}{2\kappa} - \frac{1}{2\kappa_c}\right). \tag{3.4}$$

The gauge theory with adjoint fermions is asymptotically free if $N_f < N_f^I = 11/4$, independently on the value of N. It is argued by a range of analytic methods [49, 50] that (also independently on N) there exists a value $N_f^* < N_f^I$ above which the massless theory loses its confining character and develops an infrared fixed point (becomes conformal). The range $N_f \in [N_f^*, N_f^I)$ is called the "conformal window". N_f^* is estimated by various methods to be in $N_f^* \in [1\frac{1}{16}, 2\frac{3}{40}]$ [49]. However, only non-perturbative studies can give a definite answer whether the theory with given N_f lies in the conformal window or not[1].

[1]This is especially interesting in the case $N_f = 2$ for which the analytic methods are not unanimous. Several lattice studies have been performed for this theory (see below).

Thus, the AEK models with $N_f = 1/2$, $N_f = 1$ and $N_f = 2$ are all interesting, for different reasons. Let us briefly review the putative large-volume equivalents of the three theories:

1. $N_f = 1/2$ (single Majorana fermion): this corresponds, in the massless case, to the large-N limit of $\mathcal{N} = 1$ SYM. This theory has been extensively studied, also using lattice methods, although this is somewhat difficult due to the so-called sign problem [51, 52, 53]. The lattice regularization also breaks the supersymmetry and a set of specific methods has to be used to analyze this theory efficiently. We do not attempt to analyze the supersymmetric case in this work.

2. $N_f = 1$: as discussed in Sec. 2.1 the large-N orientifold equivalence connects the theory with N_f adjoint Dirac fermions to the theory with $2N_f$ Dirac fermions in the antisymmetric representation. On the other hand, large-N QCD(AS) with two flavours is the Corrigan-Ramond limit of the physical QCD with 2 lightest quarks. Thus there exists a chain of orbifold-orientifold equivalences, pictured in Fig. 3.1, that connects $N_f = 1$ AEK to $N_f = 2$ QCD, up to $1/N$ corrections [33]! The large-volume theory, $N_f = 1$ QCD(Adj), is expected to be confining and to show spontaneous breaking of chiral symmetry [49, 50].

3. $N_f = 2$: the theory with two flavours of massless adjoint fermions is expected to lie in the conformal window or close to it [49, 50]. The best analyzed case is $N = 2$ due to its use in the walking technicolor theory – it is now rather well established that the theory is conformal [54, 55, 56]. This result is expected to persist for all N [49, 50] – e.g. note that the gluonic and fermionic degrees of freedom scale with N in the same way and that the Gell-Mann–Low β function of the theory is independent on N up to two loops (although there exists an N-dependence in the fourth-order correction to the β function [57]). Also note that the theories inside the conformal window are perfectly feasible to analyze using volume reduction [58].

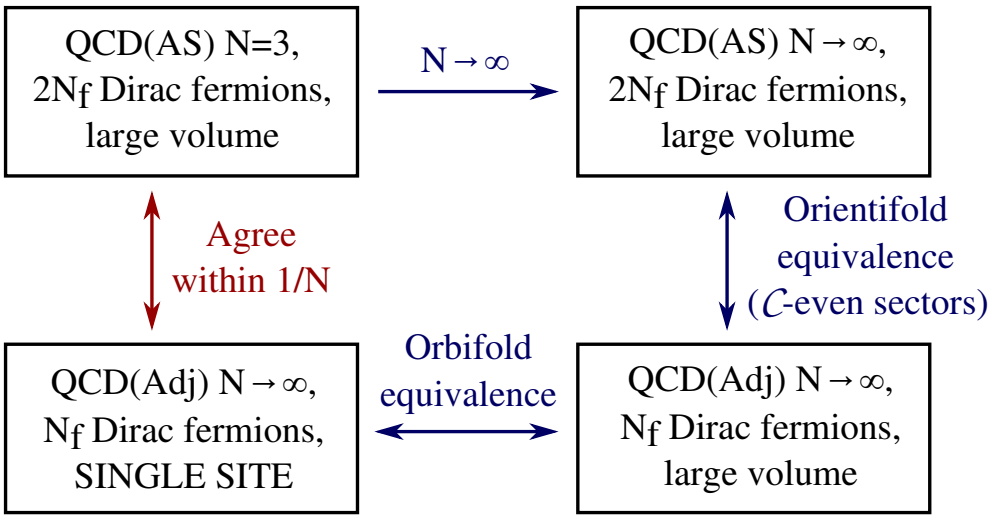

Figure 3.1: The chain of orbifold-orientifold equivalences connecting the QCD with $N = 3$ (in the antisymmetric representation which is equivalent to the fundamental representation at this value of N) with $2N_f$ flavours and the AEK model with N_f flavours.

Also, if the center symmetry is preserved for heavy quarks we expect that in this region the AEK model well approximates the dynamics of the large-volume pure-gauge model, regardless of N_f [45]. That would be a realization of a working Eguchi-Kawai reduction.

3.2 Perturbative calculation

In this section we investigate the perturbative properties of the volume-reduced systems. We first consider the pure gluonic model and show the emergence of the center symmetry breaking that invalidates the volume reduction. Then we analyze the impact of adjoint fermions, both in the massless and in the massive case.

3.2.1 Pure-gauge case

The perturbative calculation of the one-loop potential in the (four-dimensional) Eguchi-Kawai model can be found in Refs. [18, 21][2]. The action of the model can be rewritten, up to a constant factor, as

$$S_{\text{gauge}} = Nb \sum_{\mu<\nu} \text{Tr}\left([U_\mu, U_\nu][U_\mu, U_\nu]^\dagger\right). \tag{3.5}$$

The minimum of the action is obtained when $[U_\mu, U_\nu] = 0$ i.e. when the link matrices can be simultaneously diagonalized. Thus it is convenient to parametrize:

$$U_\mu = V_\mu D_\mu V_\mu^\dagger, \ \mu = 1, \ldots, 4 \tag{3.6}$$

where $D_\mu = \text{diag}\,[e^{i\vartheta_\mu^1}, \ldots, e^{i\vartheta_\mu^N}]$ and V_μ is a unitary matrix.

At large b the effective potential can be found by calculating the partition function in the vicinity of the diagonal link matrices. We change the integration variables to ϑ and V obtaining

$$Z_{\text{EK}} = \mathcal{N} \int \Big(\prod_\mu \prod_i d\vartheta_\mu^i\Big) \prod_\mu \prod_{i<j} \sin^2 \tfrac{\vartheta_\mu^i - \vartheta_\mu^j}{2} Z'(\vartheta), \tag{3.7}$$

$$Z'(\vartheta) = \int \Big(\prod_\mu dV_\mu\Big) \exp\Big(Nb \sum_{\mu\neq\nu} \text{Tr}\left(V_\mu D_\mu V_\mu^\dagger V_\nu D_\nu V_\nu^\dagger V_\mu D_\mu^* V_\mu^\dagger V_\nu D_\nu^* V_\nu^\dagger\right)\Big) \tag{3.8}$$

We may now fix the gauge – we choose the "timelike" gauge $V_1 = I$, eliminating one of the integrals. When b is large the remaining link matrices are close to being diagonal, thus we can write

$$V_\mu = \exp(iA_\mu), \ \mu = 2, \ldots, 4 \tag{3.9}$$

and expand in the hermitian matrices A_μ. Note that after choosing the timelike gauge there still exists a residual gauge freedom – Eq. 3.6 is invariant with respect to the transformation:

$$V_\mu \to V_\mu \Lambda_\mu, \tag{3.10}$$

[2]In this derivation we use the timelike gauge following Ref. [21] however we do not use the smart parametrization trick used in that Ref. This (arguably) makes the derivation simpler in our approach, at the cost of harder generalization to arbitrary dimensionality.

where Λ_μ is an arbitrary unitary diagonal matrix. To remove this freedom, we require (following Ref. [21]) that matrices A_μ have vanishing entries on the diagonal.

The first order of the expansion in A_μ disappears and in the second order we obtain:

$$Z'(\vartheta) = \int \big(\prod_{\mu>1}\prod_{i>j} d^2A_\mu^{ij}\big) \exp\Big(-16Nb\sum_{i>j}\sum_{\mu\neq\nu}\sin^2\tfrac{\vartheta_\mu^i-\vartheta_\mu^j}{2}\sin^2\tfrac{\vartheta_\nu^i-\vartheta_\nu^j}{2} \times \big(|A_\mu^{ij}|^2+|A_\nu^{ij}|^2-A_\mu^{ij}A_\nu^{ji}-A_\mu^{ji}A_\nu^{ij}\big)\Big), \tag{3.11}$$

with $A_1^{ij}\equiv 0$. For each given i,j the integral in Eq. 3.11 is a 3-dimensional complex Gaussian integral. We evaluate the determinants and obtain:

$$Z_{\mathrm{EK}} = \mathcal{N}'\int \big(\prod_{\mu,i} d\vartheta_\mu^i\big)\exp\big(-V_{\text{1-loop}}(\vartheta)\big), \tag{3.12}$$

$$V_{\text{1-loop}}(\vartheta) = 2\sum_{i>j}\log\big(\sum_\mu \sin^2\tfrac{\vartheta_\mu^i-\vartheta_\mu^j}{2}\big), \tag{3.13}$$

where $V_{\text{1-loop}}(\vartheta)$ is called the one-loop effective potential (or effective action). In Refs. [18, 21] the effective potential was calculated for arbitrary lattice dimensionality:

$$V_{\text{1-loop}}(\vartheta) = (d-2)\sum_{i>j}\log\big(\sum_\mu \sin^2\tfrac{\vartheta_\mu^i-\vartheta_\mu^j}{2}\big) \tag{3.14}$$

The validity of the large-N volume reduction in $d=2$ is well-known by other methods [1, 59]. However when $d>2$ the effective potential for the phases ϑ_μ^i is attractive and favours a peaked distribution of eigenvalues, signalling spontaneous breaking of the center symmetry. This phenomenon is in fact seen in the Monte Carlo simulations [18, 19, 20, 31, 32] and it invalidates the Eguchi-Kawai volume reduction.

3.2.2 The effect of adjoint fermions

We now add N_f adjoint Wilson fermions with periodic boundary conditions to the theory. In one-loop perturbation theory the Wilson Dirac operator,

Eq. 3.3, is diagonal in color space [60] and one can easily calculate the one-loop potential (up to a ϑ-independent term) [61]:

$$V_{\text{1-loop}}(\vartheta) = 2\sum_{i>j}\log\Big(\sum_{\mu}\sin^2\tfrac{\vartheta^i_\mu-\vartheta^j_\mu}{2}\Big) - 4N_f\sum_{i>j}\log\Big(\sum_{\mu}\sin^2(\vartheta^i_\mu-\vartheta^j_\mu)+m_W^2(\vartheta)\Big), \tag{3.15}$$

where the first term is the contribution of the gauge fields and the second term is the fermionic part, with m_W being the contribution from the bare mass and the Wilson term:

$$m_W(\vartheta) = am_0 + 2\sum_{\mu}\sin^2\tfrac{\vartheta^i_\mu-\vartheta^j_\mu}{2}. \tag{3.16}$$

The fermionic term in the potential has the opposite sign to the gauge part (the fermions give a repulsive contribution to the potential) and the analysis which term dominates is more involved in this case. In particular, the singularities for coinciding eigenvalues can now lead to incorrect conclusions if not analyzed with proper care [61].

The situation is simpler in the case of only one compactified direction. Ref. [33] contains the one-loop result for massless fermions in the $\mathbb{R}^3 \times S^1$ case (in the continuum):

$$V_{\text{1-loop}}(\Omega) = \big(N_f - \tfrac{1}{2}\big)\frac{1}{\pi^2 L^4}\sum_{r=1}^{\infty}\frac{1}{n^4}|\operatorname{Tr}\Omega^r|^2, \tag{3.17}$$

where Ω is the Polyakov loop matrix in the compactified direction. For $N_f > 1/2$ this potential prefers the vanishing traces of $\operatorname{Tr}\Omega^r$ and thus it is repulsive for the phases of eigenvalues, resulting in the preservation of the center symmetry[3].

The continuum analysis has been extended to the massive case in Refs. [62, 63]. A corresponding lattice analysis with Wilson fermions was presented in Refs. [60, 64]. Both these approaches show that as we increase the mass from zero there is a cascade of transitions breaking $\mathbb{Z}_N$ symmetry

[3]For $N_f = 1/2$ (the supersymmetric case, see Sec. 3.1) the one-loop potential vanishes and different methods were used to show that the center symmetry is preserved in this case, see Ref. [33].

to its $\mathbb{Z}_K$ subgroups with K decreasing from large values at very small mass to 1 at very large mass[4].

This effect can be understood as follows [64]. The one-loop effective potential can be written as

$$V_{\text{1-loop}}(\Omega) = \sum_{r=1}^{\infty} V_r |\operatorname{Tr} \Omega^r|^2 + \text{Const.}, \tag{3.18}$$

where the coefficients V_r are of the form[5]:

$$V_r = N_f V_r^{(\text{ferm.})} - V_r^{(\text{gauge})} \quad \text{where} \quad V_r^{(\text{ferm.})}, V_r^{(\text{gauge})} > 0\,. \tag{3.19}$$

The sign of V_r determines the realization of the center symmetry (at the one-loop level). If all $V_r \geq 0$ for $1 \leq r < N$ (and at least one of them is greater than zero) then the center symmetry is unbroken. It is shown in Ref. [64] that this is the case for massless fermions with $N_f > 1/2$. On the other hand, if for some $K < N$ we have $V_K < 0$ then the symmetry is broken to the $\mathbb{Z}_K$ subgroup. Ref. [64] numerically shows that this is the case for the massive fermions, with $K \sim 1/am$.

This result is easy to understand intuitively [64] – in the reduction language r corresponds to euclidean distance ($\operatorname{Tr} \Omega^r$ wraps r times around the compactified direction) in the corresponding volume-expanded theory. If the fermions have a mass then their range is smaller than that of the massless gluons and at some r the fermionic contribution, that dominates at small distance, must become smaller than the gluonic one.

Thus the one-loop analysis with one compact direction allows reduction only with the fermions of mass of order $\mathcal{O}(1/aN)$, which vanishes in the large-N limit.

However, as pointed in Refs. [58, 61], this picture is far from being complete, especially when compactifying multiple directions. For example,

[4]This silently assumes that N is divisible by K – however, as we will see in Chapter 5, there exist phases with only approximate $\mathbb{Z}_K$ symmetry, e.g. $\mathbb{Z}_N$ at odd N can break into approximate $\mathbb{Z}_2$ with bunches of eigenvalues differing by $\mathcal{O}(1/N)$ – this is a subleading effect at large N and we neglect this subtlety in the analysis of this chapter.

[5]The explicit expressions are not important for our purposes, see Ref. [64] for details.

the breaking of the symmetry in the single-site model causes the eigenvalues to coincide which results in an IR singularity in Eq. 3.15. This is a result of integrating out massless modes that are necessary for the correct description of the long-distance behaviour of the theory [61].

The authors of Ref. [61] give a semi-quantitative description of the neglected modes by introducing a matrix model from which they infer the non-perturbative fluctuation scale at which the one-loop analysis breaks down. They estimate the size of the eigenvalue separation to be of order $\sim b^{-1/4}$.

Therefore, when the perturbation theory suggests that the center symmetry is broken to a $\mathbb{Z}_K$ subgroup with $K \gg 1$, the separation of the bunches of eigenvalues may be in fact smaller than their width and the resulting phase is indistinguishable from the completely unbroken phase, thus leading to a working large-N volume reduction. The final picture can however only be resolved by non-perturbative calculations, such as the one presented in the subsequent chapters.

Chapter 4

Monte Carlo simulation of the AEK model

In this chapter we present the numerical methods to analyze the Adjoint Eguchi-Kawai model by means of Monte Carlo simulations. We analyze both the $N_f = 1$ and $N_f = 2$ cases. We use Hybrid Monte Carlo algorithm [65] to generate the ensembles, equipped with the rational approximation in the case of the single fermionic flavour [66, 67].

4.1 Hybrid Monte Carlo – general idea

Hybrid Monte Carlo (HMC) is a standard algorithm used in lattice gauge theories with dynamical fermions. Let us first review the basic concepts of the algorithm (for a more in-depth discussion see e.g. [68, 69]).

Consider a general bosonic field A with action $S[A]$. For simplicity we employ matrix notation and omit the indices – in lattice gauge theory one has $A \equiv A^a_\mu(x)$.

HMC is based on introduction of auxiliary Gaussian-distributed momenta conjugate to A. We can symbolically write the resulting Hamiltonian as

$$H[A, P] = \tfrac{1}{2}\mathrm{Tr}\, P^2 + S[A]\,. \tag{4.1}$$

Note that one can easily integrate out the momenta and recover the original expectation values:

$$\langle O \rangle_{A,P} = \frac{\int \mathcal{D}[A]\mathcal{D}[P]\, e^{-H[A,P]}\, O[A]}{\int \mathcal{D}[A]\mathcal{D}[P]\, e^{-H[A,P]}} = \frac{\int \mathcal{D}[A]\, e^{-S[A]}\, O[A]}{\int \mathcal{D}[A]\, e^{-S[A]}} = \langle O \rangle_A \,. \quad (4.2)$$

The Hamiltonian gives the classical equations of motion, called Molecular Dynamics (MD) equations, that leave H unchanged and thus lead to exact microcanonical evolution of the system in additional "computer" time τ:

$$\dot{A} = \frac{\partial H}{\partial P} = P \,, \quad \dot{P} = -\frac{\partial H}{\partial A} = -\frac{\partial S}{\partial A} \,. \quad (4.3)$$

In computer practice we integrate the MD equations numerically, introducing a discrete step size $\varepsilon = \Delta\tau$. This method introduces systematic errors. To balance this effect the algorithm utilizes a Metropolis accept/reject step with acceptance probability

$$P_{acc}(A \to A', P \to P') = \min\{1,\, \exp(H[A,P] - H[A',P'])\} \quad (4.4)$$

after integrating the equations from $\tau = 0$ to $\tau = \tau_{fin}$ (which is most often set to 1).

One can show that this corrects the errors and satisfies the detailed balance condition for A provided that the Molecular Dynamics integration is reversible

$$P_{MD}(A \to A', P \to P') = P_{MD}(A' \to A, -P' \to -P) \quad (4.5)$$

and preserves the integration measure $\mathcal{D}[A]\mathcal{D}[P]$. The simplest and most commonly used integrator that satisfies these conditions [68] is the leap-frog integrator:

$$\mathcal{I}(\varepsilon, \tau_{fin} = \varepsilon N_{MD}) = \left(\mathcal{P}_{\frac{\varepsilon}{2}}\, \mathcal{A}_{\,\varepsilon}\, \mathcal{P}_{\frac{\varepsilon}{2}}\right)^{N_{MD}} , \quad (4.6)$$

where

$$\mathcal{P}_\varepsilon : \{A(\tau_A), P(\tau_P)\} \to \left\{A(\tau_A),\; P(\tau_P + \varepsilon) = P(\tau_P) - \varepsilon\, \tfrac{\partial S}{\partial A}\big|_{A(\tau_A)}\right\}, \quad (4.7)$$

$$\mathcal{A}_\varepsilon : \{A(\tau_A), P(\tau_P)\} \to \{A(\tau_A + \varepsilon) = A(\tau_A) + \varepsilon P(\tau_P),\; P(\tau_P)\} \,. \quad (4.8)$$

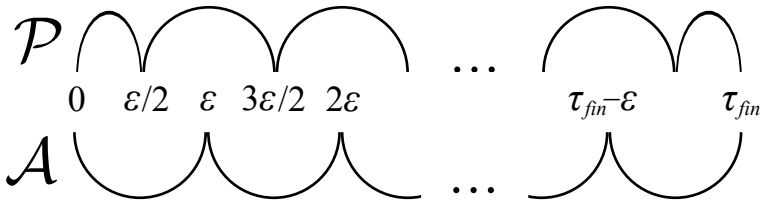

Figure 4.1: Schematic picture of a multi-step leap-frog evolution of A and P fields.

Fig. 4.1 shows a pictorial explanation of leap-frog's action on A and P. Leap-frog integrator introduces errors of order $\mathcal{O}(\varepsilon^2)$. They are corrected by the Metropolis step, however if the errors are too big the acceptance will become poor. This is why it is important to properly choose ε. In our calculations ε is set so that the acceptance rates are approximately between 0.7 and 0.85.

Most of the calculations presented in this work were done using the leap-frog algorithm. There exist however more advanced integrators, systematically studied in Ref. [70] by Omelyan et al. (hence the commonly used name "Omelyan integrators"). Recently, we have implemented the second order minimum-norm (2MN) integrator [70, 71]. It requires two calculations of $\frac{\partial S}{\partial A}$ ("force calculations") per MD step, i.e. it is approximately twice as costly as the leap-frog, however the resulting difference between the final and the initial hamiltonian (ΔH) is an order of magnitude smaller in the case of 2MN (for the same ε). This gives a significant speed-up of the algorithm and 2MN is the integrator-of-choice in our current calculations[1].

[1]There is also a possibility to use the higher-order integrators analyzed in Ref. [70], e.g. the ones that introduce $\mathcal{O}(\varepsilon^4)$ errors. We have implemented the fourth order integrator 4MN4FP (we follow the naming convention of Ref. [71]) that requires 4 force calculations per MD step. It gives ΔH much smaller than 2MN, however in practice we found its efficiency to be inferior to 2MN at the system sizes we currently use – its practicality should increase as one goes to larger systems than the ones we can currently achieve.

4.2 Hybrid Monte Carlo – application to $N_f = 2$ AEK

4.2.1 Introduction

The action for the $N_f = 2$ AEK model is

$$S[U] = S_{\text{gauge}}[U] - \ln(\det D[U])^2 \,, \tag{4.9}$$

where S_{gauge} is the Wilson plaquette action defined in Eq. 3.2, and the (Wilson) Dirac operator is defined in Eq. 3.3.

The explicit calculation of the fermionic determinant is very costly and the way to avoid it is to introduce pseudofermion fields. The determinant is real due to the γ_5-hermiticity of the Dirac operator:

$$\gamma_5 D \gamma_5 = D^\dagger. \tag{4.10}$$

Thus we can write:

$$(\det D)^2 = \det D \det D^\dagger = \det(DD^\dagger). \tag{4.11}$$

Next we note that one can interpret the determinant as a result of a bosonic integral:

$$\det(DD^\dagger) = \frac{1}{\det(DD^\dagger)^{-1}} = Const. \int \mathcal{D}[\phi] \mathrm{e}^{-\phi^\dagger (DD^\dagger)^{-1} \phi} \,, \tag{4.12}$$

where ϕ is a complex bosonic field with the same indices as the fermionic fields (hence the name pseudofermions). The last observation is that the action is indifferent to the substitution

$$D \to Q = D\gamma_5 \,, \quad Q = Q^\dagger. \tag{4.13}$$

We are now ready to write the HMC Hamiltonian for the $N_f = 2$ AEK model:

$$H = \frac{1}{2} \sum_\mu \mathrm{Tr}\,(P_\mu^2) - \frac{Nb}{2} \sum_{\mu \neq \nu} (\mathrm{Tr}\, U_{\mu\nu}^{\square} + h.c.) + \phi^\dagger Q^{-2} \phi \,. \tag{4.14}$$

P_μ are momenta conjugate to the gauge fields A_μ (the link variables $U_\mu = \exp(iA_\mu)$) – they are traceless hermitian $N \times N$ matrices, while the pseudofermion ϕ is a complex (bosonic) Dirac field in the adjoint representation (thus having $4(N^2-1)$ complex components).

The standard HMC algorithm produces momenta, gauge fields and pseudofermions distributed according to the probability density e^{-H}. This is done using the following steps, undertaken with a given "starting" set of U_μ:

- New momenta P_μ are drawn directly from the Gaussian distribution $\exp(-\mathrm{Tr}\, P_\mu^2/2)$.
- A new pseudofermion ϕ is obtained by first drawing a random pseudofermion field ψ from a Gaussian distribution, with weight $\exp\{-\mathrm{Tr}\,(\psi^\dagger\psi)\}$, and then setting

$$\phi = Q\psi\,. \tag{4.15}$$

- The initial Hamiltonian is evaluated. Note that the pseudofermion term in the action can be easily obtained from the Gaussian fields ψ.
- The Molecular Dynamics equations are then solved numerically using the leap-frog algorithm (or some more sophisticated integrator). The MD equation for the gauge field is

$$\dot{U}_\mu = iP_\mu U_\mu\,, \tag{4.16}$$

  while that for $\dot{P}_\mu$ must be determined by enforcing that $\dot{H} = 0$ (the specific calculations for AEK model are presented in the next subsection). The pseudofermion field ϕ is unchanged during the evolution.
- At the end of the MD trajectory the new fields U'_μ and P'_μ are obtained and the final Hamiltonian is evaluated using these fields. Finally, the Metropolis accept/reject step is performed, i.e. the new gauge configuration is accepted with probability Eq. 4.4.

One ends up with a (possibly) new set of U_μ and then repeats the steps.

4.2.2 Calculation of the HMC force

The right hand side of the Molecular Dynamics equation for $\dot{P}$ (called force in analogy with classical mechanics) corresponds to a change of the action with respect to an infinitesimal change in the gauge field (see Eq. 4.3):

$$U \to U\mathrm{e}^{i\omega}\,, \tag{4.17}$$

where ω is an infinitesimal traceless hermitian matrix. The force separates into the gluonic and fermionic part:

$$\dot{P}_\mu = \dot{P}_\mu{}^{U} + \dot{P}_\mu{}^{\phi}\,. \tag{4.18}$$

The former is

$$\dot{P}_\mu{}^{U} = iNb\sum_{\nu\neq\mu} U_\mu\left[U_\nu U_\mu^\dagger U_\nu^\dagger + U_\nu^\dagger U_\mu U_\nu\right] + h.c.\,. \tag{4.19}$$

Note that this result is automatically traceless and that it has the same structure as the large-volume HMC result (see e.g. Ref. [68]), despite different derivation – the large-volume gauge action is linear in $U_\mu(x)$ while the EK action is quadratic in U_μ.

To calculate the fermionic part we first express the variation of the pseudofermion action in terms of variation of $Q[U]$:

$$\phi^\dagger\delta(Q^{-2})\phi = -2\phi^\dagger\mathrm{Re}\{Q^{-2}\delta Q Q^{-1}\}\phi = -2\,\mathrm{Re}\{\chi^\dagger\delta Q\psi\} \tag{4.20}$$

where we have introduced

$$\chi = Q^{-2}\phi \quad\text{and}\quad \psi = Q\chi\,. \tag{4.21}$$

Next we use the explicit form of the Dirac operator, Eq. 3.3, and obtain the final result for the fermionic force:

$$\begin{aligned}\dot{P}_\mu{}^{\phi} = i(-\kappa)\Big\{&(\gamma_5-\gamma_\mu\gamma_5)_{\alpha\beta}\left[U_\mu\psi_\beta U_\mu^\dagger\chi_\alpha^\dagger - \chi_\alpha^\dagger U_\mu\psi_\beta U_\mu^\dagger\right]\\ &-(\gamma_5+\gamma_\mu\gamma_5)_{\alpha\beta}\left[\psi_\beta U_\mu\chi_\alpha^\dagger U_\mu^\dagger - U_\mu\chi_\alpha^\dagger U_\mu^\dagger\psi_\beta\right]\Big\} + h.c.\,.\end{aligned} \tag{4.22}$$

Again, the tracelessness of P_μ is maintained.

4.2.3 Some technical details

The most computationally expensive operation in HMC is the inversion of the Dirac operator. In the MD equation, the only place where we need the inversion of Q is the calculation of χ in Eq. 4.21. We use the fact that Q^2 is a hermitian positive definite operator and use Conjugate Gradients algorithm to obtain an iterative approximation to χ. In this way we never need to explicitly calculate the Dirac operator Q – we only need to calculate the action of Q^2 on a vector.

This greatly reduces the memory consumption of the algorithm and also allows significant CPU-time reduction[2]. It also allows us to avoid the explicit construction of the adjoint matrices U_μ^{adj}. Instead we represent the pseudofermion fields ϕ in the color space as a traceless hermitian matrix on which U_μ^{adj} acts as

$$U_\mu^{\mathrm{adj}}\phi \to U_\mu \phi U_\mu^\dagger. \tag{4.23}$$

In this way the action of Q on a vector only requires the multiplication of $N \times N$ matrices so it has the time scaling $\mathcal{O}(N^3)$.

We calculate the pseudofermion part of the final Hamiltonian in analogous manner. The only difference is a stronger stopping criterion of the CG. For the MD we require that the residue

$$r \equiv \phi - Q^2\chi \tag{4.24}$$

satisfies $|r|/|\phi| < 10^{-5}$. The accept-reject step compensates for any errors introduced due to the truncation of the CG so we only need to take care that the lower precision does not affect the acceptance rate too much. In the accept-reject step, on the other hand, we need to assure that the precision

[2]That is, unless the number of CG iterations N_{CG} grows proportionally to N – a possibility that cannot be easily excluded in the volume-reduced case where Q is a dense matrix. The actual scaling, however, ranges from $\mathcal{O}(N^0)$ to $\mathcal{O}(N^{1/2})$ as will be discussed further in this section. The matter is more obvious in the large-volume simulations where Q is a sparse matrix or at least most of its values are very close to 0. The lack of a simple zero-structure in the volume-reduced case also greatly hampers the use of CG-preconditioners commonly used in the large-volume case. No preconditioning was used in the calculations presented in this work.

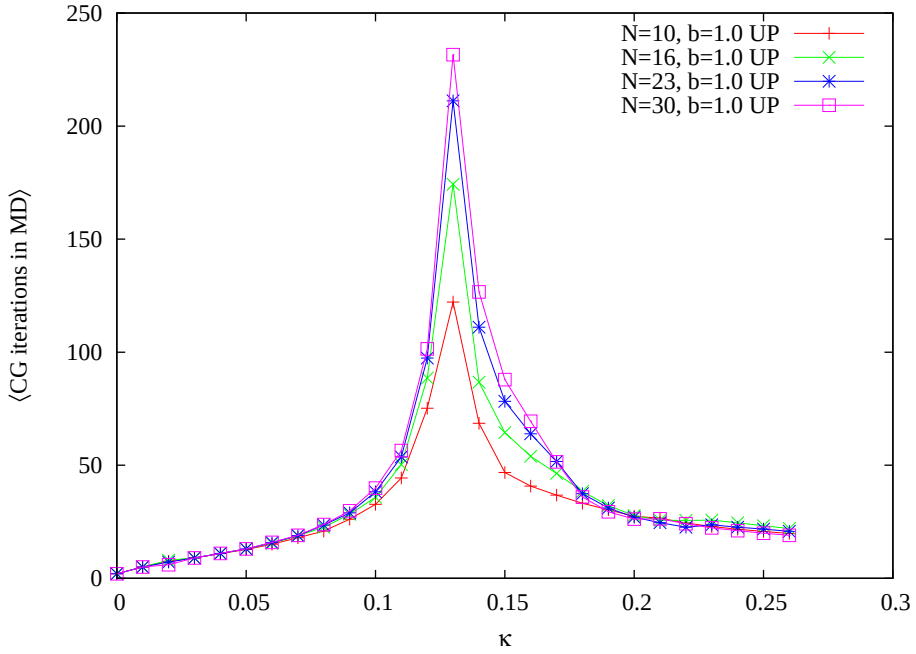

Figure 4.2: Average number of CG iterations in the MD updates for various N as a function of κ at $b = 1.0$, $\kappa_c \approx 0.13$.

is good enough so we use a stopping criterion $|r|/|\phi| < 10^{-15}$ which is comparable to the numerical precision of the exact inverter.

Next, we want to estimate the CPU-time scaling of the algorithm with N. To do that we need to know how the number of CG iterations, N_{CG} depends on N – we found that this depends on the quark mass. For the heavy quarks, away from the critical line κ_c, N_{CG} is independent of N (for a given stopping criterion) while for the light quarks (close to κ_c) it grows approximately as $N^{1/2}$. An illustration of this is given in Fig. 4.2.

The last ingredient of the time-scaling behaviour of the HMC algorithm is the number of MD steps per trajectory (for a given acceptance rate). We find it to grow approximately linearly with N. Thus the final CPU time scaling ranges from $\mathcal{O}(N^4)$ for heavy quarks to $\mathcal{O}(N^{4.5})$ for light quarks.

It is a common practice in large-volume simulations to use larger time steps for the fermionic force than for the gluonic force. This is based on the fact that the gluonic part of the force is typically much larger (i.e. the

fields change faster under its influence and have to be evaluated with larger accuracy). In our case we may expect that, since fermions play crucial role in the center symmetry restoration, their impact on the dynamics (and the corresponding size of the force) can be comparable to the gluonic one. We found that this is in fact the case in the Monte Carlo simulations (see Ref. [2] for details) so we conclude that using different time steps is not practical in our case.

Finally, almost all simulations in this work were done using serial code working on a single CPU core. Recently, we have implemented a parallel simulation code that can be efficiently executed on $(16 \times Volume)$ cores. This allows working with 16 cores on a single-site and 256 cores on 2^4 lattice. In this work, only one result obtained with the new code is presented – see Sec. 5.3.2.

4.3 Simulation of $N_f = 1$ AEK – Rational Hybrid Monte Carlo

4.3.1 The rational approximation

When trying to construct the HMC algorithm for odd number of flavours we encounter several problems of both conceptual and technical nature. First, we note that although the fermionic determinant in the models we analyze is always positive [45], there may exist gauge configurations where some eigenvalues of the Wilson Dirac operator will have a negative real part. This invalidates the concept of the pseudofermion integral and to protect from that, we replace $\det D$ with

$$\det |D| = \det \sqrt{DD^\dagger} = \det |Q| = Const. \int \mathcal{D}[\phi] \mathrm{e}^{-\phi^\dagger |Q|^{-1} \phi}, \qquad (4.25)$$

where Q is the hermitian operator defined in Eq. 4.13.

Explicit calculation of $|Q|^{-1}$ is, however, very costly and one has to rely on some sort of approximation – we choose the Zolotarev optimal rational

approximation:

$$\mathcal{R}(x) = A\prod_{i=1}^{n}\frac{(x+c_{2i-1})}{(x+c_{2i})} = A\left(1+\sum_{i=1}^{n}\frac{r_i}{x+a_i}\right) \xrightarrow[n\to\infty]{} 1/\sqrt{x}, \qquad (4.26)$$

where he coefficients A, a_i, r_i are set to minimize the error (see e.g. Ref. [68] for an accessible review or Ref. [72] for a more in-depth treatment):

$$\delta = \max_{\varepsilon\le x\le 1} |1-\sqrt{x}\mathcal{R}(x)|. \qquad (4.27)$$

If the spectrum of Q^2 is contained in $[\varepsilon M^2, M^2]$ then the approximation we need is

$$|Q|^{-1} \simeq \frac{1}{M}\mathcal{R}(Q^2/M^2) \equiv R\,. \qquad (4.28)$$

To protect ourselves from any imperfections of the approximation we introduce additional correcting pseudofermion field ϕ_{corr} and write the determinant as:

$$\det|Q| = Const.\int \mathcal{D}[\phi,\,\phi_{corr}]\,\exp\left\{-\phi^\dagger R\,\phi - \phi^\dagger_{corr}(|Q|R)^{-1}\phi_{corr}\right\}. \qquad (4.29)$$

If the quality of the approximation is good, then the operator $|Q|R$ is close to identity and has a very weak dependence on the gauge configuration. Thus using only ϕ in the Molecular Dynamics should not affect the acceptance rate very much.

4.3.2 Changes compared to $N_f = 2$

Compared to the $N_f = 2$ case, there are three parts of the algorithm that need to be changed for the Rational Hybrid Monte Carlo (RHMC):

1. Generation of the pseudofermion fields: we generate fields ψ and ψ_{corr} with Gaussian distribution and calculate

$$\phi = C\psi\,,\quad \phi_{corr} = B\psi_{corr}\,, \qquad (4.30)$$

where $C^\dagger C = R^{-1}$ and $B^\dagger B = |Q|R$.

Operator C that fulfills the above condition can be easily found from Eq. 4.26:

$$C = \sqrt{\frac{M}{A}} \prod_{i=1}^{n} \frac{(Q/M + i\sqrt{c_{2i-1}})}{(Q/M + i\sqrt{c_{2i}})}. \tag{4.31}$$

To find B note that the operator

$$Z = Q^2 R^2 - 1 \tag{4.32}$$

is very small (of order δ) so one only needs the first few terms of the power series:

$$B = (1+Z)^{1/4} = 1 + \tfrac{1}{4}Z - \tfrac{3}{32}Z^2 + \dots \tag{4.33}$$

to compute B up to the machine precision [68].

2. Calculation of the pseudofermion contribution to the Hamiltonian for the Metropolis step. The initial Hamiltonian can be calculated from ψ and ψ_{corr}. The final Hamiltonian however requires calculation of $R\phi$ and $(|Q|R)^{-1}\phi_{corr}$. The latter can be found as a power series in Z.

3. Calculation of the fermionic force in the Molecular Dynamics equations. The variation of the $\phi^\dagger R\,\phi$ part is (remember that we do not include ϕ_{corr} in the MD):

$$\begin{aligned}
\phi^\dagger \delta R\,\phi &= \frac{A}{M}\sum_{i=1}^{n} r_i \phi^\dagger \delta\left((Q^2/M^2 + a_i)^{-1}\right)\phi = \\
&= -\frac{2A}{M^3}\sum_{i=1}^{n} r_i \phi^\dagger \mathrm{Re}\{(Q^2/M^2 + a_i)^{-1}\delta Q\, Q\,(Q^2/M^2 + a_i)^{-1}\}\phi = \\
&= -\frac{2A}{M^3}\sum_{i=1}^{n} r_i\, \mathrm{Re}\{\chi_i^\dagger \delta Q \psi_i\},
\end{aligned} \tag{4.34}$$

where

$$\chi_i = (Q^2/M^2 + a_i)^{-1}\phi \quad \text{and} \quad \psi_i = Q\chi_i\,. \tag{4.35}$$

From Eq. 4.34 we see that the force is nothing but a sum of terms equivalent to the force in the $N_f = 2$ HMC (compare Eq. 4.21).

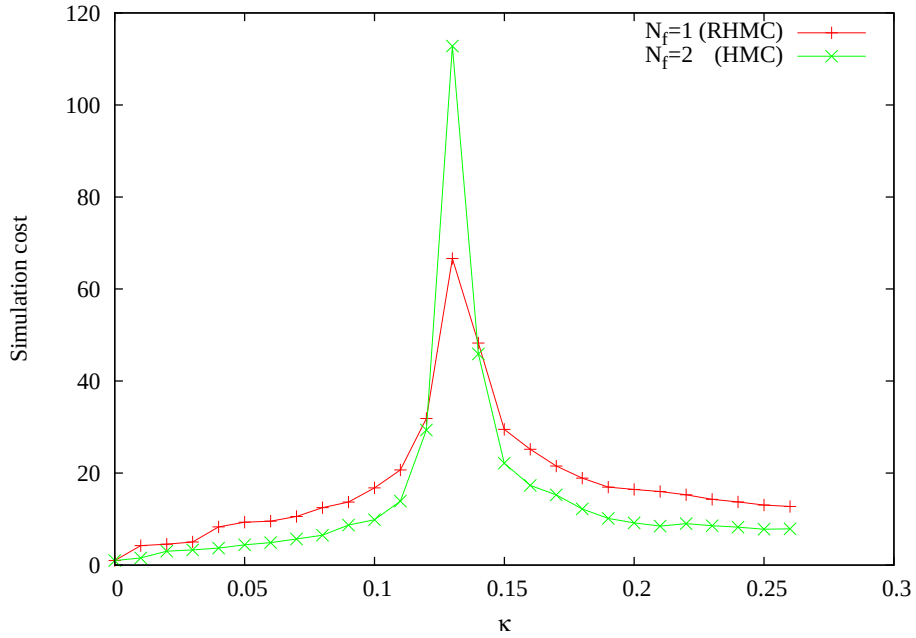

Figure 4.3: Example comparison of simulation cost of $N_f = 1$ and $N_f = 2$ simulations for a representative scan. We define the simulation cost as the CPU time per HMC trajectory divided by the average acceptance rate and we normalize it to the pure-gauge value (set to one). The results are presented as a function of κ at $N = 16$, $b = 1.0$.

Note that the shifted structure of Eqs. 4.35 allows their simultaneous solution at the cost of solving the single (most expensive) equation, using the multi-shift Krylov solver CG-M [73]. Similar calculations can be applied to other parts where the approximation is used.

Calculating C in the pseudofermion generation, Eq. 4.31, is the only place where we need to invert a matrix that is not hermitian positive definite – we do this using CGNE-M algorithm (which is a combination of standard CGNE with the multi-shift solver CG-M – the normal equations preserve the shifted structure).

It is interesting to compare the cost of the $N_f = 1$ and $N_f = 2$ simulations. An example comparison is presented in Fig. 4.3. The first observation is that in both cases the simulation becomes much more costly as one ap-

proaches κ_c (even by two orders of magnitude). In the analyzed case the cost of the simulation for heavy fermions is roughly two times bigger for the RHMC algorithm than for the ordinary HMC. As we get closer to κ_c the additional overhead due to the rational approximation becomes less significant and at $\kappa = 0.13$ we can see that the result for $N_f = 2$ is in fact much larger. This is most likely caused by a smaller physical quark mass which requires more CG iterations in the two-flavour case (κ_c have different values for the two models due to a different additive renormalization).

Chapter 5

Phase diagram of the AEK model

The ultimate goal of the volume reduction technique is to use the single-site model to extract the properties of physical (large-volume) systems. To do that we must first determine the values of parameters of the AEK model for which the center symmetry is unbroken. In this section we present the methods and the numerical results used to establish these values. The sketch of the deduced phase diagram in the $\kappa - b$ plane (cf. Eqs. 1.12, 1.15) is presented in Figure 5.1.

The main feature of the phase diagram is the presence of a broad region of parameters in which the $\mathbb{Z}_N^4$ center symmetry is intact. Due to its funnel-like shape we call this region the center-symmetric "funnel". In this region the large-N volume reduction holds and the measurements of observables can be mapped to the large-volume ones. The smallest value of κ (for given b) at which the center-symmetry is unbroken is denoted as κ_f.

This chapter mostly presents the results for $N_f = 2$ contained in Ref. [2] with some minor extensions. We find that the results in $N_f = 1$ are very similar and thus we only show a limited number of plots for this case – the only substantial difference is the width of the center-symmetric funnel and we present the results for both cases in Sec. 5.3.2.

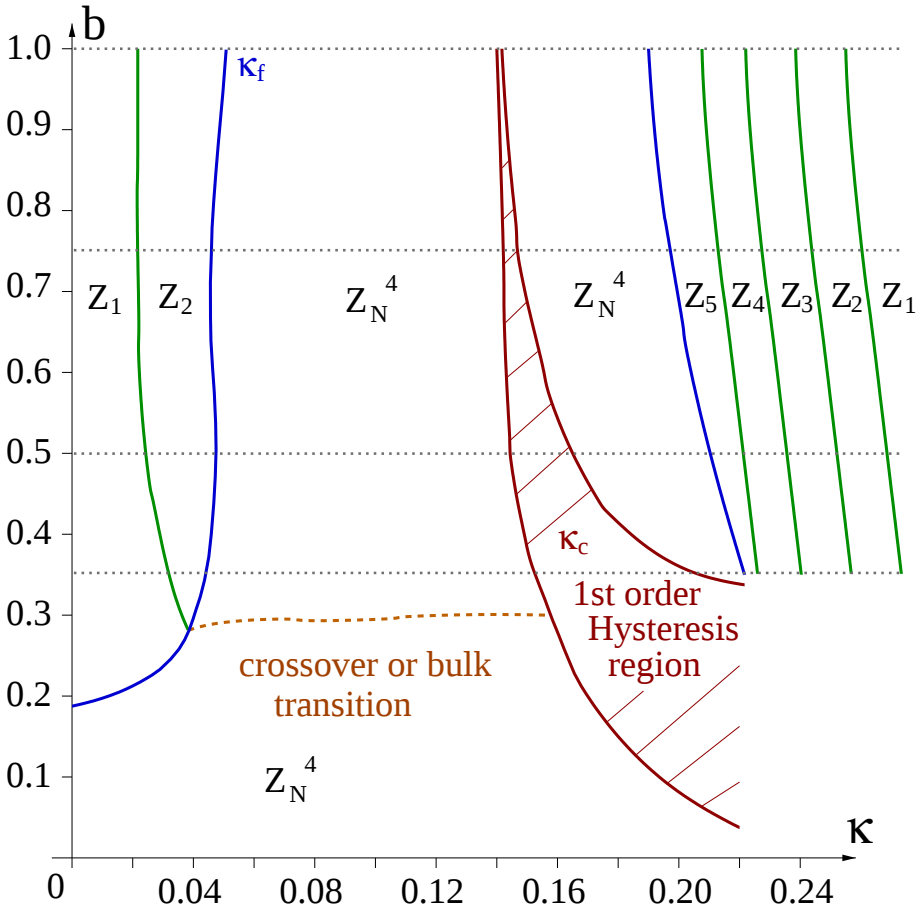

Figure 5.1: Sketch of the phase diagram for the $N_f = 2$ AEK model with $N \approx 30$ (a completely analogous picture is valid for $N_f = 1$). The region named $\mathbb{Z}_N^4$ is the center-symmetric funnel in which the volume reduction is valid. Surrounding it, there are several phases named $\mathbb{Z}_1$-$\mathbb{Z}_5$ after the pattern of partial breaking of the center symmetry (the phases are labeled $\mathbb{Z}_K$, not $\mathbb{Z}_K^4$ because every time we observe the center symmetry breaking there are substantial correlations between different lattice directions, see Sec. 5.2). $\mathbb{Z}_1$ is the name for the region where the center symmetry is completely broken (as in the pure-gauge EK model, that is represented by the $\kappa = 0$ line). The grey dotted lines denote the values of b used for scans in Sec. 5.2.

5.1 Measured quantities

Observables used to detect the center symmetry breaking are the general open loops:

$$K_n = \tfrac{1}{N}\mathrm{Tr}\; U_1^{n_1} U_2^{n_2} U_3^{n_3} U_4^{n_4}, \quad \text{with} \;\; n_\mu = 0, \pm 1, \pm 2, \ldots \tag{5.1}$$

where $U^{-n} \equiv U^{\dagger n}$. These loops transform non-trivially under the center symmetry (unless all n_μ are integer multiples of N) and are thus very general order parameters for the center-symmetry breaking. We put the most focus on the simplest examples of such loops, which are the 4 Polyakov loops:

$$P_\mu = \tfrac{1}{N}\mathrm{Tr}\, U_\mu \tag{5.2}$$

and the 12 "corner variables":

$$M_{\mu\nu} = \tfrac{1}{N}\mathrm{Tr}\, U_\mu U_\nu \quad \text{and} \quad M_{\mu,-\nu} = \tfrac{1}{N}\mathrm{Tr}\, U_\mu U_\nu^\dagger \tag{5.3}$$

with $\mu \neq \nu$. The corner variables were found to be particularly helpful in finding the center symmetry breaking in the Quenched Eguchi-Kawai model [23] because of their sensitivity to partial $\mathbb{Z}_N^4$ breakings[1], also the ones including correlations between different lattice directions.

We also analyze the more complicated open loops, although to keep the quantity of data manageable, we limit ourselves to $-5 \leq n_\mu \leq 5$. In this case the loops are not sensitive to more complicated patterns of partial symmetry breaking, e.g. $\mathbb{Z}_N^4 \to \mathbb{Z}_{10}$. To be able to observe such patterns we analyze the eigenvalues of link matrices. As already noted in Sec. 3.2 each link can be represented as

$$U_\mu = V_\mu D_\mu V_\mu^\dagger, \quad \text{with} \;\; D_\mu = \mathrm{diag}[e^{i\vartheta_\mu^1}, e^{i\vartheta_\mu^2}, \ldots, e^{i\vartheta_\mu^N}] \tag{5.4}$$

The single-site gauge transformation $U_\mu \to \Omega U_\mu \Omega^\dagger$ leaves the set of eigenvalues unchanged. In the center-symmetric phase one expects the distribution of phases ϑ_μ^a of link eigenvalues to be invariant under translations by $2\pi n/N$.

[1]The partial breaking of $\mathbb{Z}_N$ to $\mathbb{Z}_K$ $(1 < K < N)$ is observed when all the loops $\mathrm{Tr}\,[(U_\mu)^L]$ with $0 < L < K$ vanish but $\mathrm{Tr}\,[(U_\mu)^K]$ is non-zero.

The partial symmetry breaking can be detected when only a subgroup of the translational symmetry is unbroken.

If the coupling is not very strong one also expects that the partition function is dominated by the link matrices that are close to being simultaneously diagonalizable (see Sec. 3.2). One can then use the gauge freedom to set the U_1 to be diagonal (analogously to what was done in the perturbative calculation of Sec. 3.2.1) and analyze the elements of the other link matrices. In particular, the phases of the diagonal elements are expected to be close to the phases of the link eigenvalues and the correlations between them (and the exact eigenvalues of U_1) give extra input to the realization of the center symmetry (see Sec. 5.2).

Apart from the aforementioned observables we also use the average plaquette, described in Chapter 6, which is very helpful to map the gross features of the phase diagram.

5.2 Scans of $\kappa - b$ plane

To establish the center symmetry realization in the model we performed a series of scans in the $\kappa - b$ plane. The gross features of the phase diagram were analyzed with the scans in κ, at fixed b ("horizontal scans"). In these runs we used $N \leq 30$. The gathered information was later supplemented by looking at the selected points with greater precision and larger values of N (up to 53, and in one case up to 60). We also made several "vertical scans" (changing b at fixed κ).

We mostly focused on the range of $b \in [0.35, 1]$. This reaches from the non-perturbative regime above the bulk transition to a weakly coupled regime that can be compared to the perturbative calculations – e.g. for $N = 3$ this corresponds to the range of β between 6.3 and 18.

For the $N_f = 2$ case we also made several scans extending to the unphysical strongly-coupled phase (where the center symmetry is intact also in the pure-gauge case) as well as to extremely weakly coupled theory (up to $b = 200$). The values of κ were mostly in the range between 0 and 0.26

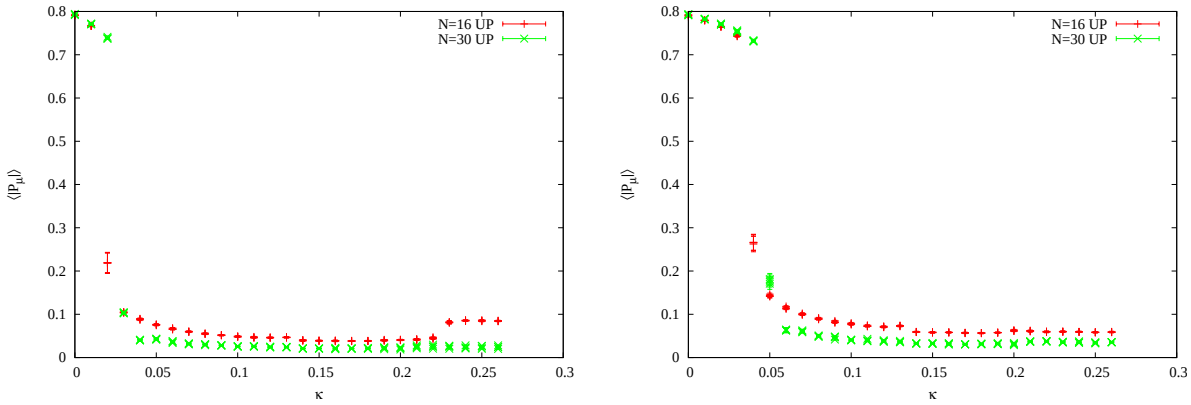

(a) $N_f = 2$ (b) $N_f = 1$

Figure 5.2: Absolute values of the Polyakov loops for $N = 16$ and 30, $b = 1.0$. All 4 directions are shown (in both panels).

but we also made some runs extending as far as $\kappa = 0.6$.

In particular, for both $N_f = 1$ and $N_f = 2$ we performed detailed scans at $b = 0.35, 0.5, 0.75, 1.0$ with $N = 10, 16, 23, 30$ for $\kappa \in [0, 0.26]$ measured every 0.01, both increasing the value of κ (called "UP" scans in the following) and decreasing κ (called "DOWN" or "DN" scans).

In Fig. 5.2 we present the example results of Polyakov loops measured in the runs at $b = 1.0$ for both values of N_f (for the sake of clarity, only the UP scans at $N = 16$ and 30 are plotted). At pure gauge, $\kappa = 0$, the absolute values of the Polyakov loops are clearly different from 0 signalling a spontaneously broken center symmetry, as expected. For $N_f = 2$, Fig. 5.2(a), at around $\kappa = 0.02 - 0.04$ there is a jump to significantly smaller values which suggest that the center symmetry is not broken, up to finite-N fluctuations[2]. The situation does not change throughout all higher values of κ up to κ_c, around 0.13, and beyond. There may be some concerns perhaps

[2]Note that, strictly speaking, one can only discuss phase transitions and spontaneous symmetry breaking in infinite systems so the terminology we use is only adequate for $N \to \infty$. In practice, however, spontaneous symmetry breaking is effectively observed in simulations at finite but large values of N and we keep using the language of phase transitions throughout this work.

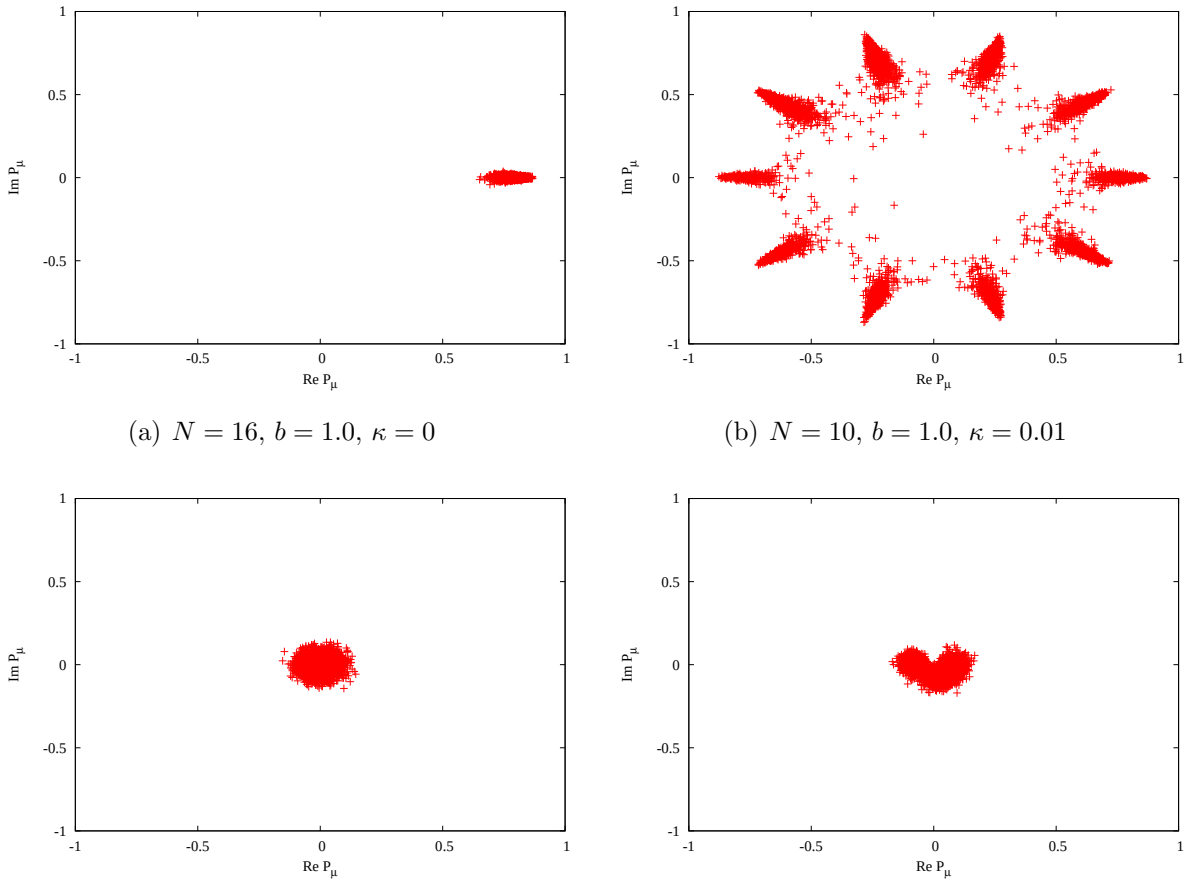

(a) $N = 16$, $b = 1.0$, $\kappa = 0$

(b) $N = 10$, $b = 1.0$, $\kappa = 0.01$

(c) $N = 16$, $b = 1.0$, $\kappa = 0.09$

(d) $N = 16$, $b = 1.0$, $\kappa = 0.25$

Figure 5.3: Scatter plots of Polyakov loops in the $N_f = 2$ model. All 4 directions are pictured together.

about the $N = 16$ run for $\kappa > 0.22$. For $N_f = 1$, Fig. 5.2(a), the situation is similar, however the transition to smaller absolute values of Polyakov loops takes place at higher values of $\kappa = 0.03 - 0.05$.

The picture is confirmed by looking at the scatter plots of the Polyakov loops in the complex plane, presented in Fig. 5.3 (for the $N_f = 2$ case). In the pure-gauge model, Fig. 5.3(a), the values of the Polyakov loops are close to 1, clearly forming a state with broken center symmetry. With smaller N one can observe tunneling between the different vacua with broken center symmetry, see Fig. 5.3(b). The tunneling is however suppressed as the

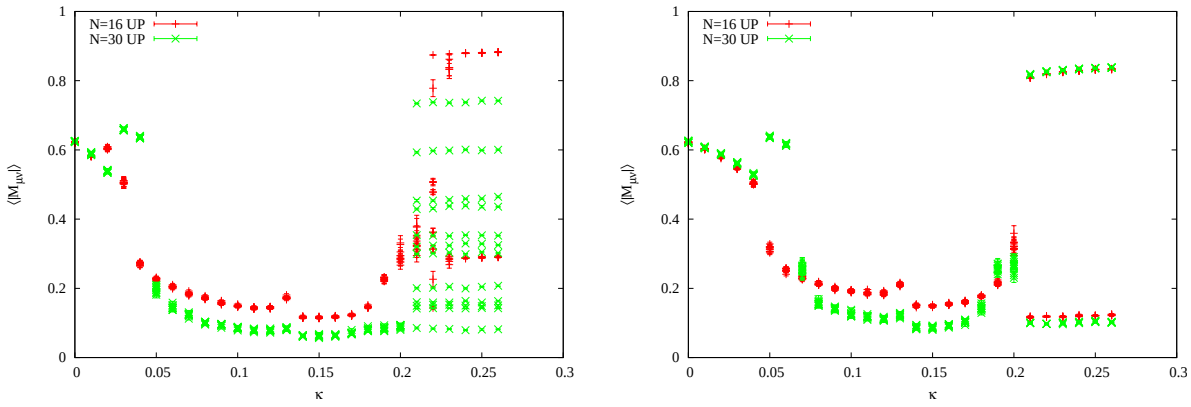

(a) $N_f = 2$ (b) $N_f = 1$

Figure 5.4: Absolute values of the corner variables for $N = 16$ and 30, $b = 1.0$. All 12 directions are shown (in both panels).

size of the system becomes larger. The run with $\kappa = 0.09$, Fig. 5.3(c), is on the other hand uniformly distributed around 0, signalling that the center symmetry is likely to be unbroken. The last plot, Fig. 5.3(d), is also distributed close to zero but the shape of the blob is rather asymmetric, signalling that there may occur a partial breaking of the $\mathbb{Z}_N^4$ symmetry.

We can further analyze the situation by looking at the corner variables $M_{\mu\nu}$, Fig. 5.4. They are sensitive to partial symmetry breaking, especially in the case where correlations between different directions are involved. We can see that the jump to $|M_{\mu\nu}|$ close to zero occurs at larger values of κ than in the case of Polyakov loops. Also, in the region $\kappa \gtrsim 0.2$ the corner variables are clearly non-zero (both for $N_f = 1$ and $N_f = 2$). We thus conjecture that the center-symmetric phase is separated from the completely broken phases by regions with partially broken symmetry.

This conjecture can be further verified by looking directly at the histograms of eigenvalues of U_μ. The link eigenvalues provide a more thorough test of the realization of the center symmetry than P_μ and $M_{\mu\nu}$ alone as they are sensitive also to patterns of symmetry breaking in which both of these loops vanish. From now on we focus on the $N_f = 2$ model. All the results presented in this section are analogous for the $N_f = 1$ case, except the

larger κ_f (which will be analyzed for both values separately in Sec. 5.3.2) and slightly larger finite-N corrections.

In Fig. 5.5 we present examples of the results that allow us to fill in the details of the phase diagram in Fig. 5.1. The phases of eigenvalues (defined in the range $\vartheta_\mu^a \in (-\pi, \pi]$) presented in each histogram are collected in $3N$ bins of width $2\pi/3N$ each. The $\mathbb{Z}_N$ symmetry implies that the histogram should be periodic under translation by multiples of 3 bins (up to the errors, that are proportional to the square root of the number of counts in each bin).

An example histogram inside the funnel is presented in Fig. 5.5(a). The distribution of ϑ_μ^a is invariant under $\mathbb{Z}_N$ translations and within errors it is consistent with being uniform. This is, in fact, a little surprising as the pure-gauge model is known to reproduce the Haar-measure-like probability density distribution in the unbroken phase [20]:

$$p(\vartheta_\mu^a) = \left(\frac{1}{2\pi} - \frac{(-1)^N}{N\pi} \cos(N\vartheta_\mu^a) \right), \tag{5.5}$$

which has visible oscillations in computer simulations (that vanish like $1/N$). As a check on our code, we have confirmed that the simulation reproduces this equation at $\kappa = 0$ with b below the bulk transition.

Outside the funnel the attraction between eigenvalues leads to the breaking of the center symmetry that manifests itself by a formation of groups ("clumps") of eigenvalues on the unit circle. By counting the number of clumps we can identify the approximate remnant symmetry ($\mathbb{Z}_k$-symmetric histogram has k clumps).

In Fig. 5.5 we show some examples of the clumping patterns – Figs. 5.5(b) and 5.5(c) show $\mathbb{Z}_1$ and $\mathbb{Z}_2$ phases on the l.h.s of the funnel (small κ region) while Figs. 5.5(d), 5.5(e) and 5.5(f) show $\mathbb{Z}_3$, $\mathbb{Z}_4$ and $\mathbb{Z}_5$ phases on the r.h.s. of the funnel (large κ region).

Note that the remnant symmetry is not always exact. For example, in Fig. 5.5(c) we find two clumps for $N = 23$ and in Fig. 5.5(d) three clumps for $N = 16$ – the eigenvalues cannot be equally distributed between the clumps and the symmetry is only approximate. Also in the case of Fig. 5.5(f) where

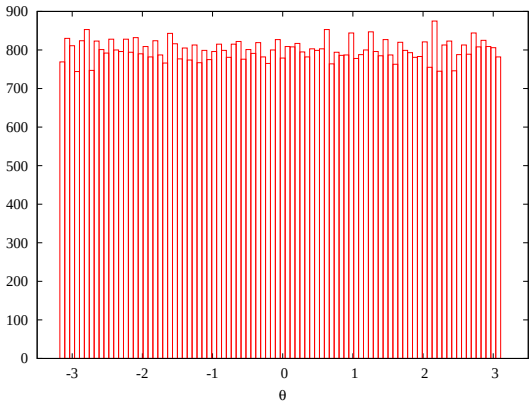

(a) $N = 30$, $b = 0.35$, $\kappa = 0.09$, 600 configs, all links

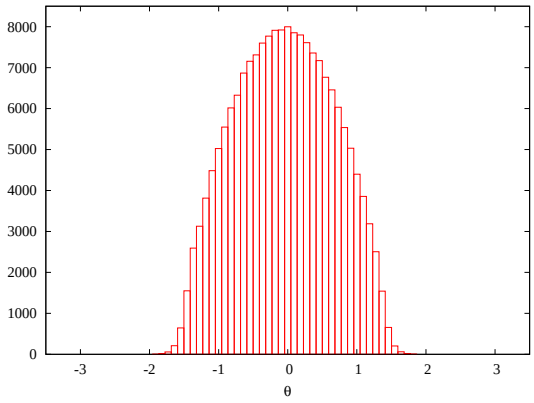

(b) $N = 23$, $b = 1.0$, $\kappa = 0.01$, 2000 configs, all links

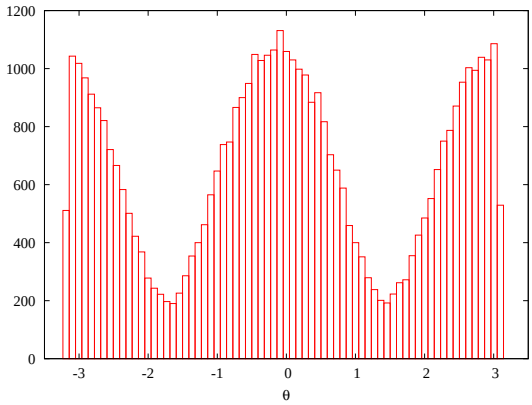

(c) $N = 23$, $b = 1.0$, $\kappa = 0.03$, 2000 configs, U_2 only

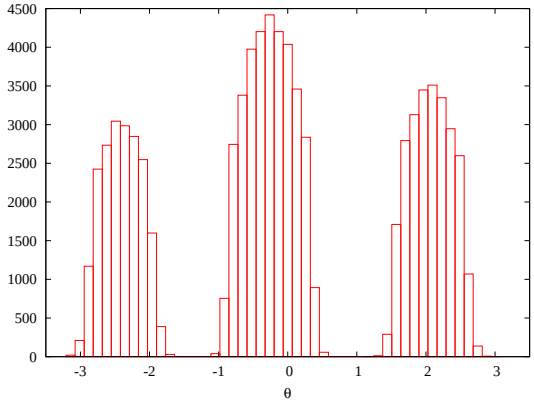

(d) $N = 16$, $b = 1.0$, $\kappa = 0.24$, 5000 configs, U_3 only

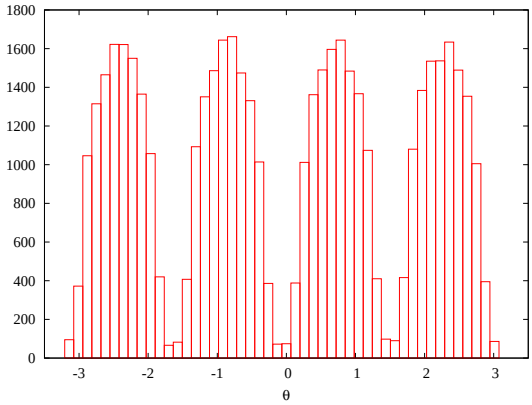

(e) $N = 16$, $b = 0.35$, $\kappa = 0.22$, 3000 configs, U_3 only

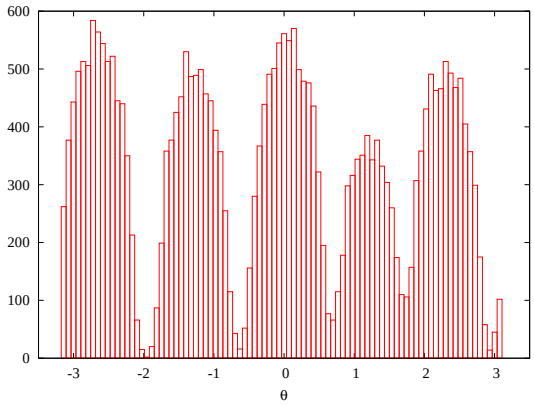

(f) $N = 30$, $b = 1.0$, $\kappa = 0.23$, 1000 configs, U_1 only

Figure 5.5: The (unnormalized) histograms of the phases ϑ_μ^a of the link eigenvalues. The uncertainties in each bin are of the order of $\sqrt{Number\ of\ counts}$. More details of the binning are discussed in the text.

there are five clumps for $N = 30$ we see that the clumps are not even and correspond to 7,6,7,6,4 eigenvalues respectively. We also find that different runs can have different patterns of clumping, e.g. 7,7,6,6,4 vs. 7,6,6,6,5, but that it is rare for the clumping to change during a run. Thus it appears that there are different competing "vacua" that are only approximately related by center symmetry transformations.

We can now understand the results given by the Polyakov loops and the corner variables. The Polyakov loops are practically insensitive to the partial symmetry breaking while the corner variables are giving various, sometimes complex, patterns in that case (cf. Fig. 5.4) – also in the case of more complicated patterns such as $\mathbb{Z}_5$ where we expect the "squared" Polyakov loop $\mathrm{Tr}\, U_\mu^2$ to be insensitive. Thus, as $M_{\mu\nu}$ involve links in different directions, we may expect that these complex patterns mean that there exist substantial correlations between the different links.

To measure this, at least at relatively weak coupling, we use the "time-like" gauge in which U_1 is diagonal, in a similar manner as in Section 3.2. At large b we expect that in this gauge the remaining links are also close to diagonal (cf. Eq. 3.5) and thus we can treat their diagonal elements "almost" as eigenvalues. In Fig. 5.6 we see an example configuration which shows that even at b as low as 0.35 the diagonal dominance is very clear (at least for $\kappa > \kappa_c$; for $\kappa < \kappa_c$ the diagonal dominance is only clear for $b \gtrsim 1.0$).

Fig. 5.7 presents the phases of U_μ in 20 configurations collected in a run with the same parameters as in Fig. 5.6. We set the gauge in such a way that the phases of eigenvalues of U_1 are ordered – note that no ambiguity exists in the ordering of the remaining diagonal elements once we specify the order for U_1. We see three clumps of sizes 6,4,6 that, while being positioned at different angles, are almost completely correlated between all four links, and do not change during the Monte Carlo evolution. Because of these correlations, seen every time when the center symmetry is broken, we infer that the approximate remnant symmetry of Fig. 5.6 is $\mathbb{Z}_3$, not $\mathbb{Z}_3^4$.

Ref. [61] argues that one should expect that the number of clumps should become smaller as one gets further away from the funnel (i.e. as the quark

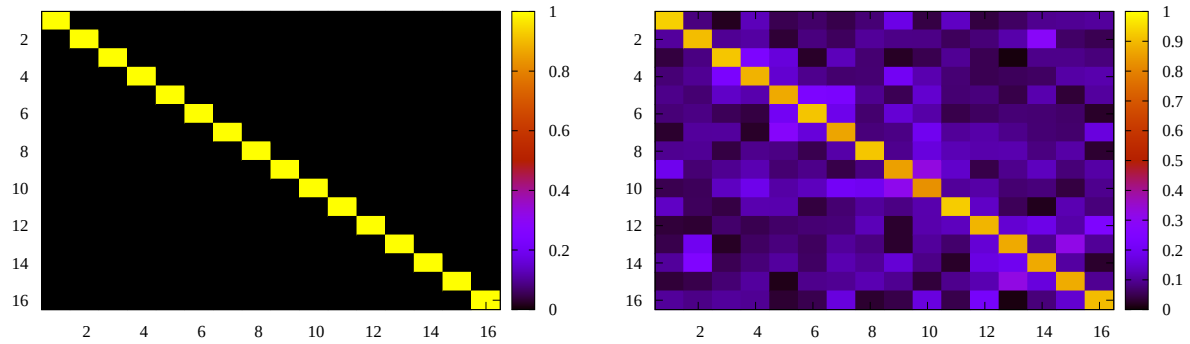

(a) U_1

(b) U_2

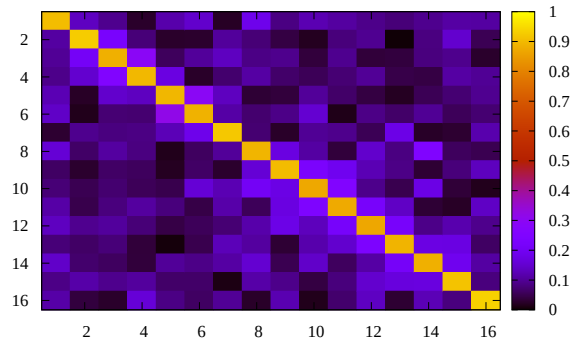

(c) U_3

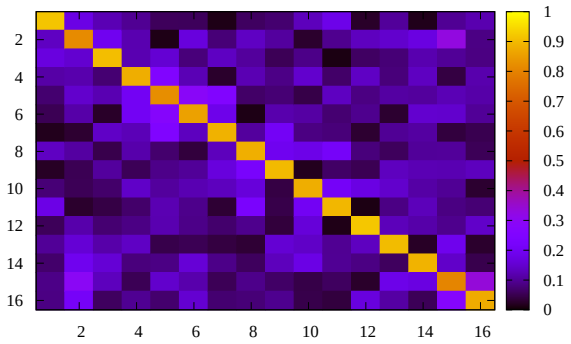

(d) U_4

Figure 5.6: Absolute values of link elements in the "timelike" gauge – an example configuration at $N_f = 2$, $N = 16$, $b = 0.35$, $\kappa = 0.23$. The diagonal elements are clearly the largest ones.

mass gets higher). That is indeed what we observe. On the large-κ side we extended some scans up to $\kappa = 0.6$. We find that ϑ_μ^a in the UP scans form less and less clumps after leaving the funnel, until they end up in a two clump state. The DOWN scans, started from an ordered start, begin with a single clump and as κ is decreased have a transition to two clumps. The transition appears to occur in stages where the eigenvalues gradually "peel off" from the original clump. As κ is further decreased, there appear more and more clumps until we enter the funnel and the eigenvalues become uniformly distributed on the unit circle. The largest number of clumps depends on N, and the largest we have observed is five, as shown

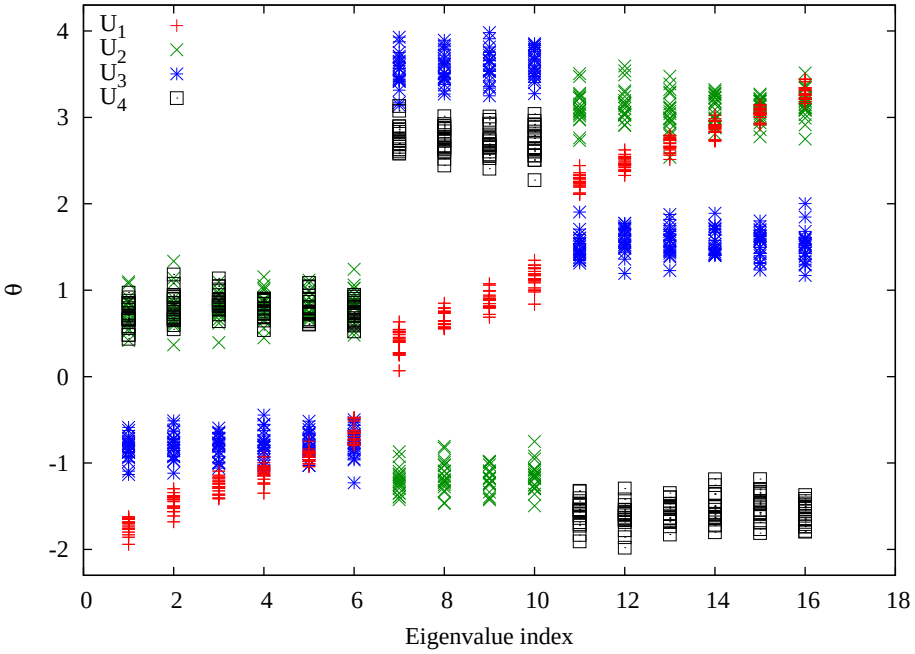

Figure 5.7: Phases of the diagonal elements of U_μ, in the gauge where U_1 is diagonal and its phases are ordered, for 20 thermalized configurations at $N_f = 2$, $N = 16$, $b = 0.35$, $\kappa = 0.23$. The phase is $\mathbb{Z}_3$ and the range of the phases was adjusted so as to avoid the cut through one of the three clumps.

in Fig. 5.5(f).

One expects a similar phenomenon on the small-κ side. In fact, as we increase κ (thus reducing the quark mass) from 0 we encounter similar transitions although the maximum number of clumps before entering the funnel is significantly smaller in this region. For $N < 23$ we only observe the $\mathbb{Z}_1$ phase, for $23 \leq N < 47$ we see $\mathbb{Z}_1$ and $\mathbb{Z}_2$, while for $N = 47$ and 53 we find $\mathbb{Z}_1$, $\mathbb{Z}_2$ and $\mathbb{Z}_3$ phases. The arguments of Ref. [61] imply that the maximum number of clumps should increase with b. Indeed, that is what we observe – for $b > 1$ the phase $\mathbb{Z}_3$ appears at smaller values of N.

We have also checked the results given by the higher-order open loops defined in Eq. 5.1, following the method of Ref. [45], as well as performed several vertical scans in the $\kappa - b$ plane to supplement our knowledge of the phase diagram. We found that these calculations confirm the results

presented earlier in this section and, for the sake of brevity, we do not present them here.

5.3 The width of the center-symmetric funnel

5.3.1 The N-scaling of P_μ and $M_{\mu\nu}$

The encouraging results of the previous section lead to the crucial question – what happens to the center-symmetric funnel as $N \to \infty$? In order to study the large-N limit we have extended the calculations to larger values of N in several points of the $\kappa - b$ plane.

Let us begin with the large-N extrapolations of $\langle |P_\mu|^2 \rangle$ and $\langle |M_{\mu\nu}|^2 \rangle$. In the $N \to \infty$ limit they are equal to $|\langle P_\mu \rangle|^2$ and $|\langle M_{\mu\nu} \rangle|^2$ (cf. Eq. 1.16) – which are both equal to zero if the center symmetry is unbroken. Thus an important check of the proposed phase diagram, presented in Fig. 5.1, is that both these values extrapolate to 0 in the tentative center-symmetric funnel.

Ordinarily finite-N effects are $\mathcal{O}(1/N^2)$ but in the volume-reduced models one can also encounter $\mathcal{O}(1/N)$ corrections (see Sec. 6.1). In Fig. 5.8 we show $\langle |P_1|^2 \rangle$ as a function of $1/N^2$ for two representative points in the $\kappa - b$ plane. Although the $1/N^2$ term is clearly the largest finite-N contribution in many cases we found that pure $1/N^2$ fits have large values of χ^2/d.o.f.. Addition of $1/N$ term as well as dropping the 2 lowest values of N (10 and 16) lead to satisfactory fits in all analyzed cases – the values of the fit parameters are collected in Table 5.1. The coefficients of the $1/N$ term are small in all cases, and in fact consistent up to $\sim 3\sigma$ with zero except for $b = 0.35$, $\kappa = 0.06$. We also show the results of fits to $1/N^2$ plus a constant term – the fits are of similar quality and the constant term is consistent with 0 except, again, the point $b = 0.35$, $\kappa = 0.06$. We conclude that (except this one point near the edge of the tentative funnel) the behaviour of Polyakov loops is consistent with hypothesis that the center symmetry is

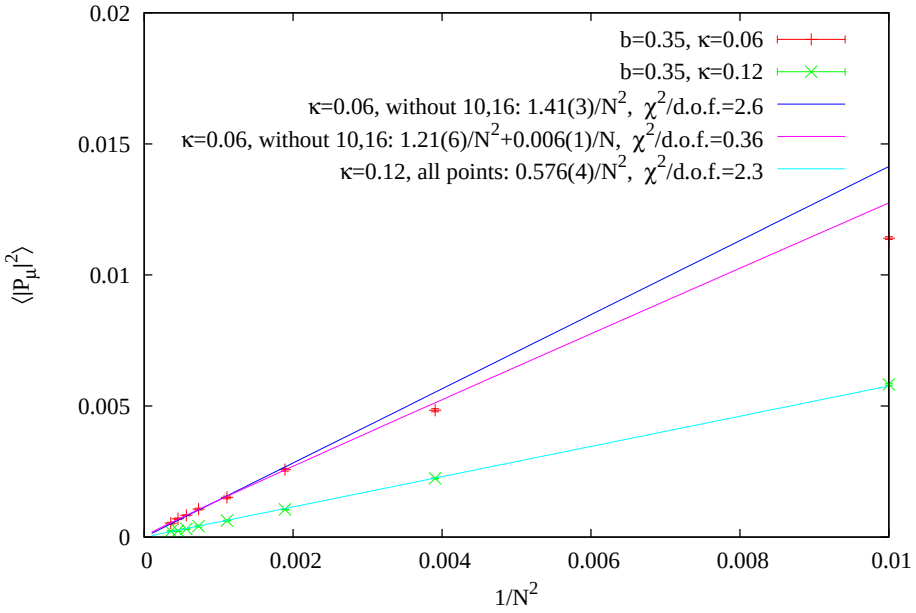

Figure 5.8: Large-N extrapolations of $\langle|P_1|^2\rangle$ for $N_f = 2$, $b = 0.35$ and two values of κ: 0.06 and 0.12. The values of N are 10, 16, 23, 30, 37, 42, 47 and 53.

intact in the funnel.

Example data for the corner variables are presented in Fig. 5.9. The particularly striking is the data at $b = 0.35$, $\kappa = 0.06$ – the pictured $\langle|M_{12}|^2\rangle$ begins to rise for $N \gtrsim 40$ and clearly does not extrapolate to zero. This result is rather surprising as otherwise there is no clear sign of breaking of the center symmetry – for all analyzed values of N, $M_{\mu\nu}$ as well as other open loops from Eq. 5.1 are distributed approximately near the origin and the distribution of link eigenvalues is consistent with uniform.

Our interpretation is that the increase in $\langle|M_{\mu\nu}|^2\rangle$ with N is due to the lower edge of the funnel, κ_f, increasing with N (possibly reaching $\kappa_f > 0.06$ in the large-N limit)[3]. In that case, we might be able to observe clear signal of $\mathbb{Z}_N^4$ symmetry breaking at higher values of N and the hints of the transition are already visible in the values we use due to the vicinity of

[3]This effect can be also observed (for $b = 1.0$) in Fig. 5.4 where the jump in the corner variables for $N = 30$ is at visibly higher values of κ than for $N = 16$.

Qty	b	κ	c_1	c_2	$\frac{\chi^2}{\text{d.o.f.}}$	c_0'	c_2'	$\frac{\chi'^2}{\text{d.o.f.}}$
$\langle\|P_1\|^2\rangle$	0.35	0.06	0.006(1)	1.21(6)	0.36	$9(1)\times10^{-5}$	1.31(1)	0.39
$\langle\|P_1\|^2\rangle$	0.35	0.09	0.0014(9)	0.73(3)	0.67	$2(1)\times10^{-5}$	0.76(2)	0.73
$\langle\|P_1\|^2\rangle$	0.35	0.12	0.001(3)	0.57(3)	0.82	$0(2)\times10^{-5}$	0.56(1)	0.84
$\langle\|M_{12}\|^2\rangle$	0.35	0.09	0.152(5)	2.9(1)	0.42	0.0023(3)	5.3(4)	2.57
$\langle\|M_{12}\|^2\rangle$	0.35	0.12	0.036(6)	3.5(2)	1.0	$5(1)\times10^{-4}$	4.1(2)	1.2
$\langle\|P_1\|^2\rangle$	1.0	0.06	$-0.0001(3)$	1.17(1)	0.025	$-1(3)\times10^{-6}$	1.17(1)	0.025
$\langle\|P_1\|^2\rangle$	1.0	0.09	$-0.0003(4)$	0.70(1)	1.2	$-5(6)\times10^{-6}$	0.70(1)	1.2
$\langle\|P_1\|^2\rangle$	1.0	0.12	$-0.0010(3)$	0.55(1)	0.60	$-1.4(4)\times10^{-5}$	0.54(1)	0.58
$\langle\|M_{12}\|^2\rangle$	1.0	0.06	0.69(3)	-1.6(7)	0.58	0.010(1)	9(2)	2.7
$\langle\|M_{12}\|^2\rangle$	1.0	0.09	0.0053(7)	6.1(2)	0.99	$8(2)\times10^{-4}$	6.9(3)	1.7
$\langle\|M_{12}\|^2\rangle$	1.0	0.12	0.01(1)	5.5(4)	0.4	$0(1)\times10^{-4}$	5.4(2)	0.41

Table 5.1: Results from fits to the large-N behavior of $\langle|P_1|^2\rangle$ and $\langle|M_{12}|^2\rangle$ in the $N_f = 2$ case [2]. Fits are to $N = 23$, 30, 37, 42, 47 and 53 using $f_1(N) = c_1/N + c_2/N^2$ and $f_2(N) = c_0' + c_2'/N^2$, showing statistical errors.

increasing κ_f. The results for $M_{\mu\nu}$ also explain why the P_μ fits were less satisfactory in this point.

For all other analyzed points we find that the corner variables decrease monotonically with N. As for the Polyakov loops, the $1/N^2$ fits are rather poor but the addition of $1/N$ term leads to acceptable fits in all cases (note that contrary to the P_μ case the $1/N$ terms differ significantly from 0). The fits to $1/N^2$ plus constant lead to small but often non-zero constant values but they also usually have higher χ^2/d.o.f. than the $c_2/N^2 + c_1/N$ fits – we thus conclude that the latter fits are the most reasonable ones[4].

[4]We have also experimented with fits to $c_2/N^2 + c_4/N^4$ (an example is shown in Fig. 5.9) but the fits require very large coefficients with opposite sign to give a satisfying quality – we consider such fine tuning as very unlikely to be the correct description.

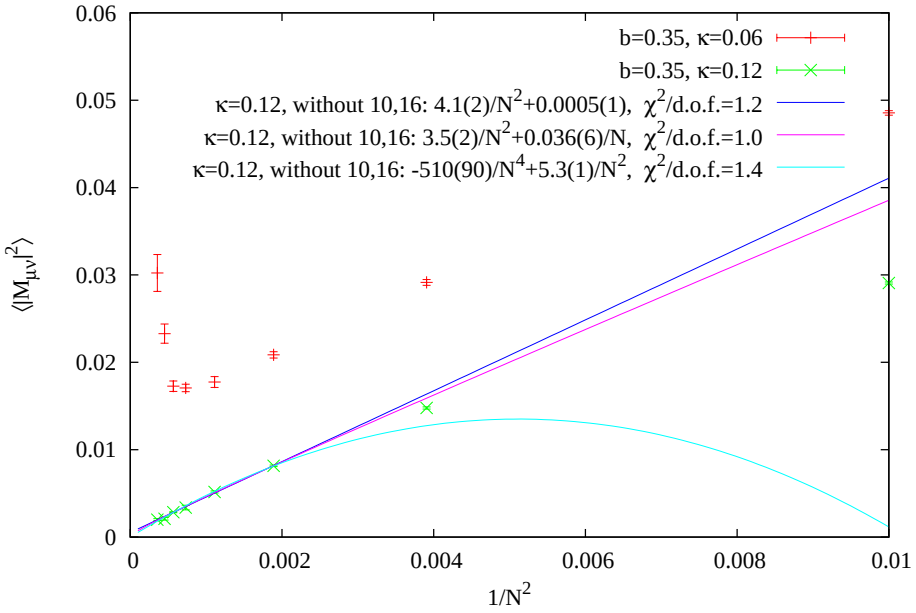

Figure 5.9: Large-N extrapolations of $\langle|M_{12}|^2\rangle$ for $N_f = 2$, $b = 0.35$ and two values of κ: 0.06 and 0.12.

5.3.2 Funnel width as $N \to \infty$

The presented results suggest that the center symmetry is in fact unbroken in a sizeable region of parameters, but there remains some anxiety whether κ_f does not in fact converge to κ_c in the large-N limit – in that case the reduction with massive fermions may only be apparent for some low enough values of N (as in the $b = 0.35, \kappa = 0.06$ case).

To resolve this matter it is important to study the function $\kappa_f(N)$ and to perform its large-N extrapolation. To investigate this we have performed a series of fine scans of the small κ region. An example is pictured in Fig. 5.10. There are two phases with broken center symmetry before we enter the funnel: the system is in the $\mathbb{Z}_1$ phase in the region $0 \leq \kappa \lesssim 0.02$ and in the $\mathbb{Z}_2$ phase in $0.02 \lesssim \kappa \lesssim 0.05$. The transition between the first and the second phase shows a significant hysteresis while that between the second phase and the funnel does not – we will discuss the possible order of this phase transition in the following part of this section.

A reliable large-N extrapolation of $\kappa_f(N)$ requires very costly analysis

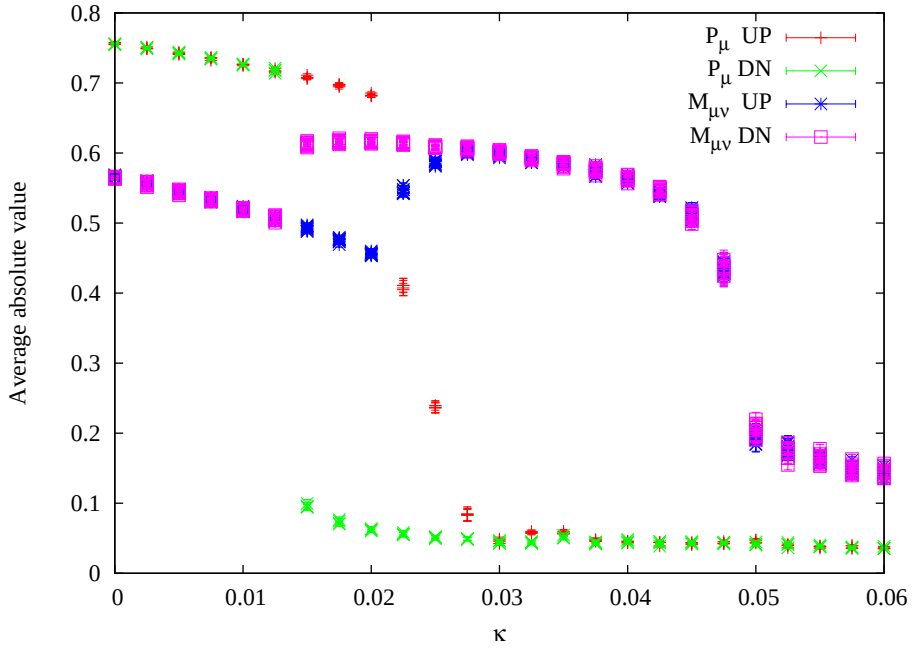

Figure 5.10: Absolute values of all Polyakov loops and corner variables in the low κ region, $N_f = 2$, $N = 30$, $b = 0.75$.

and with our resources we were only able to perform it at a single value of coupling, $b = 1.0$, albeit for both $N_f = 2$ and $N_f = 1$. In both cases we have done very fine scans near the edge of the funnel. $N \leq 53$ was used for $N_f = 2$ and $N \leq 60$ for $N_f = 1$. The corner variables were found to be the most useful in determining the transition (although we performed careful checks if the other observables do not show any signs of some more complicated pattern of the symmetry breaking that the corner variables could miss). We were able to pin down the transition, conservatively, to about $\delta\kappa = \pm 0.001$.

The results are presented in Fig. 5.11 along with two fits each. The first fits are of the form $c_0 + c_1/N$ – they have a very low χ^2/d.o.f. (signalling that the uncertainties are perhaps overly conservative) and they look very

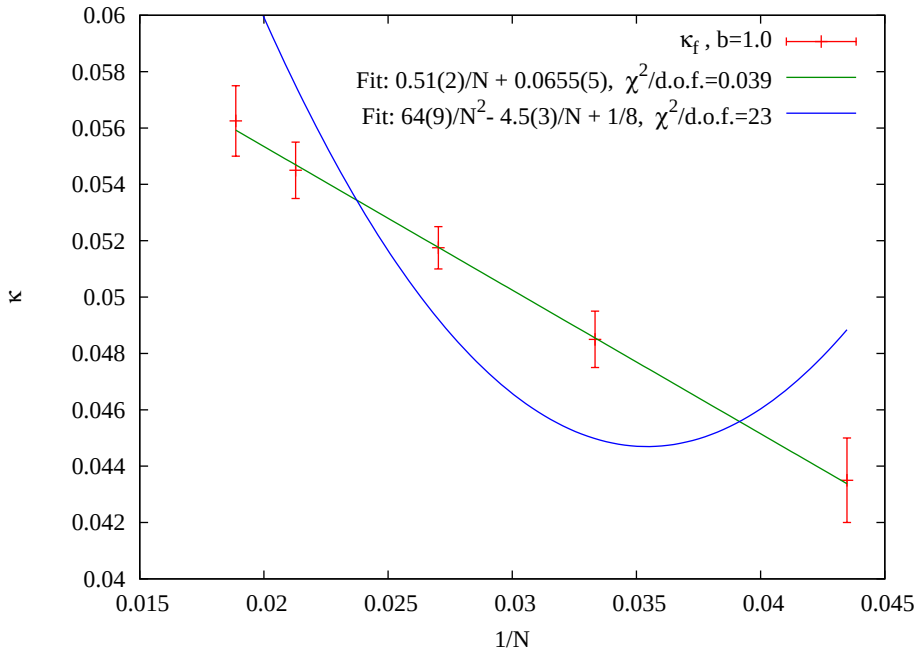

(a) $N_f = 2$

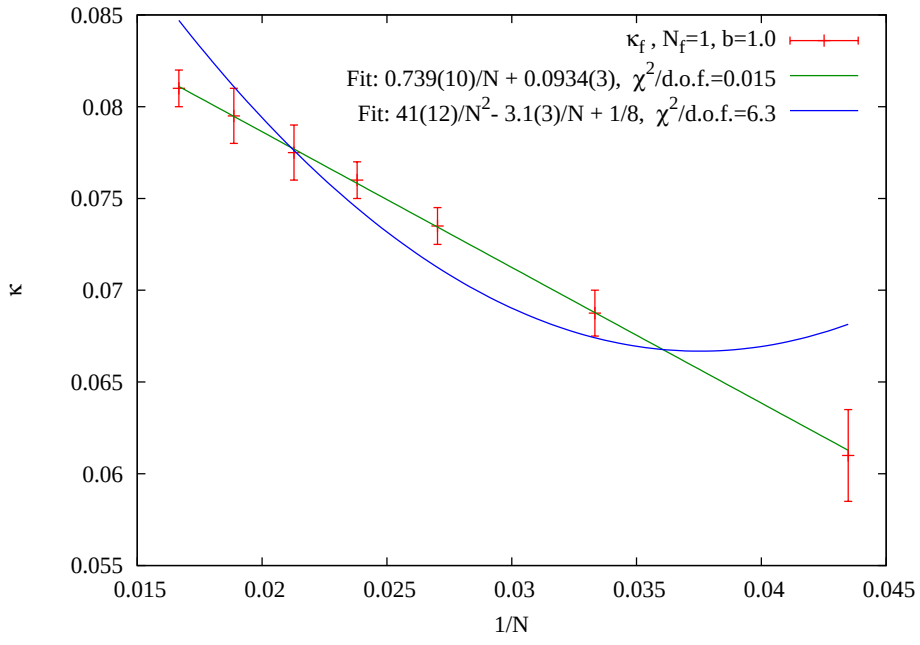

(b) $N_f = 1$

Figure 5.11: Large-N extrapolations of κ_f. Note that the errors are rather conservative as the main goal was the exclusion of the "closed funnel" hypothesis. The point $N = 60$ for $N_f = 1$ was calculated using the new parallel code on the `Deszno` supercomputer.

reasonable. The extrapolated large-N limits are:

$$\kappa_f(N_f = 2, N = \infty, b = 1) = 0.0655(5), \tag{5.6}$$

$$\kappa_f(N_f = 1, N = \infty, b = 1) = 0.0934(3), \tag{5.7}$$

both of which are values substantially lower than κ_c (which is $\approx 0.13 - 0.14$ at this value of b). Note that the funnel is significantly narrower for $N_f = 1$. This is understandable in the context of the perturbative calculations presented in Sec. 3.2.2 (cf. Eq. 3.19).

The second fits are to the function $c_1/N + c_2/N^2 + 1/8$ where the constant term is the lower limit on κ_c[5]. In both cases the fit is extremely poor (χ^2/d.o.f. $= 23$ for $N_f = 2$ and χ^2/d.o.f. $= 6.3$ for $N_f = 1$), excluding the possibility of the closed funnel – particularly taking into account that taking $\kappa_c = 0.13 - 0.14$ makes the fits even worse. We conclude that, at least for $b = 1$, the funnel has finite width in the large-N limit and the reduction holds also for rather heavy fermions.

5.3.3 Funnel width as a function of b

Another interesting property of the funnel is its behaviour as a function of b. Ref. [61] predicts that at large b the width of the funnel in am should be proportional to $b^{-1/4}$. As was already mentioned in the previous section, it also predicts that at the edge of the funnel there should be multiple phases with partially broken symmetry – the width of each eigenvalue clump is proportional to $b^{-1/4}$ so the maximum number of clumps should increase with b (as long as N is large enough).

To investigate this we have performed a series of scans in κ for $N = 10$ (and, in some cases, for $N = 30$) at b=2.5, 5, 10, 50 and 200 (the presented analysis uses $N_f = 2$ data only; we have no reasons to suspect a qualitatively different behaviour of $N_f = 1$ in this case). We find that the simulation algorithm performs surprisingly well even at such extremely high values of

[5]That is, without taking into account the additive renormalization of the mass. The precise determination of κ_c is very costly and we have limited ourselves to finding the approximate value. Therefore, we choose the most conservative approach in the fits.

b. No indication of autocorrelation times that are close to the number of trajectories used for measurements (7500 in the $N = 10$ case) was found[6].

We analyze κ_f as a function of b to check whether

$$am_f \equiv \frac{1}{2\kappa_f} - \frac{1}{2\kappa_c} \propto b^{-1/4}. \tag{5.8}$$

It would be of great benefit to repeat the study of the previous section for all values of b – that is however out of our numerical possibilities. Also, we find that it is harder to pin down the precise κ_f for b away from unity. At $b = 0.35$ the transition to the center-symmetric phase is very smooth, up to the point where locating it precisely is very hard and in fact it may be a crossover – one sign of such difficulties was already seen in Sec. 5.3.1 in the case $b = 0.35$, $\kappa = 0.06$. Also, Ref. [74] has triggered a discussion whether the funnel has at all finite width at this value of b. At $b = 0.5$ and above the transition becomes well-located and with growing b it becomes stronger and stronger. At very high b it becomes a strong-first order transition with significant hysteresis (see also the discussion of the plaquette in Sec. 6.1) that makes it difficult to precisely determine κ_f without using more advanced methods. The situation is thus not entirely explained away from $b = 1$ and would definitely benefit from further study.

Therefore, we limit ourselves to the analysis of the data for $N = 10$ and 30, presented in Fig. 5.12. Along with the data we present the fits to the form predicted by Ref. [61] with $\kappa_c = 0.125$ for all b, for simplicity. The fit at $N = 10$ is good while the fit at $N = 30$ has some tension to the obtained data (the data seems to be better reproduced if we insert the estimate for the true value of κ_c but that also significantly increases the uncertainties in am_f as the precision of our estimate of κ_c is rather limited). Overall, our conclusion is that the obtained results are consistent with the predicted dependence on b.

[6]However the MD step size has to be reduced, approximately as $\sqrt{b}$, and we find that for $b = 200$ the 450 trajectories used for thermalization is sometimes slightly too little for the system to thermalize completely.

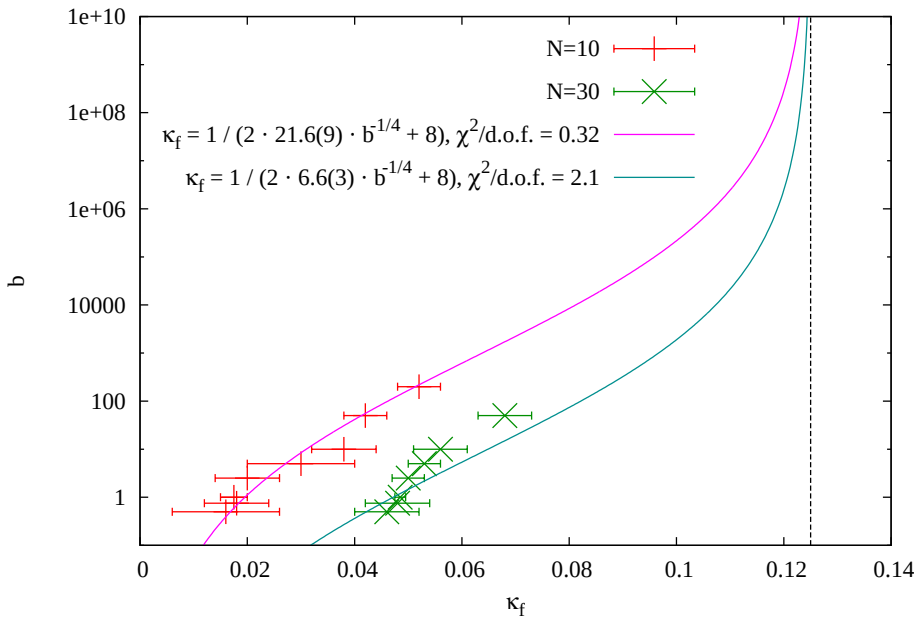

Figure 5.12: The dependence of κ_f on b, for $N = 10$ and 30, $N_f = 2$. The dashed vertical line marks $\kappa_c(b = \infty) = 1/8$. The fit functions are discussed in the text.

Chapter 6

Physical measurements in the AEK model

6.1 Plaquette

The basic quantity to analyze in any lattice gauge theory is the average value of the plaquette

$$U_{\text{plaq}} = \frac{1}{6N} \sum_{\mu<\nu} \operatorname{Tr} U_\mu U_\nu U_\mu^\dagger U_\nu^\dagger. \tag{6.1}$$

While the plaquette is a UV-dominated quantity, and thus does not relate directly to any continuum observable, it is very helpful to study the gross features of the theory and to compare different lattice calculations.

Fig. 6.1 presents the results of the plaquette in the horizontal scans at $b = 0.5$ and $b = 1.0$ (with the parameters described in Sec. 5.2). We also plot, where possible, the approximate large-N results obtained by fitting the results at the four values of N (or more, where available) to the function $c_0 + c_1/N + c_2/N^2$. The more precise fits done in selected points of the $\kappa - b$ plane are described further in this section.

In both plots there is a visible change of slope around $\kappa \approx 0.05$, when we enter the funnel. Also in the large-κ region we see a change of behaviour at the edge of the funnel. Another interesting feature of both plots is the behaviour in the vicinity of $\kappa_c \approx 0.13$ – there is a large jump in the

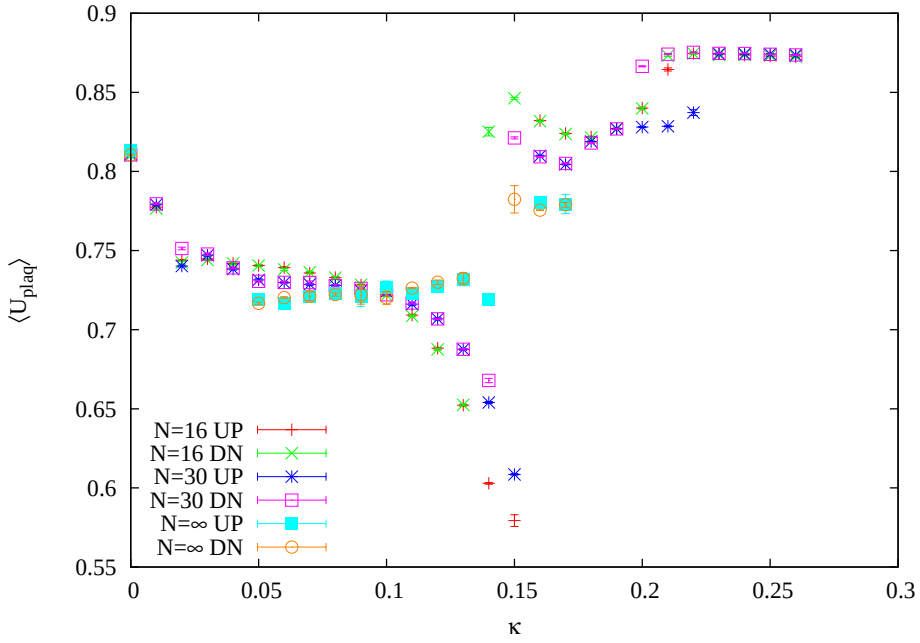

(a) $b = 0.5$

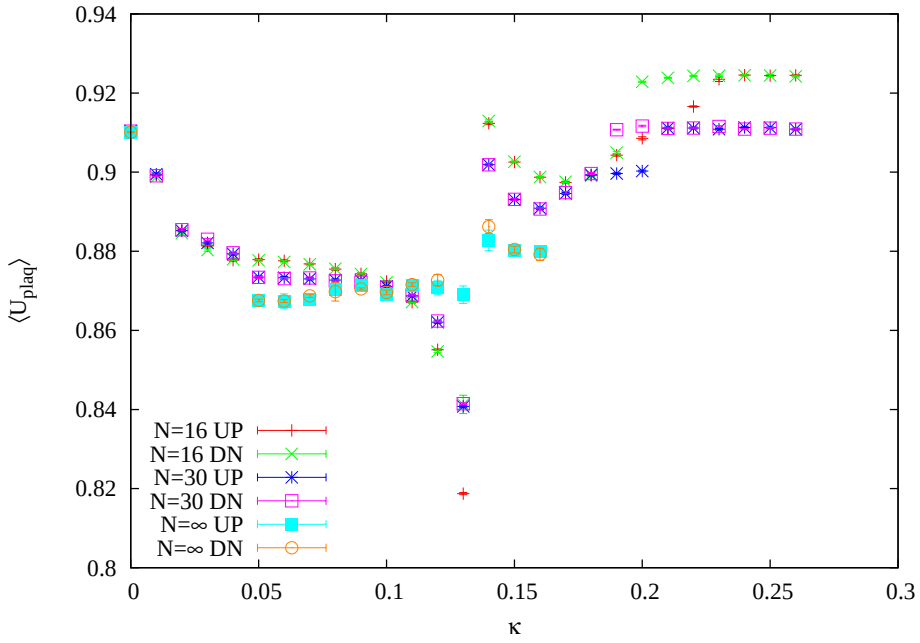

(b) $b = 1.0$

Figure 6.1: Horizontal scans (both UP and DOWN) of the average plaquette at $N_f = 2$ for $N = 16$, 30 and the large-N extrapolations (where possible), and two values of the 't Hooft coupling.

plaquette value. The jump becomes smaller with growing N, however it seems to persist at large N. While a more precise (and very expensive computationally) scan in the near-κ_c region could resolve this issue, this data suggests that the phase transition in κ_c is likely to be of first order.

At $N_f = 1$ we see the same picture, which was already reported in Ref. [45]. In the $N_f = 1$ case this is the expected behaviour because the large-volume theory is expected to be confining [49, 50]. For $N_f = 2$ the supposed first order transition in κ_c is however somewhat surprising as the large-volume theory is expected to be conformal (in the massless case).

The argument goes as follows: based on analysis in chiral perturbation theory one can argue that for a confining theory one expects (close to the continuum limit) a first order transition or two second order transitions separated by the Aoki phase [75, 76]. On the other hand if the theory is conformal one expects a single second order phase transition at κ_c – that is the case for $N = 2$ where the single second order phase transition is observed for $b \gtrsim 0.25$ [54, 55]. A different behaviour of the large-N theory is possible although unexpected (see Sec. 3.1).

Let us now discuss the large-N extrapolations of the average plaquette. Fig. 6.2 shows two example plots for different parameters. As already pictured in Fig. 6.1, the finite-N corrections are quite substantial and can have either sign, depending on the position in the $\kappa - b$ plane. We find that the leading finite-N correction is $\mathcal{O}(1/N)$. This is different from the large-volume results where one expects $\mathcal{O}(1/N^2)$. In the reduced model one can however observe this kind of behaviour – the one-loop analysis of the one-site pure-gauge model around the center-symmetric vacuum gives [19]:

$$\langle U_{\text{plaq}} \rangle = 1 - \frac{1}{8b}(1 - 1/N) + \mathcal{O}(1/b^2). \tag{6.2}$$

In fact, comparing Eq. 6.2 to the data in Fig. 6.2(b) we see that at $b = 1$ the large-N one-loop result, 0.875, is a reasonable approximation to the limit obtained from the data, even with moderately light fermions at $\kappa = 0.12$.

In general, inside the center-symmetric funnel but far away from κ_c (for the heavy fermions) we expect that the large-N extrapolation of the plaquette will be close to the large-volume pure-gauge result with a growing

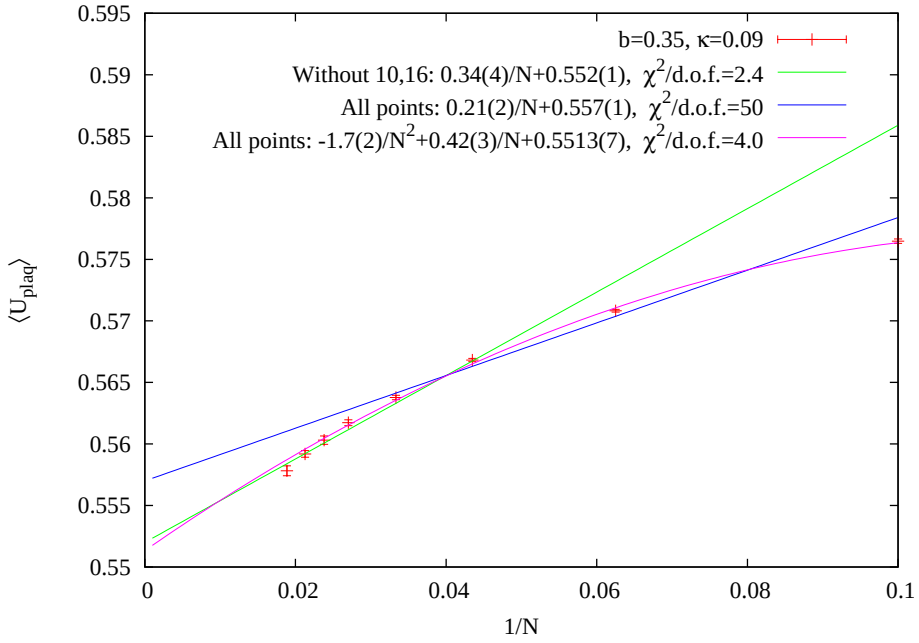

(a) $b = 0.35, \kappa = 0.09$

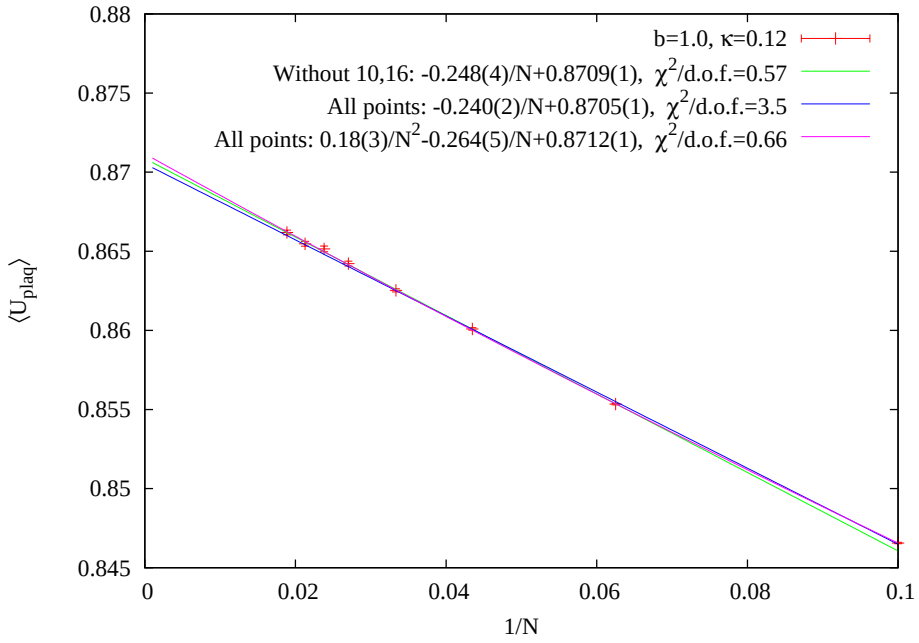

(b) $b = 1.0, \kappa = 0.12$

Figure 6.2: Two examples of large-N extrapolations of the plaquette for $N_f = 2$. Various fits are shown in addition to the data.

b	κ	χ^2/d.o.f.	c_1	c_0	pure-gauge value
0.35	0.06	1.8	0.75(4)	0.549(1)	0.550
0.35	0.09	2.4	0.34(4)	0.552(1)	0.550
0.35	0.12	1.5	-0.92(3)	0.565(1)	0.550
1.0	0.06	0.2	0.120(3)	0.8694(1)	0.8692
1.0	0.09	1.1	0.076(3)	0.8697(1)	0.8692
1.0	0.12	0.6	-0.248(4)	0.8709(1)	0.8692
1.0	0.15	2.3	0.39(1)	0.8795(4)	0.8692

Table 6.1: Results from large-N extrapolation of plaquette expectation values at $N_f = 2$. We choose the fit function $c_0 + c_1/N$ to results at $N = 23$, 30, 37, 42, 47 and 53 – we find that in all cases analyzed this choice leads to reasonable fit quality (the largest obtained χ^2/d.o.f is 2.4 which corresponds to p-value $p \approx 0.04$). The inclusion of $N = 10$ and 16 leads to worse fit quality and in some cases even the inclusion of $1/N^2$ term does not lead to acceptable fits (see e.g. Fig. 6.2(a)). The table quotes the values of c_0, c_1 and χ^2/d.o.f., with errors being statistical. Systematic errors (from different choices of fit function) are a few times larger than the statistical errors. Our best estimates of the pure-gauge large-volume expectation value are also quoted. The $b = 1$ value is a perturbative result obtained from Ref. [45], while that at $b = 0.35$ is obtained from the $N = 8$ pure-gauge simulation at $b = 0.3504$, from Ref. [77].

discrepancy from the pure-gauge behaviour as $\kappa \to \kappa_c$. To verify this hypothesis, in Table 6.1 we collect the results of the extrapolations together with the estimates of the pure-gauge large-volume results.

We see that the extracted large-N results, c_0, confirm our semi-quantitative prediction. For $\kappa = 0.06, 0.09$ the results are consistent with the pure-gauge results while for $\kappa = 0.12$ (closer to κ_c) they begin to differ. We also consider one point on the large-κ side of κ_c. In this case the plaquette differs substantially from the pure-gauge result. This shows that the difference of behaviour between the l.h.s. and r.h.s. of κ_c persists in the large-N limit (see also the large-κ regions in Fig. 6.1).

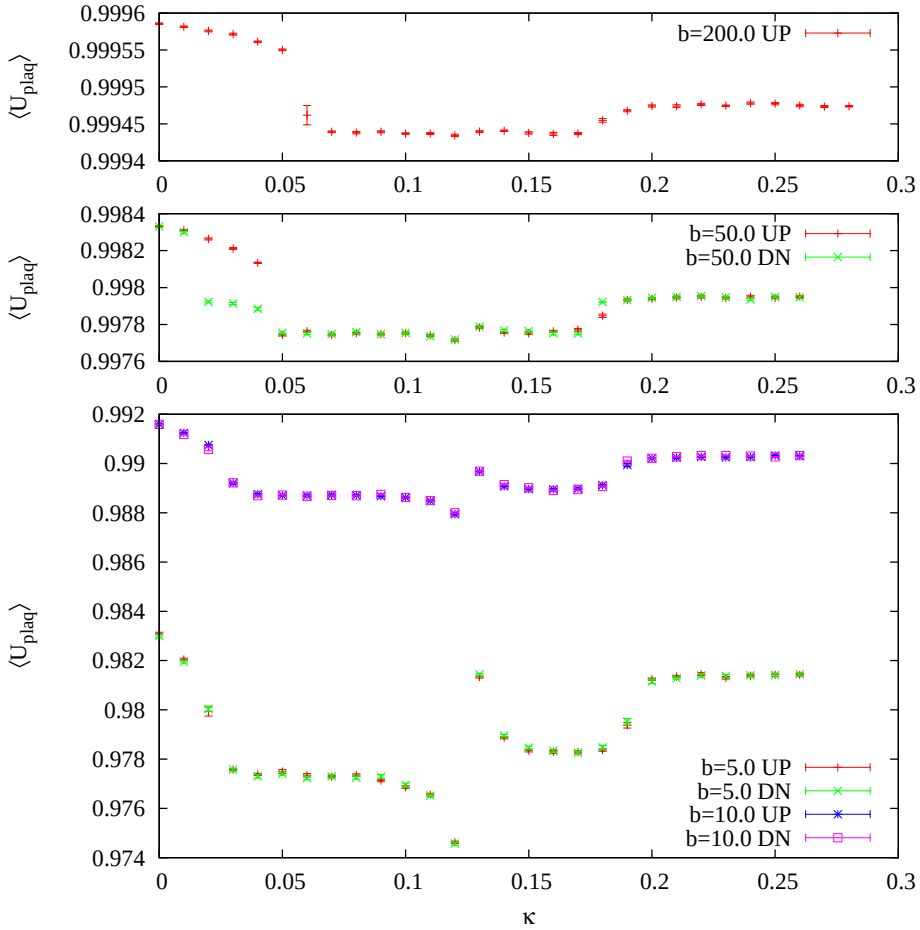

Figure 6.3: The average plaquette in scans at extremely high b for $N_f = 2$, $N = 10$. Note the very fine vertical scale at large b. At such high values of b we have $\kappa_c \approx 0.125$, while κ_f ranges approximately between 0.03 and 0.05, depending on the value of b (cf. Fig. 5.12).

We conclude this section with the results for very large b. The values of the plaquette in scans at $b = 5, 10, 50, 200$ (which were already discussed in Sec. 5.3.3) are presented in Fig. 6.3. The general shape of each curve resembles those at $b = 1$ (compare Fig. 6.1(b)). There are two distinctive features:

1. The jump at κ_c falls rapidly with increasing b – such behaviour is qualitatively consistent with the expectations of chiral perturbation

theory in the confining scenario [75].

2. The jump in the plaquette at κ_f becomes more distinct, signalling that the transition in κ_f is first order at very large b.

6.2 Wilson loops and static-quark potential

While the plaquette is a very useful quantity to compare lattice simulations to one another, ultimately one would like to be able to use the volume reduction to calculate physical (continuum) quantities. One such quantity that is accessible in the single-site model is the heavy-quark potential. We calculate it using rectangular Wilson loops wrapped around the 1^4-torus, in accordance with the volume reduction prescription:

$$W(L_1, L_2) = \frac{1}{12} \sum_{\mu \neq \nu} \left\langle \tfrac{1}{N} \mathrm{ReTr}\, U_\mu^{L_1} U_\nu^{L_2} U_\mu^{\dagger L_1} U_\nu^{\dagger L_2} \right\rangle , \tag{6.3}$$

where we have averaged over all orientations.

For $N \to \infty$, inside the funnel, the single-site result should be equal to the large-volume value, for all L_1, L_2. We can extract the potential from the large L_2 behaviour:

$$W(L_1, L_2) \xrightarrow{L_2 \to \infty} c(L_1) e^{-V(L_1) L_2}. \tag{6.4}$$

In the confining regime we expect linear behaviour of the potential at large L_1, with non-vanishing string tension σ:

$$\frac{dV(L_1)}{dL_1} \xrightarrow{L_1 \to \infty} \sigma. \tag{6.5}$$

As we are always dealing with finite N in the simulations, we need to keep $L \ll N$ to keep the finite-N effects under control – the key question is how large L_i one can achieve at given N. This is an exploratory study and we only used unsmeared links, as opposed to the state-of-art large-volume simulations which use various kinds of smearing as well as other noise reduction techniques. In this way we can identify the finite-N effects in a more transparent way.

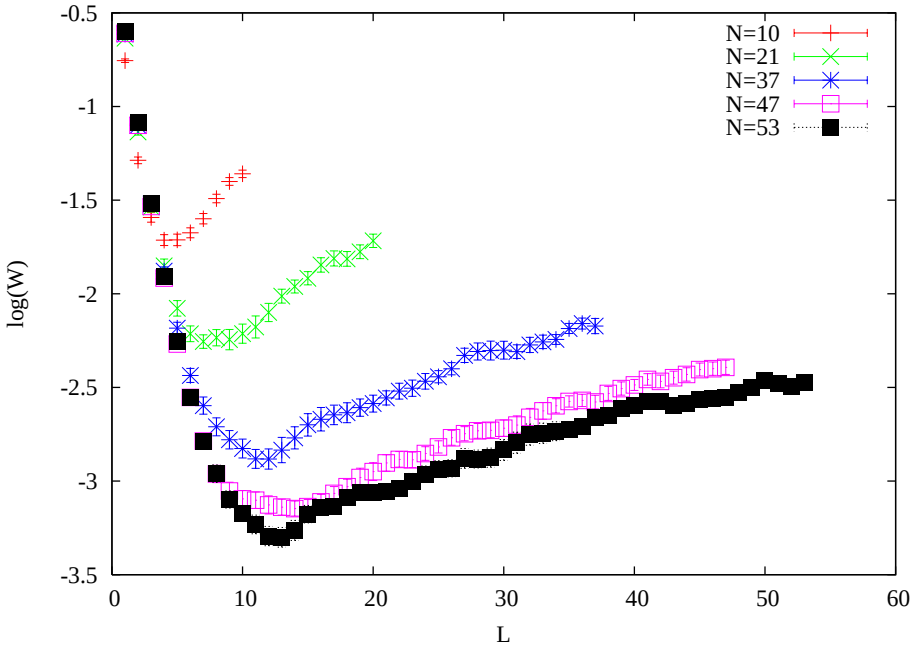

Figure 6.4: Log-linear plot of $1 \times L$ Wilson loop versus L for $L \leq N$. Results are from $N_f = 2$, $b = 0.35$, $\kappa = 0.12$ and for $N = 10$, 21, 37, 47 and 53, using 20 configurations except for $N = 10$ where 150 configurations were used.

In Fig. 6.4 we present the log-linear plot of $1 \times L$ Wilson loops for several values of N. For each N we find an approximately exponential decrease followed by a slow, approximately linear, rise. Since the rise is an unphysical behaviour (in the large-volume language) and it begins at larger L as N increases we interpret it as a finite-N effect. The exponential drop-off seems to converge to a common envelope (linear on the logarithmic plot). For example, at $L = 6$ the $N = 37$ point has already peeled off from the envelope while the $N = 47$ and 53 are in good agreement. We can thus reliably extract the large-N behaviour up to some $L_{max}(N)$ – the crucial question is how exactly L_{max} depends on N. To estimate this for every N one can look at the minimum value of the loop for given L. Then we find that it falls approximately as $1/N$ thus L_{max} grows only logarithmically with N.

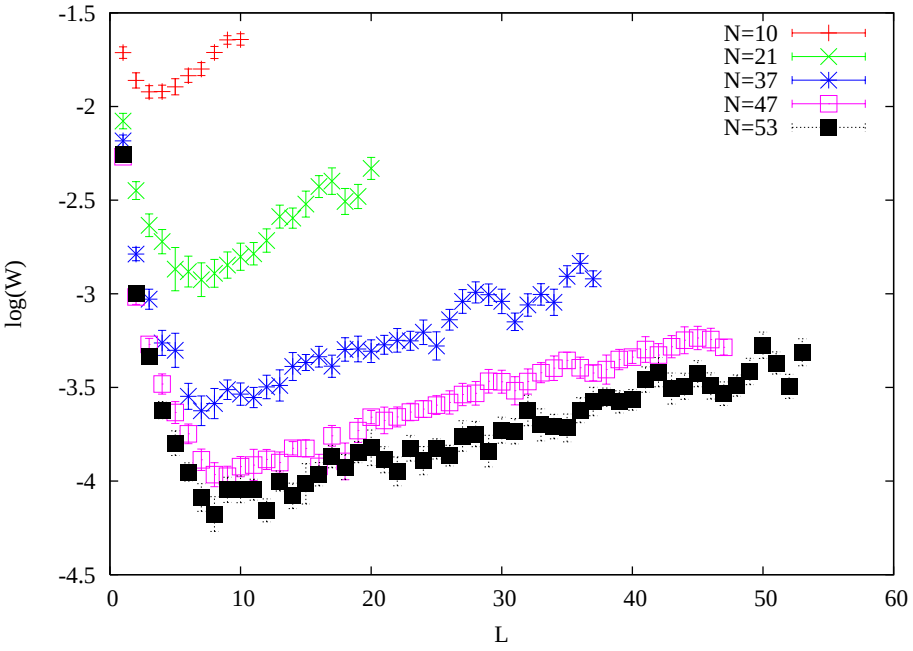

Figure 6.5: As for Fig. 6.4, but for $5 \times L$ loops.

This is not unexpected as we are trying to extract an exponentially falling contribution from a quantity that has finite-N corrections, however this poses a significant numerical challenge. It is also worth stressing that it is not the statistical errors that are limiting but the size of N that needs to be taken to extract the potential for large enough L.

Having said that, we see from the Fig. 6.4 that we can extract the value of the potential $V(1)$ with reasonably small errors. To find σ we also need to extract the potential at larger separations. In Fig. 6.5 we show the results for $5 \times L$ loops. The overall pattern is similar to the one in Fig. 6.4 but the convergence to the common exponentially-decaying envelope is much poorer and only results for $L \leq 2$ appear converged. This is by no means unexpected as the signal for $W(5, L)$ is significantly smaller than for $W(1, L)$ while the finite-N background is little changed. This type of behaviour only allows us to calculate the potential up to separations of 2-3 lattice units which is too small to reliably estimate the string tension. We were also unable to extract the Creutz ratios in a reliable way. Again, note

that the problem is not in the statistics (the 20 configurations are sufficient to measure the exponentially-falling part of the curves) but rather in the $1/N$ corrections.

We have also carried out similar calculations in the other points inside the funnel. Our results are qualitatively the same although we find that the slope of the rising part at large values of L generally decreases with growing b. Also, in the large-κ part of the funnel (where the plaquette is closer to unity) the slope decreases even further and becomes almost L-independent.

The unphysical rise at large L can be understood, at least qualitatively, in the strong coupling limit of the pure gauge theory (i.e. at $\kappa = 0, b = 0$). The links are then distributed according to the Haar measure. In the large volume this results in a zero signal due to the vanishing integrals of type:

$$\int U dU = 0. \tag{6.6}$$

On the single site, however, the zero-th order of the strong coupling expansion does not vanish because for every closed contour every U_μ in the integral comes in pair with a corresponding $U_\mu^\dagger$. In fact, one can show (using Refs. [78, 79]) that for $b = 0, \kappa = 0$:

$$W(L_1, L_2) = \frac{1}{N^2 - 1}(L_1 + L_2 - 1 - L_1 L_2/N^2) \quad \text{for} \quad 0 < L_1, L_2 \leq N. \tag{6.7}$$

This result shows that the linear rise of the signal with L is not unnatural in volume-reduced models at finite N. On the quantitative level, however, the above model does not fit the data obtained in the simulations in the moderate and weak coupling region. For example, one would expect that $W_{min} \sim 1/N^2$ while we observe an approximate $1/N$ dependence.

One idea on how to make the corrections smaller is to use the 2^4 lattice and only measure the Wilson loops with odd L_1 and L_2. In this way the loop never contains pairs U, $U^\dagger$ of the same link and the zero-th order in the strong coupling expansion vanishes. That this in fact reduces the finite-N corrections is pictured in Fig. 6.6. This further confirms that the finite-N behaviour can be understood, at least on the qualitative level. However, our values of N to date ($N \geq 15$) are too small to allow a reliable extraction of the string tension from the 2^4 data.

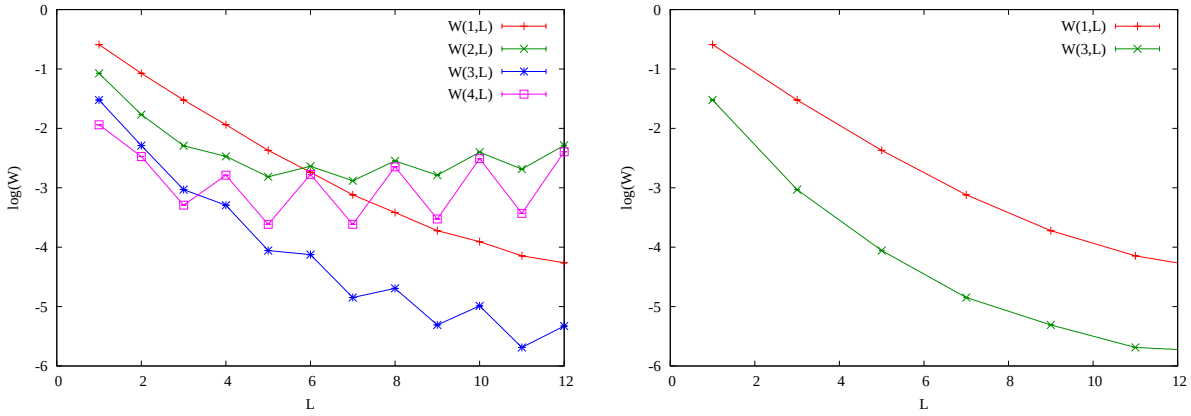

(a) All Wilson loops

(b) Only odd-sized Wilson loops

Figure 6.6: Wilson loops on 2^4 lattice. $N_f = 2$, $N = 10$, $b = 0.35$, $\kappa = 0.1$. The lines between the datapoints are added to guide the eye.

6.3 Spectrum of the Dirac operator

6.3.1 Spectrum of the Wilson Dirac operator D_W

As discussed in Sec. 2.2.4, one can analyze the effective size of the volume-reduced system at finite-N. One of the observables that are useful to analyze this quantity is the spectrum of the Dirac operator. The orbifold construction predicts the effective length L_{eff} to scale proportionally to $N^{1/4}$ (cf. Eq. 2.17 and the preceding discussion).

However, as we show further in this section, some features of the Dirac operator spectrum suggest that such scaling may be perhaps overly pessimistic thus we also compare our data to a less conservative possibility, discussed in Refs. [80, 81] in the context of theories with twisted boundary conditions – in this case every element of the the volume-reduced link matrices is used in the packaging of the link matrices of the large-volume theory. This leads to $L_{\text{eff}} \propto N^{1/2}$. There is also an even more optimistic scenario, motivated in the Appendix of Ref. [2], which leads to $L_{\text{eff}} \propto N$.

We expect that in the center-symmetric funnel the spectrum of the Wilson Dirac operator D_W (cf. Eq. 3.3) should resemble that of the large-

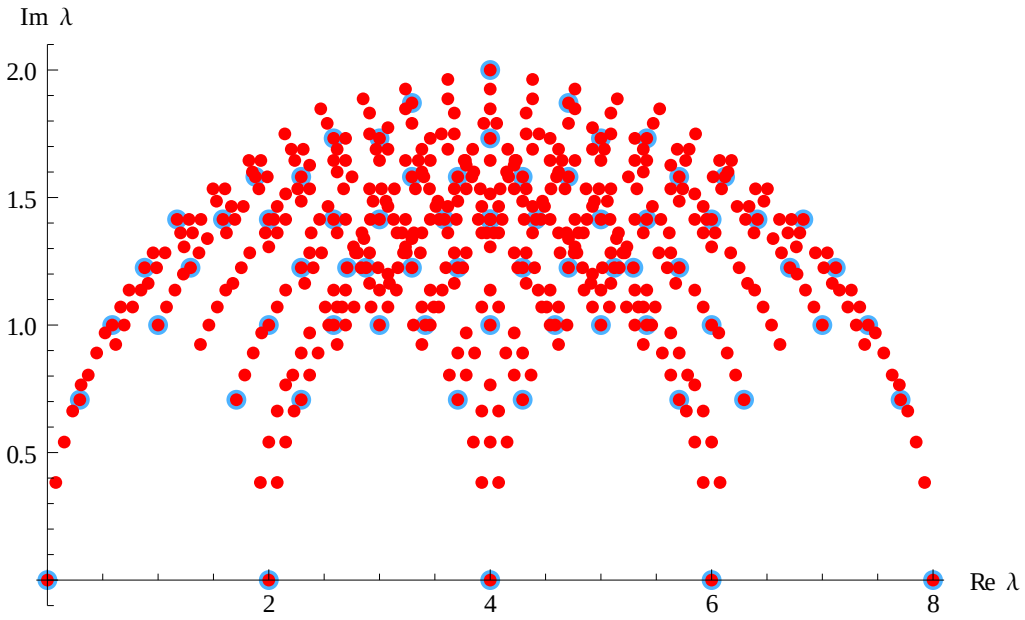

Figure 6.7: Free spectrum of the Wilson Dirac operator at 8^4 (large blue dots) and 16^4 (small red dots), $m_0 = 0$. The spectrum is symmetric with respect to the real axis, only the non-negative imaginary part is shown.

volume four-dimensional lattice gauge theory on L_{eff}^4. In particular, in the weak coupling, $b \gtrsim 1$, where the spectrum of a free fermion is a valid approximation, the spectrum should have the characteristic five "fingers" that reach down to the real axis [82]. The number of fingers is a direct indicator of the dimensionality of the system (in d dimensions there are $d+1$ fingers). Thus observing a smaller number of fingers is an indicator of the correlations between the lattice directions (supplementing the discussion in Sec. 5.2). Also, the distance of the fingers to the real axis should scale like $1/L_{\text{eff}}$. As an example, the spectrum of the free Wilson Dirac operator on lattices 8^4 and 16^4 is presented in Fig. 6.7.

We now show some representative results for the spectrum of $D_W(m_0^{(\text{valence})} = 0)$ from our simulations. Note that the Dirac operator in the determinant of Eq. 3.1 (which determines the masses of the sea quarks)

is

$$D_W(m_0) = 2\kappa\big(4D_W(0) + \tfrac{1}{2\kappa} - 4\big) = \frac{1}{4 + am_0}\big(4D_W(0) + am_0\big), \qquad (6.8)$$

so that the eigenvalues of $4D_W(0)$ close to $\lambda = 4 - \frac{1}{2\kappa}$ are suppressed. The spectrum is bounded to $0 \leq \mathrm{Re}\lambda \leq 8$ so the determinant suppression is important only for $\kappa > 1/8$.

Another thing to remember is that on a lattice with even number of sites in each direction the Dirac operator spectrum is symmetric under reflection about the $\mathrm{Re}\lambda = 4$ axis [83]. On the single site there is no such symmetry but if the reduction holds we expect its emergence (approximate at finite-N).

In Fig. 6.8 we show the spectrum for six representative values of κ in the scan at $N_f = 2$, $N = 30$, $b = 1$. At $\kappa = 0.01$, Fig. 6.8(a), which is in the $\mathbb{Z}_1$ phase (compare Figs. 5.1 and 5.4(a)) we see a well-formed first finger and a small indication of the second one. This is consistent with the link eigenvalues forming a single clump, so that the "momenta", given by eigenvalue differences are small (the Dirac operator is constructed out of the adjoint links and thus it gives the information about the differences of eigenvalues of the fundamental links). At $\kappa = 0.03$, Fig. 6.8(b), we are in the $\mathbb{Z}_2$ phase. The two clumps of link eigenvalues allow the eigenvalue differences to reach π and to form the fifth finger, however the second and fourth finger are only slightly indicated and the middle finger is absent. Also the "rectangular" shaped envelope shows that the spectrum is very different from the large-volume one.

The next value, $\kappa = 0.12$ pictured in Fig. 6.8(c), is well inside the center-symmetric funnel. The distribution of the eigenvalues of D_W is qualitatively very similar to that of a free fermion on a large lattice with a rounded top and five fingers – these features are present for all $\kappa < \kappa_c$ inside the funnel. A particularly interesting feature is the presence of the comet-shaped clump of eigenvalues near the origin. We find that there are exactly $4(N-1)$ eigenvalues per configuration in this clump. We thus interpret them as the would-be zero modes i.e. the eigenvalues that would be zero in the $b \to \infty$ limit. In the weak-coupling analyses these modes are neglected

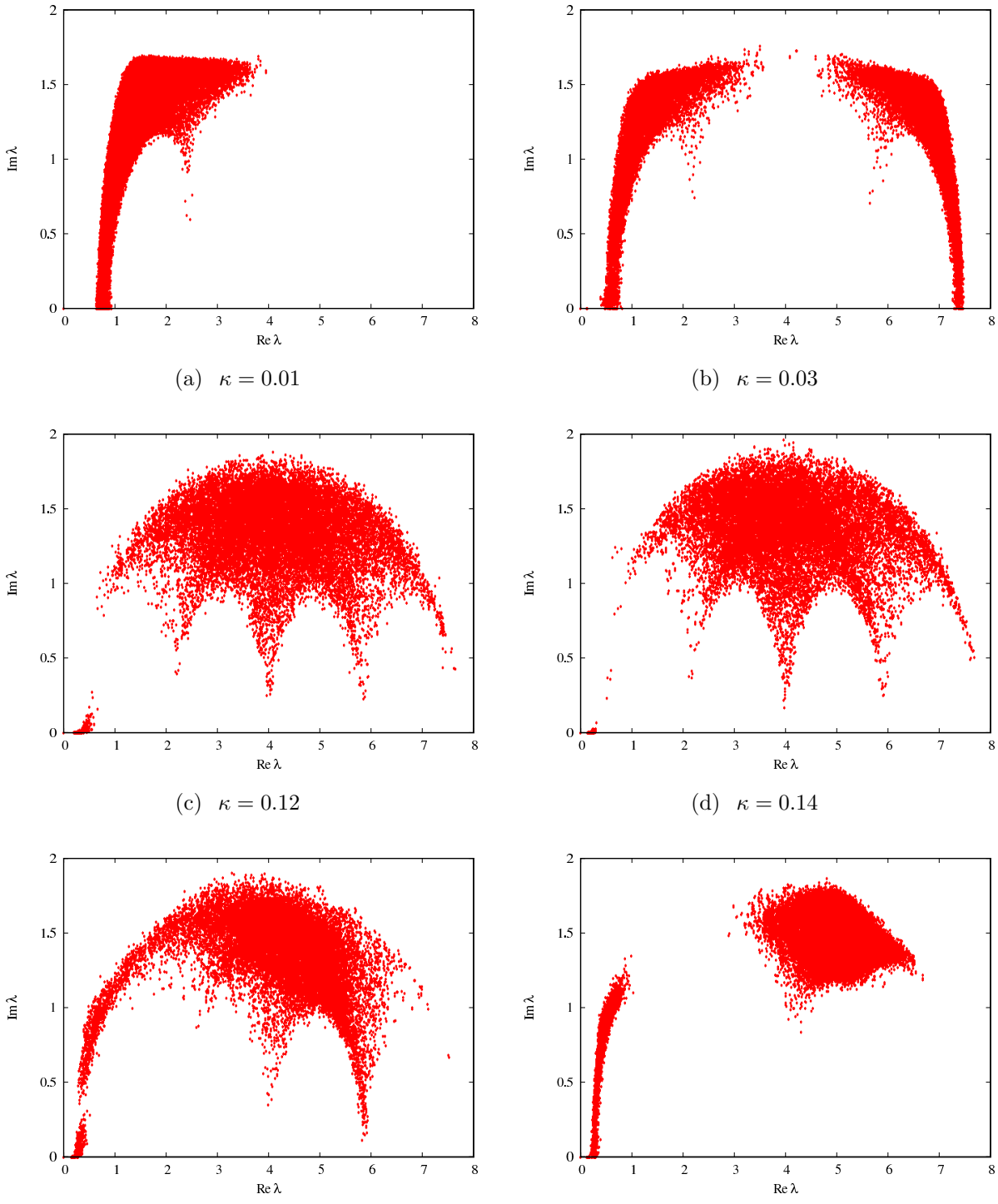

(a) $\kappa = 0.01$ (b) $\kappa = 0.03$

(c) $\kappa = 0.12$ (d) $\kappa = 0.14$

(e) $\kappa = 0.17$ (f) $\kappa = 0.24$

Figure 6.8: Spectrum of $4D_W(0)$ from simulations at $N_f = 2$, $N = 30$, $b = 1.0$ and six representative values of κ (i.e. masses of the sea quarks). The plots are made using 20 configurations each, only the eigenvalues with non-negative imaginary part are shown.

[60] because they do not impact the dynamics (i.e. they do not depend on ϑ_μ^a) and because they only form a $\mathcal{O}(1/N)$ fraction of the total number of modes.

In our calculations, however, they form the lowest non-zero eigenvalues of the Dirac operator and thus can have a significant impact on the finite-N dynamics, despite their relative paucity. Recall that the smallest eigenvalues of the large-volume Dirac operator determine the long-range behaviour of the theory, such as chiral symmetry breaking. For very large values of N we expect the smallest eigenvalues to come dominantly from the first finger, which should approach close to the real axis – we see that $N = 30$ is rather far from this description and we conclude that the would-be zero modes are a potential source of $\mathcal{O}(1/N)$ corrections whose contribution can be sizeable (given how far the "true" low-energy modes in the first finger are from the real axis).

For $\kappa = 0.14$, which is inside the funnel and above κ_c, the spectrum, shown in Fig. 6.8(d), is very similar to the one at $\kappa = 0.12$. The would-be zero modes look somewhat different – almost all of them are squeezed to the left of $\mathrm{Re}\lambda = 0.43$ which is the point suppressed by the determinant. As a whole though, the picture looks similar on both sides of the funnel. Moving on further to $\kappa = 0.17$, Fig. 6.8(e), which is also expected to be inside the funnel, we see that the second and fifth finger have almost disappeared while the first finger has become more distinct and reaches down closer to the real axis. This may raise some concerns whether this point is in fact in the funnel where volume reduction holds (an analysis of the width of the r.h.s. of the funnel, similar to the one in Sec. 5.3.2, would help to clarify this issue).

The last plot, Fig. 6.8(f), is taken at $\kappa = 0.24$, in the $\mathbb{Z}_3$ phase. This is reflected by the spectrum being divided into three distinct regions (the one with the negative imaginary part is not shown in the plot) resulting from link eigenvalue differences distributed around 0 and $\pm 2\pi/3$.

We have also studied the N-dependence of the spectrum at $b = 1$ and $\kappa = 0.12$. Fig. 6.9 compares the results for $N = 37$ and $N = 53$. The number of eigenvalues is approximately the same in both panels (and a

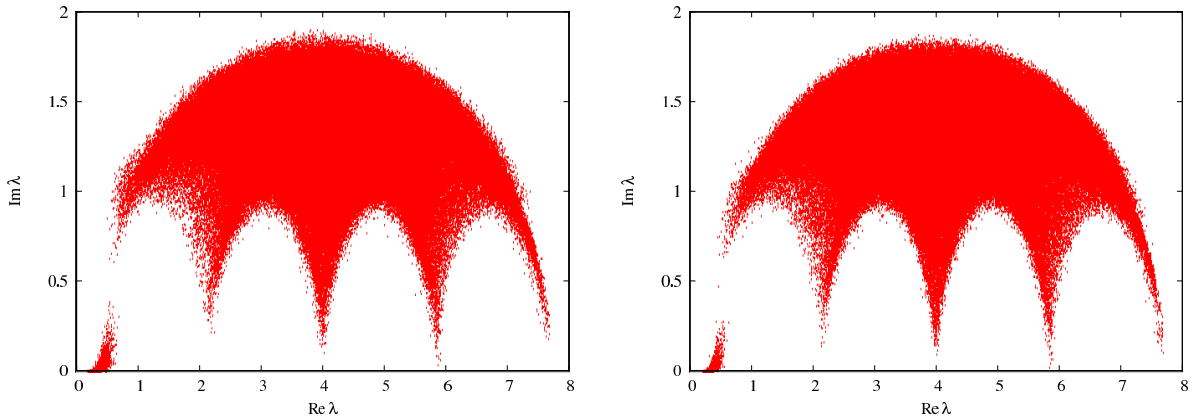

(a) $N = 37$, 300 configs (b) $N = 53$, 150 configs

Figure 6.9: Spectrum of $4D_W(0)$ at $N_f = 2$, $b = 1.0$ and $\kappa = 0.12$, for $N = 37$ and 53. Note that since $(53/37)^2 \approx 2$ the number of points is approximately the same in both plots.

lot bigger than in Fig. 6.8). There is not much difference in the spectra – the clump of the would-be zero modes decreases with growing N and the first and fifth finger move a little downwards. The tips of the other fingers, however, barely move.

The conclusions from these results can be summarized as follows:

1. There is a qualitative agreement of the spectrum of D_W inside the funnel with that of a theory on a four-dimensional large-volume lattice that supports our claim that the reduction holds therein.

2. The dependence of the distance of the fingertips to the real axis is inconsistent with $L_{\text{eff}} \propto N$. On our level of precision it allows both $N^{1/2}$ and $N^{1/4}$ although the presence of well-formed fingers disfavors the latter possibility. At $N \leq 53$ we would not expect the presence of the fingers in that case, unless some effects that we have not taken into account make the spectrum look "surprisingly" good[1].

[1]The $N = 48$ would correspond to $L_{\text{eff}} = 2$ at $N_{\text{eff}} = 3$ which shows no signs of fingers.

3. The would-be zero modes are a potential source of $\mathcal{O}(1/N)$ corrections and can significantly influence the finite-N dynamics, provided that these $1/N$ corrections are not exactly cancelled by some mechanism among the $4(N^2 - N)$ "bulk" eigenvalues.

We have also calculated the spectrum of the Dirac operator in the fundamental representation. This gives the information about the link eigenvalues themselves, rather than their differences. The obtained results confirm the results presented above and are not presented for the sake of brevity.

6.3.2 Spectrum of the hermitian Dirac operator

The scans similar to the ones in the previous section were also done for b lower than 1. In that case however, the picture is harder to compare with the known-results of the large-volume free fermion case. In particular, at $b = 0.35$ the spectrum fills the whole allowed region and there is no sign of fingers. A better approach in this case is to analyze the spectrum of the hermitian Dirac operator Q (cf. Eq. 4.13) or, equivalently, $Q^2 = D_W(m_0)D_W(m_0)^\dagger$.

Analyzing the eigenvalues of Q^2 can teach us many interesting things about the theory. In the continuum limit the spectrum has a gap

$$\lambda_{Q^2}^{\min} = (am_{\text{phys}})^2, \tag{6.9}$$

where m_{phys} is the physical quark mass. Away from the continuum the gap is smoothed but the spectrum still begins approximately at the square of the physical mass [84]. Also, if the theory shows the spontaneous breaking of the chiral symmetry, for small enough quark masses the density of the spectrum above the gap is approximately constant and equal to the condensate.

In Fig. 6.10 we present the results for the density of eigenvalues of Q^2 for $N_f = 2$, $b = 0.35$ and $\kappa = 0.12$ for several values of $N \leq 47$ (the results for $N = 53$ are very similar to those of $N = 47$ and were dropped due to lower statistics). The plots are normalized to have the same integral so that we can study the $N \to \infty$ limit. The peak at small eigenvalues around 0.01

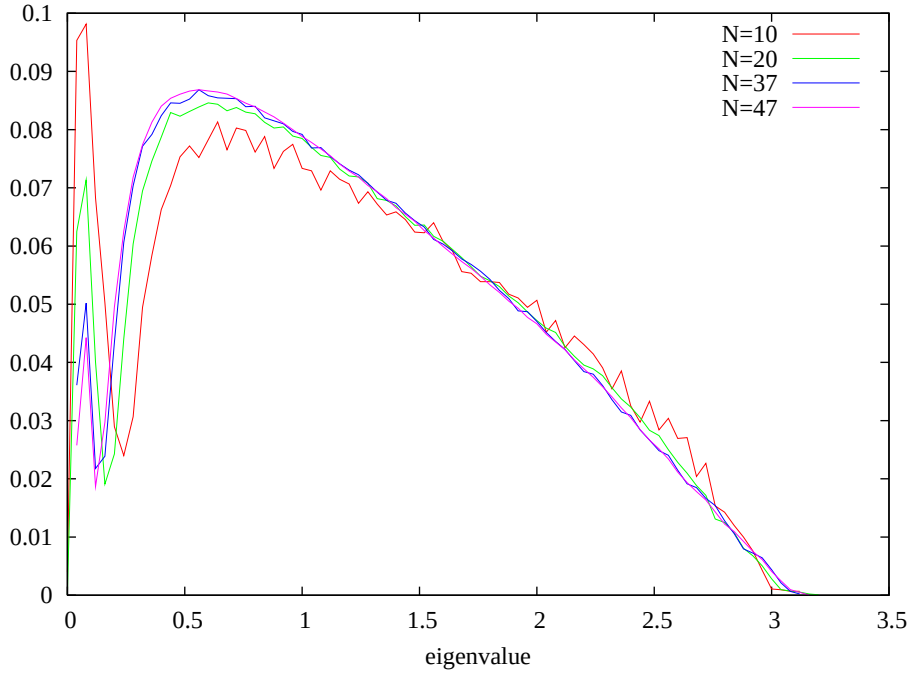

Figure 6.10: Density of eigenvalues of Q^2 for $N_f = 2$ at $b = 0.35$ and $\kappa = 0.12$, for $N = 10$, 20, 37 and 47, using 150, 150, 20 and 60 configurations, respectively. The vertical scale is arbitrary, but the relative scales for different N are chosen so that the area under each spectrum is the same. Errors are not shown, but can be estimated from the kinks in the spectra.

has exactly the area to contain the $4(N-1)$ would-be zero modes. Its area drops as $1/N$ and we expect it to disappear completely in the large-N limit.

The N-dependence of the bulk part of the spectrum seems to be divided into two parts – for the eigenvalues above $\lambda_{Q^2} \approx 1.5$ the density is approximately N-independent while the density of the smaller eigenvalues has substantial N-dependence for smaller values of N. The values for $N = 37$ and $N = 47$ (and unplotted $N = 53$) seem to be pretty consistent and there is not much area of the would-be zero modes to be "redistributed" to the bulk part. Thus we conclude that the form of the bulk density at $N = 47$ should be a good approximation to the large-N density.

These results give us another estimate of how large N should one use

in simulations to obtain the results that are close enough to the large-N limit. On one hand the bulk part of the spectrum is little changed beyond $N \approx 40$. On the other hands the $\mathcal{O}(1/N)$ contribution of the would-be zero modes is dominant in the physically-important low mode region (and will most likely remain so also for much larger values of N). It is not easy to determine a priori how important are the corrections due to the would-be zero modes – one needs to calculate physical observables, such as meson masses, and study their N-dependence.

We can now also give a very crude estimate of the physical mass by neglecting the would-be zero modes and linearly extrapolating the shape of the bulk density towards zero density. This analysis suggests that the gap is $\lambda_{Q^2}^{\min} \approx 0.1$ which corresponds to the quark mass $am_{\text{phys}} \approx 0.3$ modulo an unknown multiplicative renormalization factor (which we however expect to be $\mathcal{O}(1)$ at $b = 0.35$ [45]). This rough estimate shows that the quarks are relatively heavy at the given parameters, not much below $m_{\text{phys}} = 1/a$.

Chapter 7

Summary and outlook

In this work we have presented the analysis of large-N volume-reduced gauge theories using the lattice regularization. The volume reduction allows one to non-perturbatively analyze theories that are of great importance. With heavy fermions (both for $N_f = 1$ and $N_f = 2$) one can compare the results to the large-volume pure gauge theory in the large-N limit. On the other hand, with light fermions one can analyze a theory ($N_f = 1$ AEK) that is within $1/N$ of the physical QCD with two light quarks or a theory that is close to the conformal window and is very important for the walking technicolor models ($N_f = 2$ AEK)[1].

We have reviewed the concept of volume reduction showing how it arises from the comparison of large-N Dyson-Schwinger equations on the infinitely large and single-site lattice [1]. We have discussed the lack of spontaneous breaking of the center symmetry in the volume-reduced model as the key condition for the volume reduction to hold – and how it fails in the pure-gauge model originally discussed by Eguchi and Kawai in Ref. [1]. We have reviewed the ideas to cure the model and we have focused on the concept of adding fermions in the adjoint representation of the gauge group. We have then presented a pedagogical review of the large-N orbifold equivalences that constitute a modern theoretical background for the volume reduction

[1]Also the supersymmetric $N_f = 1/2$ case, that was not analyzed in this work, is a theory of great interest for the theorists.

with adjoint fermions.

Next, we have introduced the volume-reduced system to be analyzed in this paper – the single-site $SU(N)$ lattice gauge theory with N_f adjoint Wilson Dirac fermions – called the Adjoint Eguchi-Kawai model. We have discussed the theoretical importance of this model for comparisons with standard large-volume calculations and predictions. We have presented the perturbative predictions of the behaviour of the model as well as the semi-quantitative arguments going beyond the perturbation theory presented in Ref. [61]. The perturbative analysis predicts that the center symmetry in the large-N limit is intact only for the massless fermions. On the other hand, Ref. [61] argues that in the massive case the perturbative attraction of eigenvalues of the Polyakov loop may be overwhelmed by the non-perturbative fluctuations and result in a center-symmetric ground state, perhaps even with heavy fermions of $m \sim 1/a$. In such case we expect that the observables will be influenced mostly by the gluon dynamics and that one can compare AEK with heavy fermions directly to the pure-gauge large-volume large-N results. That would be a prescription to obtain a working Eguchi-Kawai reduction.

After introducing the subject we went on to the numerical analysis of the AEK model with the Monte Carlo method. We have presented the numerical setup used in this work – the Hybrid Monte Carlo algorithm for the $N_f = 2$ case as well as the Rational Hybrid Monte Carlo for the $N_f = 1$ case. We have discussed the N-scaling and the performance of the algorithm.

After that we have analyzed the phase diagram of the AEK model. To establish the realization of the center symmetry we performed, using $N \leq 60$ and a robust set of observables, scans in the $\kappa - b$ plane going to b as high as 200. We have shown that the model has a rich phase structure that is in agreement with the predictions of Ref. [61]. The center symmetry is fully broken for very heavy fermions – as one decreases the fermion mass the theory undergoes a series of phase transitions with partial breakings of the center symmetry. Finally, at small enough mass it enters the "funnel" of the unbroken center symmetry. The funnel exists on both sides of the κ_c

(the critical value of κ where the physical quark mass disappears). However, the pattern of the partial breakings is different on the two sides of κ_c. On the l.h.s. (this is the region typically used in the large-volume analyses) we see partial breakings up to $\mathbb{Z}_3$ phase while on the r.h.s. – up to $\mathbb{Z}_5$. We believe that at larger values of N it is possible to obtain groups with even higher partial breakings. Also, in accordance with Ref. [61] it is possible to see higher partial breakings when one goes to larger b – e.g. for $N = 30$ we see at most $\mathbb{Z}_2$ at $b = 1$ while for $b \geq 10$ we observe also a $\mathbb{Z}_3$ phase. We have also found that whenever the center symmetry is broken one observes strong correlations between different lattice directions.

We have found that $N_f = 1$ and $N_f = 2$ cases have a similar behaviour and thus we have mostly focused on presenting results for the $N_f = 2$ case (described in Ref. [2]). The main difference is the width of the funnel – the funnel is expected to be narrower in the $N_f = 1$ case (i.e. going to lower fermion mass is necessary to obtain the center-symmetric phase). We have found that this is in fact observed in the simulations.

We have also observed that for both numbers of flavours the funnel becomes narrower as N grows. It is thus a matter of crucial importance to establish whether it remains finite in the large-N limit. This is a significant numerical challenge and we have limited ourselves to prove it for a single value of coupling, $b = 1$, on the l.h.s. of κ_c. We have found that both for $N_f = 2$ and $N_f = 1$ the large-N extrapolation of quark mass m_f (the largest mass sufficient to restore the center symmetry) is rather large ($m_f \sim 1/a$), allowing to treat the dynamics at the verge of the funnel as essentially pure-gauge. Also, in both cases the fits to the closed-funnel hypothesis ($m_f = 0$) have very large values of χ^2/d.o.f. (23 for $N_f = 2$ and 6.3 for $N_f = 1$). This allows us to conclude that (at $b = 1$) the funnel does not vanish in the large-N limit and that massive fermions stabilize the center symmetry. We have also found that m_f has a b-dependence that is consistent with the predictions of Ref. [61].

Finally, we have used the volume reduction in order to analyze physical observables. First we have analyzed the average plaquette. We have performed the large-N extrapolations in selected points of the $\kappa - b$ plane

and shown that for heavy quarks the large-N value is consistent with large-volume pure-gauge calculations while for light quarks it begins to differ. We have also presented data suggesting that for both $N_f = 1$ and $N_f = 2$ there is a first order transition at κ_c for $b \lesssim 1$. While this result is expected for $N_f = 1$, it is rather surprising for $N_f = 2$ because it supports the confining scenario in contrast to large-volume calculations at $N = 2$ which show that the theory is conformal. A discrepancy of behaviour between $N = 2$ and $N \to \infty$ is unexpected in the literature and the situation would definitely benefit from further study focusing particularly on the light quark region.

We have also analyzed the heavy-quark potential using large Wilson loops. We found that the accuracy that one can obtain is limited by the finite-N effects – using $N \leq 53$ we were only able to obtain $V(L)$ for $L \lesssim 3$ and so we were unable to reliably extract the string tension. We have provided a qualitative description of the $1/N$ corrections using the strong coupling expansion and proposed a way to reduce them significantly using odd-sized loops on a lattice of size 2^4.

The last analyzed observable was the spectrum of the Wilson Dirac operator. By using the spectrum of D_W we have investigated the measure of "effective lattice size" L_{eff} at finite values of N. We have shown that the spectrum favours the $L_{\text{eff}} \propto N^{1/2}$ although we cannot exclude the $L_{\text{eff}} \propto N^{1/4}$ hypothesis. We have also argued how the would-be zero modes, which are a $\mathcal{O}(1/N)$ effect typically excluded in the perturbative analyses, can have a significant impact on the dynamics of the theory for finite N – especially when discussing the properties of the theory described by the low eigenvalues of the Dirac operator. In fact, they could be one possible explanation of the discrepancy with $N = 2$ simulations in the conformal/confining scenario that we observe at $N_f = 2$. We have also analyzed the square of the hermitian Wilson Dirac operator Q^2, argued how one can distinguish the would-be zero modes from the bulk part of the spectrum and given an estimate of the physical quark mass using the bulk part of the Q^2 spectrum.

* * *

There are several ways in which one can extend the results presented in this work. A first and foremost is the need to go to larger systems – that can be realized by using larger values of N and/or using lattices with more than one site. The latter possibility has the advantage of being easier to parallelize – there is a lot of room for improvement in this respect as almost all simulations performed in this work were executed on a single CPU core.

We also find finite-N corrections that are of order $\mathcal{O}(1/N)$ and that are rather large (see e.g. Fig. 6.1). $\mathcal{O}(1/N)$ correction are to be expected from the perturbation theory in the volume-reduced case (as opposed to $\mathcal{O}(1/N^2)$ that are expected in the large-volume models). They can also arise from the would-be zero modes that we observe in the spectrum of the Dirac operator.

All these problems can be healed by using twisted boundary conditions – there the system has $\mathcal{O}(1/N^2)$ corrections. Also as shown in Refs. [61, 74] the finite-N corrections to the plaquette are very small compared to the untwisted case. Another great advantage of the twisted boundary conditions is the effective size $L_{\text{eff}}(N) \propto N^{1/2}$ [80, 81].

To see how crucial it is to obtain this scaling rather than the more pessimistic one let us compare the CPU-time scaling of the volume-reduced model with the large-volume large-N simulations. For the large-volume simulations we have

$$t_{\text{CPU}}(L^4) \propto L^5 N^3, \tag{7.1}$$

where L^5 is the standard volume scaling of the HMC algorithm [85, 86] and N^3 is the cost of the matrix multiplication. On the single site and for light quarks we have:

$$t_{\text{CPU}}(1^4) \propto N^{4.5} = \begin{cases} L_{\text{eff}}^5 N^2 & \text{if } L_{\text{eff}} \propto N^{1/2} \\ L_{\text{eff}}^5 N^{3.25} & \text{if } L_{\text{eff}} \propto N^{1/4} \end{cases} \tag{7.2}$$

Thus the volume reduction is computationally much more competitive in the case of the former scaling. Our calculations suggest that the optimistic scenario is also possible in the untwisted model, however the matter is far from being as well-established as it is in the twisted case[2].

[2]To even further confirm this we have made some preliminary calculations of the

It is also crucial to calculate more physical quantities, in particular the meson masses. This can be done on the single site using the Quenched Momentum Prescription as described in Ref. [87]. However, as this method is quite novel and it raises some controversies (see e.g. Ref. [88]), it would be very beneficial to compare its results to the standard calculations that can be done by introducing one extended lattice direction. Calculation of the pion mass would be an important crosscheck on our findings of the confining/conformal scenario at $N_f = 2$. A setup with one elongated direction also allows the calculation of glueball masses.

Wilson Dirac spectrum with twisted boundary conditions and we find that at large b the spectrum resembles very closely that of the free fermion on the corresponding $L_{\text{eff}}^4 = (\sqrt{N})^4$ lattice. We also see no sign of the would-be "zero modes", which are present in the untwisted case.

Bibliography

[1] T. Eguchi, H. Kawai, *Phys. Rev. Lett.* **48** (1982) 1063.

[2] B. Bringoltz, M. Koreń, S. R. Sharpe, *Phys. Rev.* **D85** (2012) 094504 [1106.5538 [hep-lat]].

[3] B. Bringoltz, M. Koreń, S. R. Sharpe, *PoS* **LAT2012** 045 [1212.0535 [hep-lat]].

[4] K. G. Wilson, *Phys. Rev.* **D10** (1974) 2445.

[5] R. P. Feynman, A. Hibbs, *"Quantum Mechanics and Path Integrals"*, McGraw Hill, New York 1965.

[6] M. E. Peskin, D. V. Schroeder, *"An Introduction to Quantum Field Theory"*, Westview Press 1995.

[7] M. Creutz, *"Quarks, gluons and lattices"*, Cambridge UP, 1983.

[8] K. G. Wilson, in *"New phenomena in subnuclear physics"*, ed. A. Zichichi, Plenum Press, New York 1977 (Erice lectures 1975).

[9] G. 't Hooft, *Nucl. Phys.* **B72** (1974) 461.

[10] G. Veneziano, *Nucl. Phys.* **B117** (1976) 519.

[11] E. Corrigan, P. Ramond, *Phys. Lett.* **B87** (1979) 73.

[12] Y. M. Makeenko, A. A. Migdal, *Phys. Lett.* **B88** (1979) 135.

[13] L. G. Yaffe, *Rev. Mod. Phys.* **54** (1982) 407.

[14] B. Lucini, M. Panero, *Phys. Rep.* **526** (2013) 93 [1210.4997 [hep-th]].

[15] D. Foerster, *Phys. Lett.* **B87** (1979) 87.

[16] S. R. Wadia, *Phys. Rev.* **D24** (1981) 970.

[17] P. Kovtun, M. Ünsal, L. G. Yaffe, *JHEP* **0312** (2003) 034 [hep-th/0311098].

[18] G. Bhanot, U. M. Heller, H. Neuberger, *Phys. Lett.* **B113** (1982) 47.

[19] M. Okawa, *Phys. Rev. Lett.* **49** (1982) 353.

[20] J. Kiskis, R. Narayanan, H. Neuberger, *Phys. Lett.* **B574** (2003) 65 [hep-lat/0308033].

[21] V. A. Kazakov, A. A. Migdal, *Phys. Lett.* **B116** (1982) 423.

[22] D. J. Gross, Y. Kitazawa, *Nucl. Phys.* **B206** (1982) 440.

[23] B. Bringoltz, S. R. Sharpe, *Phys. Rev.* **D78** (2008) 034507 [0805.2146 [hep-lat]].

[24] A. González-Arroyo, M. Okawa, *Phys. Lett.* **B120** (1983) 174.

[25] A. González-Arroyo, M. Okawa, *Phys. Rev.* **D27** (1983) 2397.

[26] W. Bietenholz, J. Nishimura, Y. Susaki, J. Volkholz, *JHEP* **0610** (2006) 042 [hep-th/0608072].

[27] M. Teper, H. Vairinhos, *Phys. Lett.* **B652** (2007) 359 [hep-th/0612097].

[28] T. Azeyanagi, M. Hanada, T. Hirata, T. Ishikawa, *JHEP* **0801** (2008) 025 [0711.1925 [hep-lat]].

[29] A. González-Arroyo, M. Okawa, *JHEP* **1007** (2010) 043 [1005.1981 [hep-lat]].

[30] A. González-Arroyo, M. Okawa, *Phys. Lett.* **B718** (2013) 1524 [1206.0049 [hep-lat]].

[31] R. Narayanan, H. Neuberger, *Phys. Rev. Lett.* **91** (2003) 081601 [hep-lat/0303023].

[32] M. Koreń, *Acta Phys. Pol.* **B Proc. Suppl. 2** (2009) 489.

[33] P. Kovtun, M. Ünsal, L. G. Yaffe, *JHEP* **0706** (2007) 019 [hep-th/0702021].

[34] M. Ünsal, L. G. Yaffe, *Phys. Rev.* **D78** (2008) 065035 [0803.0344 [hep-th]].

[35] H. Vairinhos, *PoS* **LAT2011** 252 [1111.0303 [hep-lat]].

[36] P. Kovtun, M. Ünsal, L. G. Yaffe, *JHEP* **0507** (2005) 008 [hep-th/0411177].

[37] M. J. Strassler, hep-th/0104032.

[38] M. Schmaltz, *Phys. Rev.* **D59** (1999) 105018 [hep-th/9805218].

[39] A. Armoni, M. Shifman, G. Veneziano, *Nucl. Phys.* **B667** (2003) 170 [hep-th/0302163].

[40] A. Armoni, M. Shifman, G. Veneziano, *Phys. Rev.* **D71** (2005) 045015 [hep-th/0412203].

[41] A. Armoni, M. Shifman, G. Veneziano, *Phys. Rev. Lett.* **91** (2003) 191601 [hep-th/0307097].

[42] M. Ünsal, L. G. Yaffe, *Phys. Rev.* **D74** (2006) 105019 [hep-th/0608180].

[43] A. Armoni, M. Shifman, G. Veneziano, *Phys. Lett.* **B647** (2007) 515 [hep-th/0701229].

[44] H. Neuberger, *Annales Henri Poincare* **4** (2003) S147 [hep-th/0212097].

[45] B. Bringoltz, S. R. Sharpe, *Phys. Rev.* **D80** (2009) 065031 [0906.3538 [hep-lat]].

[46] S. Catterall, R. Galvez, M. Ünsal, *JHEP* **1008** (2010) 010 [1006.2469 [hep-lat]].

[47] A. J. Hietanen, R. Narayanan, *JHEP* **1001** (2010) 079 [0911.2449 [hep-lat]].

[48] A. J. Hietanen, R. Narayanan, *Phys. Lett.* **B698** (2011) 171 [1011.2150 [hep-lat]].

[49] D. D. Dietrich, F. Sannino, *Phys. Rev.* **D75** (2007) 085018 [hep-ph/0611341].

[50] F. Sannino, *Acta. Phys. Polon.* **B40** (2009) 3533 [0911.0931 [hep-ph]].

[51] J. Giedt, R. Brower, S. Catterall et al., *Phys. Rev.* **D79** (2009) 025015 [0810.5746 [hep-lat]].

[52] M. G. Endres, *Phys. Rev.* **D79** (2009) 094503 [0902.4267 [hep-lat]].

[53] K. Demmouche, F. Farchioni, A. Ferling et al., *Eur. Phys. J.* **C69** (2010) 147 [1003.2073 [hep-lat]].

[54] S. Catterall, J. Giedt, F. Sannino, J. Schneible, *JHEP* **0811** (2008) 009 [0807.0792 [hep-lat]].

[55] A. J. Hietanen, K. Rummukainen, K. Tuominen, *Phys. Rev.* **D80** (2009) 094504 [0904.0864 [hep-lat]].

[56] F. Bursa, L. Del Debbio, D. Henty et al., *Phys. Rev.* **D84** (2011) 034506 [1104.4301 [hep-lat]].

[57] M. Czakon, *Nucl. Phys.* **B710** (2005) 485 [hep-ph/0411261].

[58] M. Ünsal, L. G. Yaffe, *JHEP* **1008** (2010) 030 [1006.2101 [hep-th]].

[59] D. Gross, E. Witten, *Phys. Rev.* **D21** (1980) 446.

[60] B. Bringoltz, *JHEP* **0906** (2009) 091 [0905.2406 [hep-lat]].

[61] T. Azeyanagi, M. Hanada, M. Ünsal, R. Yacoby, *Phys. Rev.* **D82** (2010) 125013 [1006.0717 [hep-th]].

[62] J. C. Myers, M. C. Ogilvie, *JHEP* **0907** (2009) 095 [0903.4638 [hep-th]].

[63] T. J. Hollowood, J. C. Myers, *JHEP* **0911** (2009) 008 [0907.3665 [hep-th]].

[64] B. Bringoltz, *JHEP* **1001** (2010) 069 [0911.0352 [hep-lat]].

[65] S. Duane, A. D. Kennedy, B. J. Pendleton, D. Roweth, *Phys. Lett.* **B195** (1987) 216.

[66] I. Horvath, A. D. Kennedy, S. Sint, *Nucl. Phys. (Proc.Suppl.)* **73** (1999) 834.

[67] M. A. Clark, A. D. Kennedy, *Phys. Rev. Lett.* **98** (2007) 051601 [hep-lat/0610047].

[68] M. Lüscher, Les Houches lectures 2009, 1002.4232 [hep-lat].

[69] C. Gattringer, C. B. Lang, *"Quantum Chromodynamics on the Lattice. An Introductory Presentation"*, Springer Berlin/Heidelberg 2009.

[70] I. P. Omelyan, I. M. Mryglod, R. Folk, *Comput. Phys. Commun.* **151** (2003) 272.

[71] T. Takaishi, P. de Forcrand, *Phys. Rev.* **E73** (2006) 036706 [hep-lat/0505020].

[72] N. I. Achiezer, *"Theory of Approximation"*, Dover Publications, New York 1992.

[73] B. Jegerlehner, hep-lat/9612014.

[74] A. Gonzalez-Arroyo, M. Okawa, *PoS* **LAT2012** 046 [1210.7881 [hep-lat]].

[75] S. R. Sharpe, R. L. Singleton, Jr., *Phys. Rev.* **D58** (1998) 074501 [hep-lat/9804028].

[76] L. Del Debbio, M. T. Frandsen, H. Panagopoulos, F. Sannino, *JHEP* **0806** (2008) 007 [0802.0891 [hep-lat]].

[77] C. Allton, M. Teper, A. Trivini, *JHEP* **0807** (2008) 021 [0803.1092 [hep-lat]].

[78] P. Diaconis, S. E. Evans, *Trans. Amer. Math. Soc.* **353** (2001) 2615.

[79] B. Bringoltz, *Phys. Rev.* **D79** (2009) 105021 [0811.4141 [hep-lat]].

[80] J. Ambjorn, Y. M. Makeenko, J. Nishimura, R. J. Szabo, *JHEP* **9911** (1999) 029 [hep-th/9911041].

[81] M. Ünsal, *JHEP* **0512** (2005) 033 [hep-th/0409106].

[82] M. Creutz, *Annals Phys.* **322** (2007) 1518 [hep-th/0609187].

[83] C. Gattringer, I. Hip, *Nucl. Phys.* **B536** (1998) 363 [hep-lat/9712015].

[84] L. Giusti, M. Lüscher, *JHEP* **0903** (2009) 013 [0812.3638 [hep-lat]].

[85] M. Creutz, *Phys. Rev.* **D38** (1988) 1228.

[86] R. Gupta, G. W. Kilcup, S. R. Sharpe, *Phys. Rev.* **D38** (1988) 1278.

[87] R. Narayanan, H. Neuberger, *Phys. Lett.* **B616** (2005) 76 [hep-lat/0503033].

[88] M. Teper, *Acta Phys. Polon.* **B40** (2009) 3249 [0912.3339 [hep-lat]].